Observatório Nacional

MINISTÉRIO DA CIÊNCIA, TECNOLOGIA, INOVAÇÕES E COMUNICAÇÕES

COSMOLOGICAL APPLICATIONS OF FAST RADIO BURSTS

Thaís Lemos Porciúncula Alves

Tese de Doutorado apresentada ao Programa de Pós-graduação em Astronomia do Observatório Nacional/MCTIC, como parte dos requisitos necessários à obtenção do Título de Doutor em Astronomia.

Orientador: Jailson Souza de Alcaniz

Rio de Janeiro
Outubro de 2024

COSMOLOGICAL APPLICATIONS OF FAST RADIO BURSTS

Thaís Lemos Porciúncula Alves

TESE SUBMETIDA AO PROGRAMA DE PÓS-GRADUAÇÃO EM ASTRONOMIA DO OBSERVATÓRIO NACIONAL/MCTIC COMO PARTE DOS REQUISITOS NECESSÁRIOS PARA A OBTENÇÃO DO TÍTULO DE DOUTOR EM ASTRONOMIA.

Examinada por:

Prof. Nome do Primeiro Examinador Sobrenome, D.Sc.

Prof. Nome da Segunda Examinadora Sobrenome, Ph.D.

Dr. Nome da Terceira Examinadora Sobrenome, D.Sc.

Prof. Nome do Quarto Examinador Sobrenome, Ph.D.

Prof. Nome do Quinto Examinador Sobrenome, Ph.D.

RIO DE JANEIRO, RJ – BRASIL
OUTUBRO DE 2024

Lemos Porciúncula Alves, Thaís

Cosmological applications of fast radio bursts/Thaís Lemos Porciúncula Alves. – Rio de Janeiro: ON/MCTIC, 2024.

XVIII, 124 p.: il.; 29, 7cm.

Orientador: Jailson Souza de Alcaniz

Tese (doutorado) – ON/MCTIC/Programa de Pós-graduação em Astronomia, 2024.

Bibliography: p. 95 – 116.

1. keyword 1. 2. keyword 2. 3. keyword 3. 4. keyword 4. I. , . II. Observatório Nacional/MCTIC, Programa de Pós-graduação em Astronomia. III. Título.

The nitrogen in our DNA, the calcium in our teeth, the iron in our blood, the carbon in our apple pies were made in the interiors of collapsing stars. We are made of starstuff.

Carl Sagan

Spacetime tells matter how to move; matter tells spacetime how to curve.
(John Wheeler)

Agradecimentos

Ao longo desses quatro anos de doutorado, várias pessoas estiveram presentes na minha formação e contribuiram para a consolidação desse trabalho, seja de forma direta, trabalhando comigo, como também de forma indireta, me dando apoio. Assim, gostaria de agradecer:

- Ao meu orientador, Jailson Alcaniz, pela dedicação e orientação. Muito obrigada pela atenção e ensinamentos ao longo de todos esses anos. Sei o quanto se importa com a formação dos seus alunos e o quanto tenta nos fazer melhorar a cada dia. Foi um enorme prazer ser orientada ao longo do mestrado e doutorado por você.

- Ao Rodrigo Gonçalves, que me acompanha desde o início do meu doutorado. Sou muito grata por todos os ensinamentos, conselhos e atenção. Muito obrigada pela sua dedicação.

- Ao Joel Carvalho, por sua dedicação desde meu mestrado. Sua colaboração foi fundamental na minha formação.

- À minha mãe, Anna, por ser essa constância na minha vida em todos os momentos. Seu amor e dedicação foram fundamentais para eu chegar até aqui.

- Ao meu irmão, Bruno, por dividir essa existência comigo. Sua presença torna minha vida mais alegre e feliz.

- A Dinorah e ao Pedro, que dividem comigo todas as alegrias e ansiedades de ser um pós-graduando. O apoio e amizade de vocês são muito importantes para mim. Ver vocês conquistarem o que desejam, é um dos meus grandes desejos. Obrigada por estarem presente esses anos todos.

- Ao Carlos Bengaly, por sua amizade e aprendizado. Muito obrigada por todos os momentos em que você me ajudou com dicas e sugestões, mas também, por todo apoio e conselho.

- A todas as pessoas maravilhosas da Cosmologia (espero não esquecer ninguém): Agripino Sousa, Rayff Souza, Gabriel Rodriguez, Jamerson Rodrigues, Javier Gonzalez, Simony Costa, Rodrigo von Marttens, Felipe Ávila, Marcela Campista, Gustavo Borges e Thais Guerini. Todos me proporcionaram momentos de discussões científicas extremamente enriquecedoras para meu crescimento. Muito obrigada.

- A todos os meus colegas da casa branca. Especialmente: Jonatã, Fernanda, Jaiane, Shao, Thiago, Ester e Bruno. Vocês tornaram os meus dias mais alegres.

- Às minhas amigas, Luana e Joyce, por todos esses 14 anos ao meu lado. Seguimos rumos diferentes na vida, mas sempre que precisei, eu pude contar com vocês e isso não tem preço.

- Às pessoas maravilhosas que tenho prazer de chamar de amigos, Ellen, Mariana e Rodolpho. A amizade de vocês foi muito importante. Agradeço por todo o carinho e atos de perturbação que compartilhamos.

- Ao meu amigo Anselmo, que chegou há pouco tempo na minha vida, mas já se mostrou tão importante para mim. Você me fez rir nos momentos em que mais precisei.

- Aos amores da minha vida, Fred e Paco, que não me deixaram desanimar quase me enloquecendo ao longos desses anos. Voltar para vocês é sempre a melhor parte. Amo vocês!

- A Tangerina, por dividir todo seu amor (se é que é possível) comigo. Por ser nosso apoio emocional em troca de comida.

- A Christiane Garnnier, por ser essa pessoa maravilhosa nos tratando com tanto carinho e dedicação.

- A todos os funcionários do Observatório Nacional, que de forma direta ou indireta são responsáveis pelo funcionamento da Pós-Graduação.

- À CAPES pelo apoio financeiro fundamental para que tudo isso fosse possível.

Resumo da Tese apresentada ao Programa de Pós-graduação em Astronomia do Observatório Nacional/MCTIC como parte dos requisitos necessários para a obtenção do título de Doutor em Astronomia (D.Sc.)

COSMOLOGICAL APPLICATIONS OF FAST RADIO BURSTS

Thaís Lemos Porciúncula Alves

Outubro/2024

Orientador: Jailson Souza de Alcaniz

Programa: Astronomia

As *fast radio bursts* (FRBs) são uma nova classe de eventos transitórios de alta energia com curta duração na faixa da frequência do rádio de algumas centenas a alguns milhares de MHz. Embora o mecanismo físico responsável por estes eventos ainda esteja em debate, o grande valor da medida de dispersão observada (DM) acima da contribuição da Via Láctea sugere uma origem extragaláctica ou cosmológica para as FRBs. Ao identificar a origem da explosão, é possível medir diretamente o *redshift* e combiná-lo com DM e, assim, estudar cosmologia. Por exemplo, a partir da relação DM $- z$ pode-se testar o princípio da equivalência fraca ou restringir os parâmetros cosmológicos, como a fração da massa de bárions no meio intergaláctico ($f_{\rm IGM}$, onde IGM denota o meio intergaláctico, vindo do inglês *intergalactic medium*) e a constante de Hubble. Desde a primeira FRB descoberta em 2007 pelo telescópio Parkes, quase mil eventos foram detectados por novos telescópios. No entanto, apenas alguns FRBs na literatura estão bem localizados (com *redshift* da galáxia hospedeira), e este número não é ainda grande o suficiente para realizar análises estatísticas robustas num cenário cosmológico. As outras questões nas análises das FRB são: (i) o $f_{\rm IGM}$ é fortemente degenerado com os parâmetros cosmológicos e não está bem restrito; (ii) a grande variância no DM devido às heterogeneidades na densidade de elétrons cósmicos não é bem modelada; (iii) e por último, o conhecimento limitado da contribuição da galáxia hospedeira. Neste contexto, na primeira parte desta Tese, discutimos em detalhes as principais características astrofísicas dos FRBs. Na segunda parte, que discute algumas aplicações de FRBs em cosmologia, apresentamos um método independente

do modelo cosmológico para estimar o $f_{\rm IGM}$ e a contribuição da galáxia hospedeira, combinando FRBs com galáxias hospedeiras localizadas e de dados de supernovas tipo Ia. Usamos os dados mais atuais das FRBs observadas e, em seguida, exploramos como pesquisas futuras irão melhorar a estimativa desses parâmetros, simulando os dados de FRBs a partir do método de simulação de Monte Carlo. Além disso, testamos nossas teorias físicas buscando uma variação espaço-temporal das constantes fundamentais. Em particular, utilizamos a medida de dispersão de FRBs para investigar uma possível evolução do *redshift* da constante de estrutura fina (α), considerando o cenário do *runaway dilaton*. Usando um método independente do modelo cosmológico, derivamos novas expressões para a dependência de DM em relação à constante de estrutura fina.

Palavras-Chave: Cosmologia; *Fast Radio Bursts*; Simulação de Monte Carlo; Meio Intergaláctico; Fração de Bárions

Abstract of Thesis presented to Observatório Nacional/MCTIC as a partial fulfillment of the requirements for the degree of Doctor of Astronomy (D.Sc.)

TITLE

Thaís Lemos Porciúncula Alves

October/2024

Advisor: Jailson Souza de Alcaniz

Department: Astronomy

Fast radio bursts (FRBs) are a new class of high-energy transient events with short duration within the radio frequency range from a few hundred to a few thousand MHz. Although the physical mechanism responsible for these events is still in debate, the larger value of the observed dispersion measure (DM) above that of the Milk Way contribution suggests an extragalactic or cosmological origin for the FRBs. By identifying the origin of the burst, it is possible to measure the redshift directly and can be combined with DM to study cosmology. For instance, from the DM $- z$ relation one can test the weak equivalence principle and constrain the cosmological parameters, such as the fraction of baryon mass in the intergalactic medium ($f_{\rm IGM}$) and the Hubble constant. Since the first discovered FRB in 2007 by the Parkes telescope, almost one thousand events have been detected by new survey telescopes. However, only a few FRBs in the literature are well localized (with redshift of the host galaxy), and this number is not large enough to perform robust statistical analysis in a cosmological scenario. The other issues in FRB analyses are: (i) the $f_{\rm IGM}$ is strongly degenerated with the cosmological parameters and is not well constrained; (ii) the poor modeling of the large variance in the DM due to inhomogeneities in the cosmic electrons density; (iii) and lastly, the limited knowledge of the host galaxy contribution. In this context, in the first part of this Thesis, we discuss in detail the main astrophysical features of FRB. In the second part, dedicated to the cosmological application of FRBs, we present a cosmological model-independent method to estimate the $f_{\rm IGM}$ and host galaxy contribution by combining FRBs with localized host galaxy and supernovae type Ia dataset. We use the current FRBs observational data and then we explore how future surveys will improve these parameters

estimation by simulating the FRBs data from Monte Carlo simulation method. In the second part, we test our physical theories by searching for a space-time variation of the fundamental constants. In particular, we use the dispersion measure of FRBs to investigate a possible redshift evolution of the fine-structure constant (α), considering the runaway dilaton scenario. Using a cosmological model-independent method, we derive new expressions for DM dependence concerning the fine-structure constant.

Keywords: Cosmology; Fast Radio Bursts; Monte Carlo Simulation; Intergalactic Medium; Baryon fraction

Contents

List of Figures

List of Tables

Chapter 1

Introduction

The standard cosmological model describes our current understanding of the Universe, including its evolution and composition, and is based on two fundamental hypotheses: The cosmological Principle (CP) [13] and the General Theory of Relativity (GTR) [14]. The CP establishes the Universe as being homogeneous and isotropic statistically at large scales for any observer while GTR provides a description of the gravitational interaction on cosmological scales.

The current standard cosmological model, the ΛCDM, is capable of describing the observed Universe by fixing only six free parameters: dark matter density ($\Omega_c h^2$), the baryon density ($\Omega_b h^2$), the observed angular size of the sound horizon at recombination ($100\theta_{MC}$), the scalar spectral index (n_s), the curvature fluctuation amplitude ($\ln(10^{10} A_s)$), and the reionization optical depth (τ) [15]. According to the ΛCDM model, our Universe is composed of: the cosmological constant (Λ) that plays the role of the dark energy, which is the component responsible for the late-time acceleration of the expansion of the Universe with negative pressure in the cosmological equations, and represents $\sim 70\%$ the bulk of the Universe's energy density; the cold dark matter (CDM term), which is the non-relativistic component that interacts only gravitational and account for $\sim 25\%$; lastly, the remaining content is composed of baryonic matter, stars, galaxies, and all the luminous structures.

The observations of some objects in the Universe provide strong evidence for the ΛCDM as the standard cosmological model, such as the accelerated expansion of the Universe deduced from the observed light curves of supernovae type Ia (SNe) [16, 17] and the power spectrum and statistical properties of the cosmic radiation background (CMB) anisotropies [15, 18]. Despite of its remarkable successes and simplicity, the ΛCDM model presents some critical issues (see Ref. [19] for a review). For instance, the so-called cosmological constant problem, that is the large discrepancy between cosmological observations and quantum field theory's predictions - around 120 orders of magnitude - when we associate the Λ with the energy density of the vacuum [20]. Another question is related to the actual nature of the

dark energy and the dark matter. Finally, a relevant challenge is the discrepancy between some parameters, for example, the 5σ-tension between the value of Hubble constant (H_0) using observations at early and late cosmological time [21, 22]. In this concern, more observational data involving cosmological model-independent approaches to cosmological quantities is required for a proper evaluation of the cosmological parameters and to avoid previous assumptions on the large-scale evolution of the Universe.

In this context, the Fast Radio Bursts (FRBs) emerge as a recent astrophysical/cosmological phenomenon [3, 11]. FRBs are a class of transient radio events (their brightness varies drastically over timescale from seconds to years), with high brightness temperature ($\sim 10^{25}$ - 10^{30} K) and duration of order milliseconds or less. So far, FRBs have been detected in range frequency from ~ 100 MHz [23] to 8 GHz [24]. Before the discovery of FRBs, radio pulsars were the only known sources of producing extremely high brightness temperatures [11].

The first burst was discovered in 2007 by Parkes telescope and this FRB was named as FRB 010724 or Lorimer burst [1]. Since then almost one thousand FRBs sources have been discovered by new surveys, such as e.g. the Canadian Hydrogen Intensity Mapping Experiment (CHIME) [25]. One can classify these events as repeating or non-repeating (or one-off) if a second burst or more is detected from the same source, with a fixed period or cyclical phases of irregular activity. Most FRBs are reported to be non-repeating, but it is impossible to claim that an FRB source is not a repeater. This happens because all FRBs may repeat but with a wide range of repetition rates.

The radiation mechanism of FRBs is a mystery until today, but the high brightness temperature and short duration of these events give us clues about their radiation emission. Such features demand that the radiation mechanism for FRB emission must be "coherent", which means that the particles emit the radiation in the same phase. Several models have been proposed in the last years to explain the radiation mechanism [11] and the progenitor source [26] of these events, but all of them are based on limited observational data and most of these ideas are disfavored or completely rejected with new data. Since the discovery of FRB 200428 [27], associated with active magnetars, many models suggest this class of neutron stars as a progenitor source of FRBs. Indeed the FRB events may be a mix of different populations or progenitor mechanisms.

Although the nature of FRBs progenitors remains inconclusive, the dispersion measure (DM) makes it possible to use extragalactic FRBs for cosmological research. The radio waves from the FRBs bursts undergo dispersion traveling through the plasma along the path from the source to the Earth. The total DM is the integral of the column density of free electrons along the line of sight. It contains important

information on cosmological distances and the ionization state of the Universe from the redshift of emission until today. The large value of observed DM compared to the Milky Way contribution of these events [28] suggests their extragalactic or even cosmological origin.

To determine the redshift of these bursts, first, it is necessary to identify their host galaxy, which has been challenging so far. However, when the origin of the burst is confirmed and, consequently, the host galaxy is identified, the redshift can be measured directly. In this situation, one can combine the dispersion measure with the redshift to obtain the DM $-$ z relation [29]. The FRBs can be used as an astrophysical and cosmological probe from these relations. For instance, to test the weak equivalence principle [30], to probe the anisotropic distribution of baryon matter in Universe [31] or to constrain cosmological parameters [32, 33], such as Hubble constant [34–36] and the baryon mass fraction in the intergalactic medium ($f_{\rm IGM}$) [37–39].

In practice, some issues hinder the application of FRBs for cosmological purposes and must be better understood to explore the full potential of these objects. For instance, the variance in the dispersion measure [40–43], which is due to the inhomogeneous cosmic distribution of the electrons. These density fluctuations can be treated as a probability distribution [41] or as a fixed value in the statistical analyses [42]. Another limitation is the contribution of the host galaxy ($\rm DM_{host}$), which is difficult to estimate from observations and to model because it depends on many factors, such as the galaxy type, the relative orientation between the FRB source related to the host as well as the mass of the host galaxy [44]. To circumvent this problem, $\rm DM_{host}$ can be assumed to be a free parameter or a log-normal distribution [41]. Finally, the last restriction is the poor knowledge about the variation with respect to the redshift of the fraction of baryon mass in the intergalactic medium (IGM), called as $f_{\rm IGM}$, which is degenerated with the cosmological parameters. In this context, many works have been performed to discuss the baryon distribution in the IGM using both numerical simulations [45–47] and observations [48–50]. In Reference [47], the authors obtained that $f_{\rm IGM} \approx 0.9$ at $z \geq 1.5$, while the authors in Reference [49], the authors found that $f_{\rm IGM} \approx 0.82$ at $z \geq 0.4$. From these results one may infer that the $f_{\rm IGM}$ grows with redshift.

As commented before, an important aspect related to studying FRBs in cosmology is the identification of the host galaxy. Although several bursts have been observed in the last years, only a few had the host galaxy identified, which restricts their applications in cosmology. Currently, only 39 FRB events in the literature are well localized, with the correspondent redshift, and this sample is not large enough to perform robust statistical analysis. However, several dedicated search programs are now ongoing or about to start, increasing the number of detected events by

many orders of magnitude. Eventually, large-scale experiments such as the CRACO system of Australian Square Kilometre Array Pathfinder (ASKAP) [51], the CHIME outriggers [52], the Square Kilometre Array (SKA) [53], Deep Synoptic Array (DSA-110) [54] and BINGO Interferometry System [55] will discover up to thousands of FRBs per year.

This thesis proposes to use FRBs as a tool to study the underlying cosmology, constraining cosmological parameters from model-independent methods to avoid previous assumptions that could bias these analyses. This thesis is organized as follows. In Chapter 2, we introduce the fundamental properties of FRBs and discuss about the radiation emission and progenitor models of these events. In Chapter 3, we present the observational features of FRBs, including population properties. The Chapters 4, 5 and 6 constitute the original results of this work, which involve the application of FRBs in cosmology scenarios. In Chapters 4 and 5 we constrain the mass of baryon fraction in IGM and host galaxy contribution. In Chapter 6 we search for a possible variation of the fine structure constant. Finally, we present the conclusion and future perspectives in Chapter 7.

PART I

Astrophysics of Fast Radio Bursts

Chapter 2

Theoretical aspects of FRBs

In the previous chapter, we discussed the motivations and goals of working with FRBs in the cosmology scenario. In this chapter, we present the fundamental concepts of FRBs (Sec. 2.1) and explain some of their main properties and the propagation effects (for recent reviews about FRBs, see [3, 5, 11, 26]). We also discuss possible radiation emission mechanisms (Sec. 2.2) and progenitor models of FRBs (Sec. 2.3).

2.1 Properties of FRBs

The radio waves from the FRB source will pass through: its host galaxy, the intergalactic medium (IGM), and our own galaxy, the Milky Way (MW), before reaching the observer in the Earth. Such signals can be affected by these intervening mediums, suffering the following propagation effects. i) First, the signal is dispersed in the plasma, causing the high-frequency photon to arrive earlier than the low-energy one. ii) the photons can scatter, broadening the signal. iii) scintillation can occur due to diffraction and refraction by turbulent gas. iv) the plasma medium could lead to a lensing effect. v) Another effect is polarization, which can change when radio waves propagate in magnetized plasma. vi) Finally, if the plasma is dense enough, the radio emission can be absorbed. Such effects lead to many important observed and derived properties of FRBs, which we will discuss below.

2.1.1 Dispersion

The radio waves are dispersed in the plasma between the source and the Earth observer because the photons from the FRB interact with the free electrons in the medium which the radio wave passes through. Since each small range of frequencies travels at a slightly different group velocity, those photons will reach Earth at a slightly different time [3]. For this reason, in this subsection, we will follow the

Reference [56] to introduce the concepts of the time delay and dispersion measure of the FRBs.

Time delay

The dispersion relation in a cold plasma is [56]

$$\omega^2 = \omega_p^2 + k^2 c^2, \tag{2.1}$$

where the plasma frequency is

$$\omega_p^2 = \frac{4\pi n e^2}{m}, \tag{2.2}$$

being n, e, m the density of free electrons, the electron charge, and the mass of the electron, respectively.

So the group velocity of the electromagnetic wave is [56]

$$v_g = \frac{d\omega}{dk} = c\sqrt{1 - \frac{\omega_p^2}{\omega^2}}. \tag{2.3}$$

Then, the time required for a wave of a source at a distance d with frequency ω and group velocity v_g to reach Earth can be written as

$$t_g = \int_0^d \frac{dS}{v_g} \approx \int_0^d \left(1 + \frac{\omega_p^2}{2\omega^2}\right) dS, \tag{2.4}$$

where S measures the line-of-sight distance from the source to the Earth.

Now, let us consider that the frequency does not change along with S

$$t_p \approx \frac{d}{c} + \left(2\omega^2 c\right)^{-1} \int_0^d \omega_p^2 dS. \tag{2.5}$$

Replacing the plasma frequency relation (Eq. 2.2) into the equation above, we can express the delayed arrival time of two photons with frequencies ν_1 and ν_2 ($\nu_1 < \nu_2$) as

$$\Delta t = \frac{e^2}{2\pi m_e c}\left(\frac{1}{\nu_1^2} - \frac{1}{\nu_1^2}\right) \int_0^d n \; dS. \tag{2.6}$$

Note that Eq. 2.6 indicates that high energy photons arrive earlier at the observer than low-energy ones, which is illustrated in Figure 2.1 where is presented the dynamic spectrum ("waterfall" plot) of the first-discovered event, FRB 010724 (also know as Lorimer burst) [1]. The dispersive "sweep" clearly indicates that high-energy photons arrive earlier than low-energy ones.

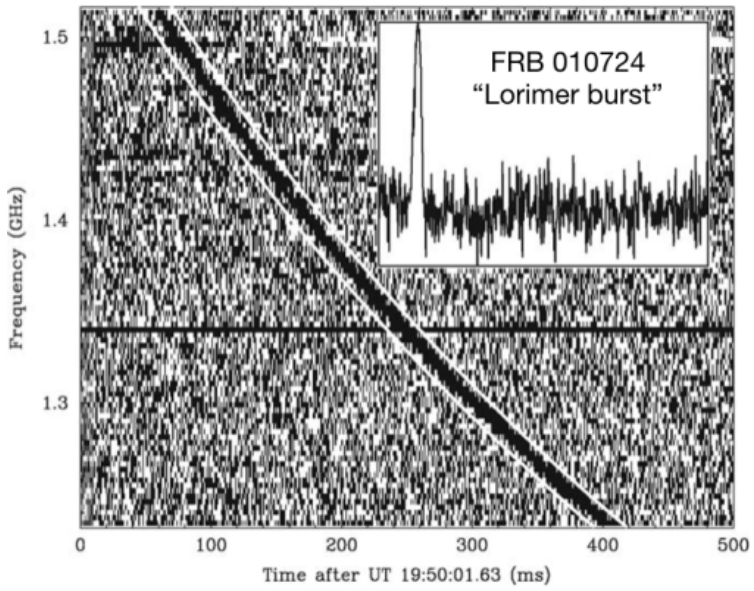

Figure 2.1: The first reported FRB: FRB 010724 or the "Lorimer burst" as a function of frequency and time (a 'dynamic spectrum'). The burst has a DM of 375 pc/cm^3. **Credit:**[1]

Definition of Dispersion Measure

The quantity that is usually measured is the rate change of the arrival time with respect to frequency. So, let us replace the plasma frequency relation (Eq. 2.2) into Equation 2.5 and assume that the number density is the only quantity that changes with S, we find

$$\frac{dt_p}{d\omega} = -\frac{4\pi e^2}{cm\omega^3}\int_0^d n\, dS. \tag{2.7}$$

We can introduce the dispersion measure (DM) quantity that is the column of free electrons along the line-of-sight from the source to the observer and is quoted in units of pc/cm^3. This parameter is obtained for each FRB when it is discovered and describes the degree of the delay in the arrival time. DM can be written as

$$\mathrm{DM} = \int_0^d n\, dS. \tag{2.8}$$

Cosmological Extension

In order to write Equation 2.8 considering a cosmological point of view, we will redo the previous analysis assuming the FRB as coming from an extragalactic source at redshift z. For that, it is necessary to consider three effects [57]: the change in the observed frequency from the redshift of light ($\omega \to \omega = (1+z)\omega_{\mathrm{obs}}$); a redshift dependence on the electronic density ($n_e = n_e(S) \to n_e = n_e(z)$); and the time

dilation effect (with the introduction of a $(1+z)$ term).

The distance of the propagated electromagnetic wave ($dS = cdt$) and finding the time variation from the definition of the Hubble parameter $\left(dt = -\frac{dz}{(1+z)H(z)}\right)$, the rate change of the arrival time becomes

$$t_p = \frac{d}{c} + \frac{1}{2\omega_{\rm obs}^2}\int_0^z \frac{\omega_p^2}{(1+z)^2 H(z')} dz'. \tag{2.9}$$

So the derivative of the previous equation in terms of the observed frequency gives us:

$$\frac{dt_p}{d\omega_{\rm obs}} = -\frac{1}{\omega_{\rm obs}^3}\int_0^z \frac{\omega_p^2}{(1+z)^2 H(z')} dz'. \tag{2.10}$$

Replacing the plasma frequency (Eq. 2.2), we obtain

$$\frac{dt_p}{d\omega_{\rm obs}} = -\frac{4\pi e^2}{c m_e \omega_{\rm obs}^3}\int_0^z \frac{n_e(z')c}{(1+z')^2 H(z')} dz', \tag{2.11}$$

where the speed of light in both the numerator and denominator are necessary to guarantee the correct units of the dispersion measure given by

$$\mathrm{DM} = \int_0^z \frac{n_e(z')c}{(1+z')^2 H(z')} dz'. \tag{2.12}$$

Dispersion Measure

Since the speed of the photons will change due to the interaction in the plasma, we will have a speed for each medium. Then we can write the observed dispersion measure as a contribution of several components[29, 58]:

$$\mathrm{DM_{obs}}(z) = \mathrm{DM_{MW}} + \mathrm{DM_{IGM}}(z) + \mathrm{DM_{host}}(z), \tag{2.13}$$

where the subscripts MW, IGM, and host denote contributions from the Milky Way, IGM, and the FRB host galaxy, respectively. The observed DM of a FRB is directly measured from the corresponding event.

The DM of the Milky Way has a contribution from the Milky Way interstellar medium (ISM) and from the Milky Way halo, estimated by the relation [41].

$$\mathrm{DM_{MW}} = \mathrm{DM_{MW,ISM}} + \mathrm{DM_{MW,halo}}. \tag{2.14}$$

$\mathrm{DM_{MW,ISM}}$ can be well constrained using models of the ISM galactic electron distribution in the Milky Way such as NE2001 [59] and YMW16 [60] from pulsar observations [61]. The Milky Way halo contribution is not well constrained yet and is limited at $\mathrm{DM_{MW,halo}} \sim 30-80$ [28, 62]. In our analysis, we follow [41] and assume

$\mathrm{DM_{MW,halo}} = 50$ pc/cm^3 .

Subtracting the Galaxy contribution from the observation of DM we define the observed extragalactic DM as

$$\mathrm{DM_{ext}}(z) \equiv \mathrm{DM_{obs}}(z) - \mathrm{DM_{MW}} \ , \tag{2.15}$$

so that, using Eq. 2.13, the theoretical extragalactic DM can be calculated as

$$\mathrm{DM^{th}_{ext}}(z) \equiv \mathrm{DM_{IGM}}(z) + \mathrm{DM_{host}}(z) \ , \tag{2.16}$$

where both terms on the right-hand side are described as follows.

The host galaxy contribution, $\mathrm{DM_{host}}$, is not well constraining because depends on many factors, such as the type of the galaxy, the relative orientations of the FRBs source with respect to the host and source, and the near-source plasma [44], being a difficult parameter to estimate from observations and to model. In this concern, previous works studied the redshift evolution of $\mathrm{DM_{host}}$ through different functions, but it remains unknown. For instance, the authors in Reference [63] studied simple log-normal form with a median value of 100 pc/cm^{-3}, while in Ref. [41] the authors used a log-normal distribution with a median value as a free parameter in the range $20 - 200$ pc/cm^{-3}. For this reason, we can write the redshift evolution of $\mathrm{DM_{host}}(z)$ using the relation [29, 64]:

$$\mathrm{DM_{host}}(z) = \frac{\mathrm{DM_{host,0}}}{(1+z)} \ , \tag{2.17}$$

where the $(1+z)$ factor accounts for the cosmological time dilation for a source at redshift z.

The largest contribution to $\mathrm{DM_{obs}}$ (Eq. 2.13) is from the ionized IGM and their contribution can be obtained when the expression for DM (Eq. 2.8) is extended, accounting for the effects of the cosmological redshift, which is given by Equation 2.12. Following Reference [29], where the authors derived a more general expression for $\mathrm{DM_{IGM}}$, let us consider the number density of free electrons at redshift z as

$$n_e(z) = \frac{3H_0^2\Omega_b}{8\pi G m_p} f_{\mathrm{IGM}} \chi_e(z)(1+z)^3. \tag{2.18}$$

Finally, replacing the above equation into Eq. 2.12, we obtain the average dispersion measure from IGM as a function of the redshift [29]

$$\mathrm{DM_{IGM}}(z) = \frac{3c\Omega_b H_0^2}{8\pi G m_p} \int_0^z \frac{(1+z') f_{\mathrm{IGM}}(z') \chi_e(z')}{H(z')} dz' \ , \tag{2.19}$$

where c is the speed of light, Ω_b is the present-day baryon density parameter, H_0 is the Hubble constant, G is the gravitational constant, m_p is the proton mass, $f_{\mathrm{IGM}}(z)$

is the baryon fraction in the IGM, $H(z)$ is the Hubble parameter at redshift z and the free electron number fraction per baryon is given by

$$\chi_e(z) = Y_H \chi_{e,H}(z) + Y_{He} \chi_{e,He}(z) \ . \tag{2.20}$$

The terms $Y_H = 3/4$ and $Y_{He} = 1/4$ are the mass fractions of hydrogen and helium, respectively, while $\chi_{e,H}(z)$ and $\chi_{e,He}(z)$ are the ionization fractions of hydrogen and helium, respectively. At $z < 3$ hydrogen and helium are fully ionized ($\chi_{e,H}(z) = \chi_{e,He}(z) = 1$) [47, 65], so that we have $\chi_e(z) = 7/8$. From the above equations, one can constrain a possible evolution of the baryon fraction by modeling both $\mathrm{DM_{host,0}}$ and $\mathrm{DM_{IGM}}$ and comparing the theoretical predictions with the observed values of $\mathrm{DM_{ext}}$.

2.1.2 Scattering

The pulse width (W) is defined as the duration of FRB and is in the order of milliseconds. The observed pulse width is a combination of an intrinsic pulse of width (W_{int}), instrumental broadening, and propagation effect [3]

$$W = \sqrt{W_{\mathrm{int}}^2 + t_{\mathrm{samp}}^2 + \Delta t_{\mathrm{DM}}^2 + \Delta t_{\mathrm{DM_{err}}}^2 + \tau_s^2}, \tag{2.21}$$

where t_{samp} is the data sampling interval, the frequency-dependent smearing due to dispersion measure DM is $\Delta t_{\mathrm{DM}} = (8.3\mu s)\mathrm{DM}\Delta\nu_{\mathrm{MHz}}\nu_{\mathrm{GHz}}^{-3}$ [66]. The dispersive delay due to dedispersion at a slightly incorrect DM is $\Delta t_{\mathrm{DM_{err}}} = \Delta t_{\mathrm{DM}}(\mathrm{DM_{err}}/\mathrm{DM})$ [66]. The pulses can also be temporally broadened and such effect is called as scattering (τ_s).

The photons from the FRB signal can be scattered by particles on its path. The scattering effect induces a change in the moving direction of photons. A portion of these scattered photons could travel along a longer path and then arrive later than the unscattered ones, giving the FRB signal a tail feature. Such tail usually appears as an exponential decay which scales strongly with frequency as [67, 68]

$$\tau_s \propto \nu^{-4}, \tag{2.22}$$

where ν is the frequency of the source.

Figure 2.2 shows the frequency-dependent widths of FRB 110220, where at lower frequencies the decaying wing presents a tail.

2.1.3 Scintillation

Like the twinkling of stars that is caused by light passing through the turbulent

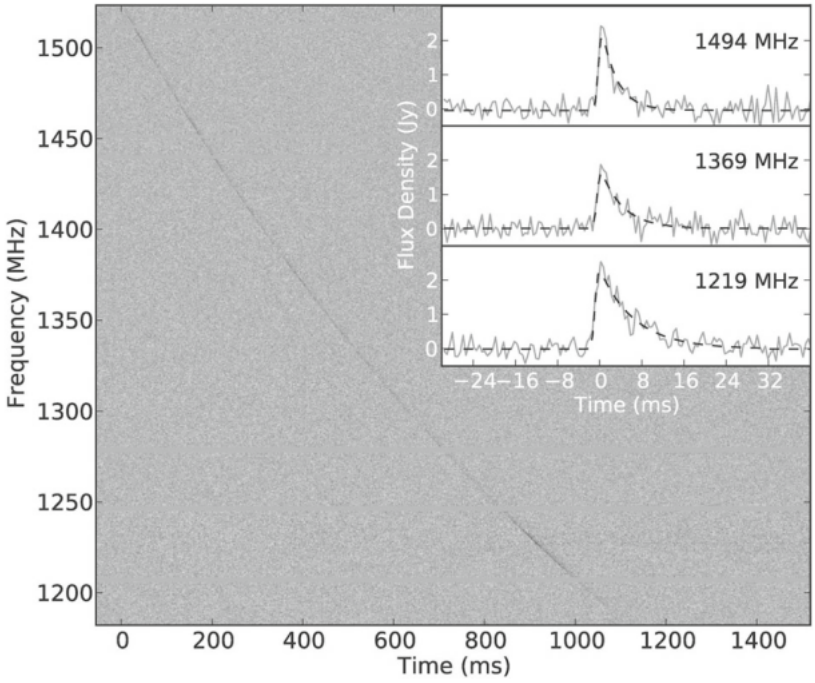

Figure 2.2: Scattering seen in FRB 110220. The main panel shows the dynamic spectrum of the burst and its dispersive sweep. The inset shows how the burst becomes asymmetrically broadened towards lower radio frequencies. **Credit:**[2]

atmosphere of the Earth, there is the scintillation of FRBs. This effect is caused by the diffraction and refraction when the radio signal passes through the clumpy and turbulent plasma medium. When the waves pass through the medium together, delays in the signal cause destructive or constructive interference, creating a complex frequency structure that varies with time. The relative motion between the observer, source, and scattering medium leads to a variation of the observed flux density that depends strongly on the frequency. The scintillation bandwidth can be written as

$$\Delta\nu_{\text{scint}} \propto \nu^4. \tag{2.23}$$

Such phenomena have been detected in some events, for example, FRB 150807 [69] and FRB 121102 [70]. For the FRB 150807, the origin of its scintillation is probably from weak scattering in the IGM or host galaxy [69] (see Figure 2.3). In the case of the FRB 121102, in the Reference [24] the authors found scale structure consistent with Galactic interstellar scintillation.

2.1.4 Plasma lensing

The definition of plasma is very controversial, it means that plasma is not necessarily a gas that contains a significant fraction of charged particles, but it can be also constituted of neutral particles. For this reason, we can use the two basic

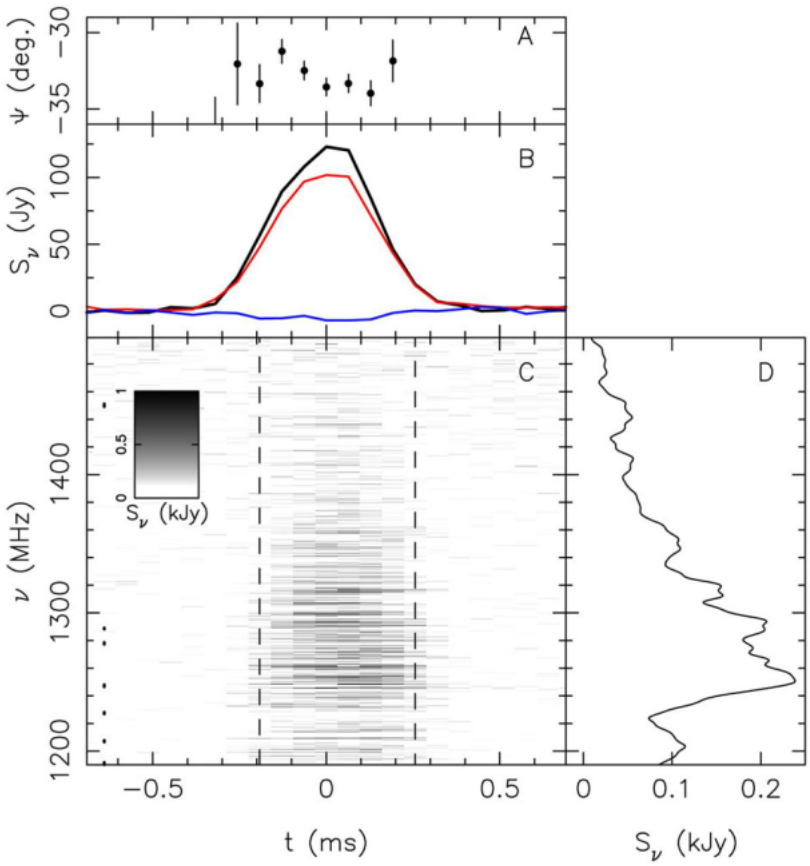

Figure 2.3: Apparent scintillation seen in FRB 150807. **c** A dedispersed dynamic spectrum of the burst at 390 kHz spectral resolution. The inferred scintillation bandwidth is 100 ± 50 kHz. **b** The frequency-averaged burst profile with total intensity (black), linearly polarized signal (red), and circularly polarized signal (blue). **a** The polarization angle across the burst, and **d** a smoothed version of the burst spectrum. **Credit:**[3]

necessary (but not sufficient) properties of the plasma to explain it. The first one is the presence of freely moving charged particles. The second is the large number of these particles.

Another characteristic of plasma is to be a dispersive medium with refractive index $n_p = \sqrt{1 - \omega_p^2/\omega^2}$, where ω is the source frequency and ω_p is the plasma frequency defined in Eq. 2.2. In the case of $\omega > \omega_p$, the radio waves will propagate in the plasma and be deflected by a certain angle, called the deflection angle. In this situation, the plasma acts as a lens, similar to a gravitational lens.

The effects of plasma on the gravitational lens system can be studied by introducing an extra deflection angle into the framework of gravitational lens theory (a detailed explanation about it can be found in References [71, 72]). This extra deflection angle depends on the frequency and position of the source, unlike gravitational lensing [73]. The plasma can also cause strong magnification (caustic spots) if the lensed image appears close to the center of the lens [74].

Plasma lensing may be relevant for FRBs in many aspects. In Reference [75], the authors consider the relevance of such an effect for understanding both the spectra and apparent luminosity of FRBs. In the case of Reference [76], the plasma effect in the gravitational lens system can cause a significant frequency-dependent time delay effect affecting the inferred DM. For this reason, the plasma lensing effect may affect the interpretation of the FRBs properties and the distribution of the population.

2.1.5 Polarization

Polarization describes the behavior of the electric field vector ($\vec{E}$) of the radio waves with respect to time. In the case of the FRBs, the polarization properties can vary significantly among bursts [3] and it seems that most FRBs have strongly polarized emission [11]. However, some FRBs present apparent low polarization and it might be intrinsic or could be due to large Faraday rotation measures in these sources (the case of FRB 121102A [4]).

The Faraday rotation effect is the rotation of the polarization direction of linearly polarized radio waves under the influence of a magnetic field. The degree of rotation is measured by the rotation by rotation measure (RM) defined as

$$\mathrm{RM} = -0.81 \int_0^d \frac{B_\parallel(l) n_e(l)}{(1+z)^2} dl, \tag{2.24}$$

where $B_\parallel(l)$ is the magnetic field parallel to the line of sight and n_e is the density of free electrons along the line of sight. RM is quote in units of rad/m^2.

About the signal of RM, when it is positive the magnetic field direction is towards the observer, and when it is negative, it is inversely.

As was mentioned, the polarization features of FRB vary from burst to burst. The FRB 121102 and FRB 180916 are repeaters and present a polarization nearly 100% linearly polarized with a flat polarization angle (PA) curve [4, 24, 77–79]. In Figure 2.4 we note that the PA remains constant across each burst for FRB 121102. In the case of non-repeaters like FRB 181112 and FRB 190102, they are usually partially linearly or circularly polarized and their PAs vary significantly with time [80, 81]. The way that the difference in polarization affects the classification of FRBs by repeating or not is not well understood because the polarization properties of FRBs vary from case to case.

2.1.6 Absorption

Along the propagation path from the source to the Earth, the radio waves can suffer various scattering or absorption processes. The important processes of absorption that attenuate the radio waves emission are free-free absorption and external

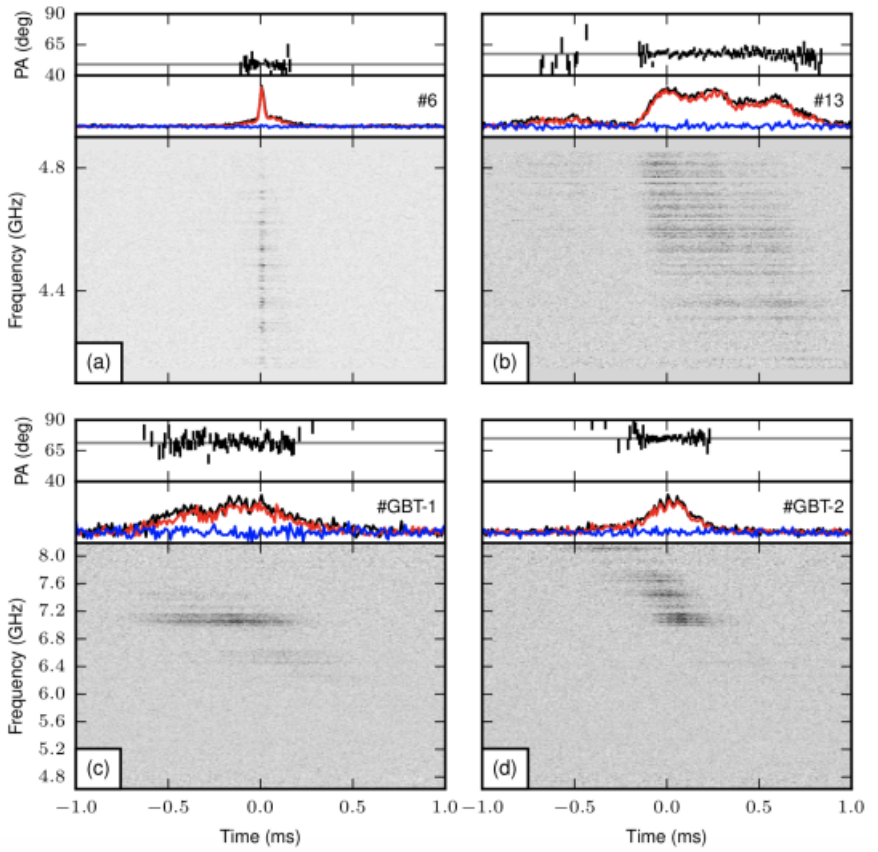

Figure 2.4: Polarization angles seen in FRB 121102. A grey horizontal line indicates the average PA of each burst. The red and blue lines indicate linear and circular polarization profiles, respectively, while the black line is the total intensity. **Credit:**[4]

synchrotron absorption [11].

The free-free absorption is a very important process in the radio band and occurs when a free electron gains energy during a collision with an ion by absorbing a photon. The free-free absorption is the inverse of free-free emission (or bremsstrahlung). Such absorption process becomes important when the plasma density in the vicinity of the FRB source is high enough.

In the case of external synchrotron absorption, which is the inverse of synchrotron radiation, happens when a photon interacts with a charge in a magnetic field and is absorbed. The signal of FRBs close to a persistent radio source could be absorbed via synchrotron absorption.

It is unclear whether the low-energy cutoff in some bursts like the FRB 180916 [82, 83] and FRB 200125A [84], is caused by absorption or intrinsic FRB radiation spectrum [23, 85]. However, a general constraint on the intrinsic spectrum can be given for particular bursts [5].

2.2 Emission mechanisms

In this section, we will comment on mechanisms of radiation emission for FRBs, which is an important topic in the astrophysical scenario. One of the challenges of theoretical models is finding a physical mechanism that can explain the amount of energy radiated over such short timescales. However, such high brightness temperature ($T_b > 10^{32}$ K) and short duration (milliseconds or less) of FRBs bursts imply a coherent emission process. It means that the emission cannot be explained in terms of individual particles radiating independently (incoherently) of each other [86–88]. In coherence emission, the particles emit radiation in phase with each other. There are many coherent radio emission models in the literature to explain FRB emission (see Reference [11] for a discussion about coherence emission models), but here we will present three models to generate coherence: i) emission by bunches (also known as antenna mechanism); ii) relativistic plasma emission (also called as plasma masers); iii) kinetic instability or maser emission. For the last one, many versions have been proposed for FRBs, including: plasma synchrotron maser, vacuum maser, and synchrotron maser from magnetized shocks, being these three the versions that we will discuss in this section.

2.2.1 Coherent curvature emission

For the coherent curvature emission by bunches, this mechanism has been discussed in the case of pulsar radio emission [89], in which the bunched particles radiate coherently in curved field lines to produce the radio emission from the inner magnetosphere. Such mechanism has been also discuss for FRBs fields for some authors [90–95]. In this scenario, the emitting particles are physically clustered in six-dimensional phase space, being 3-D position space and 3-D momentum space. In order to introduce the theory about emission by bunches, first we will explore such emission in the case of a single charge. Then, we will generalize for a bunched particles. Here we will follow Reference [56] to explain synchrotron radiation.

Single charge

In vacuum, a relativistic electron (e) with Lorentz factor γ in the presence of a magnetic field ($\mathbf{B}$) has a helicoidal trajectory: with constant velocity $v_\parallel$ along the direction of $\mathbf{B}$, and spiraling around the magnetic field line. Such electron radiates the synchrotron radiation with a characteristic frequency called as Larmor frequency that is defined as [56]:

$$\omega_B = \frac{eB}{\gamma mc}, \tag{2.25}$$

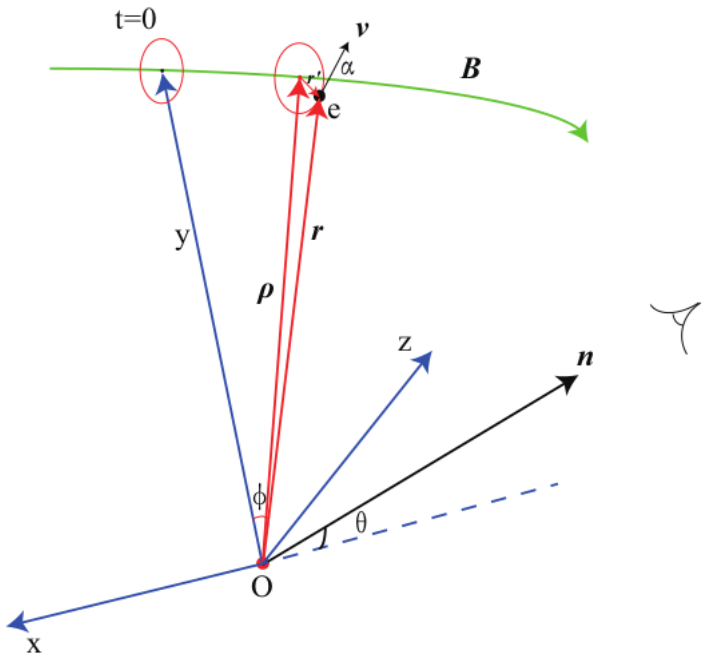

Figure 2.5: Schematic picture of synchro-curvature radiation. **Credit:**[5]

where $\gamma \equiv (1-\beta^2)^{-1/2}$ is the Lorentz factor, $\beta = \boldsymbol{v}/c$ and m is the electron mass.

In the case of particles with larger perpendicular velocities ($v_\perp$), they will spiral around magnetic field lines with a larger Larmor radius (or gyro-radius)

$$r_B = \frac{v_\perp}{\omega_B} = \frac{\gamma\beta mc^2}{eB}\sin\alpha. \tag{2.26}$$

And the energy radiated per unit solid angle per unit frequency interval of a moving charge is [56]

$$\frac{dE}{d\omega d\Omega} = \frac{e^2\omega^2}{4\pi^2 c}\left|\int_{-\infty}^{+\infty}\hat{n}\times\left(\hat{n}\times\vec{\beta}\right)e^{i\omega(t-\hat{n}\cdot\vec{r}(t)/c)}dt\right|^2, \tag{2.27}$$

being $\hat{n}$ the unit vector pointing to the observer that makes an angle θ with x-axis and Ω_0 the angular velocity of the guiding center along the magnetic field line.

Since the field lines are usually curved, particles will radiate when they accelerate in the curved trajectory and the realistic emission of relativistic electrons can be generalized as synchro-curvature emission, which is illustrated in Fig 2.5 [11]. Thus, let us consider such field along ϕ-direction being $\mathbf{B} = B_\phi e_\phi$ with curvature radius ρ. We also defined α as the angle between the velocity of the particle $\boldsymbol{v}$ and $\mathbf{B}$.

We can obtain the characteristic frequency and radiation spectrum of synchro-curvature radiation by calculating the integral in Equation 2.27. In Reference [96], in order to simplify the calculation of the spectrum, the authors assumed that the magnetic field lines are uniform in the length scale $\sim 2r_c^*/\gamma$ in which the light pulse is formed. Here r_c^* is the effective radius of curvature and we will define it later.

They also assumed that the observer is located on the (x, z)-plane without loss of generality.

The radiation is concentrated within a narrow cone centered in the direction of motion and the characteristic frequency is

$$\omega_c = \frac{3}{2}\gamma^3 \frac{c}{\rho}\left[\frac{(r_B^3 + \rho r_B^2 - 3 r_B \rho^2)}{\rho r_B^2}\cos^4\alpha + \frac{3\rho}{r_B}\cos^2\alpha + \frac{\rho^2}{r_B^2}\sin^4\alpha\right]. \tag{2.28}$$

The total radiation power spectrum is given by (for more details about the calculation, see Reference [96])

$$\begin{aligned}\frac{dP}{d\omega} &= \frac{\sqrt{3}e^2\gamma}{4\pi r_c^*}\frac{\omega}{\omega_c}\left\{\left[\int_{\omega/\omega_c}^{\infty} K_{5/3}(y)d(y) - K_{2/3}\left(\frac{\omega}{\omega_c}\right)\right]\right. \\ &+ \left.\frac{1}{r_c^{*^2} Q_2^2}\left[K_{2/3}\left(\frac{\omega}{\omega_c}\right) + \int_{\omega/\omega_c}^{\infty} K_{5/3}(y)d(y)\right]\right\},\end{aligned} \tag{2.29}$$

where $r_c^* \approx c^2/[r_B\omega_B^2 + (\rho + r_B)\Omega_0^2]$, K_i are modified Bessel functions of second kind and

$$Q_2^2 \equiv \frac{1}{r_B}\left(\frac{r_B^2 + \rho r_B - 3\rho^2}{\rho^3}\cos^3\alpha\cos\theta + \frac{3}{\rho}\cos\alpha\cos\theta + \frac{1}{r_B}\sin^3\alpha\sin\theta\right). \tag{2.30}$$

Considering the limit of $\rho \longrightarrow \infty$, $\alpha \neq 0$, $\Omega = 0$, $Q_2 = \sin^2\alpha/r_B$ and $r_c^{*^2}Q_2^2 = 1$ the characteristic frequency (Eq. 2.28) becomes the characteristic frequency synchrotron radiation

$$\begin{aligned}\omega_c &= \frac{3}{2}\gamma^3\omega_c\sin\alpha, \\ \frac{dP}{d\omega} &= \frac{\sqrt{3}e^2\gamma\omega_B\sin\alpha}{2\pi c}\frac{\omega}{\omega_c}\int_{\omega/\omega_c}^{\infty} K_{5/3}(y)d(y).\end{aligned} \tag{2.31}$$

In the limit case $\alpha = 0$, $r_B = 0$, $\Omega_0 = c/\rho$, $Q_2 = 1/\rho$ and $r_c^{*^2}Q_2^2 = 1$ we have a pure curvature radiation

$$\begin{aligned}\omega_c &= \frac{3}{2}\gamma^3\frac{c}{\rho}, \\ \frac{dP}{d\omega} &= \frac{\sqrt{3}e^2\gamma}{2\pi\rho}\frac{\omega}{\omega_c}\int_{\omega/\omega_c}^{\infty} K_{5/3}(y)d(y).\end{aligned} \tag{2.32}$$

Bunched particles

Now we can generalize the radiation spectrum considering a bunch of N particles

in the magnetosphere. If the phases of electromagnetic waves emitted by each individual electron are near the same, the coherence can be reached [5]. Then, following Equation 2.27 we can obtain the total radiation intensity of N electrons

$$\frac{dE_{\rm tot}}{d\omega d\Omega} = \frac{e^2\omega^2}{4\pi^2 c}\left|\int_{-\infty}^{+\infty}\sum_{j}^{N}\hat{n}\times\left(\hat{n}\times\vec{\beta_j}\right)e^{i\omega(t-\hat{n}\cdot\vec{r}_j(t)/c)}dt\right|^2, \tag{2.33}$$

where the subscript j represents the j-th electron.

In Reference [94], the authors simplified the above integration assuming some issues for it and here we will present their important results. They considered a one-dimensional (1-D) bunch with finite length L moving along a magnetic field line of curvature radius ρ. So the position vector from the j-th electron to the first one is $\Delta\vec{r}_j(t) = \vec{r}_j(t) - \vec{r}(t)$. Since the emission is highly beamed, this vector could be considered as time-independent and Eq. 2.33 can be rewritten as

$$\frac{dE_{\rm tot}}{d\omega d\Omega} \simeq \frac{e^2\omega^2}{4\pi^2 c}\left|\int_{-\infty}^{+\infty}\hat{n}\times\left(\hat{n}\times\vec{\beta_j}\right)e^{i\omega(t-\hat{n}\cdot\vec{r}(t)/c)}dt\right|^2 \times \left|\sum_{j}^{N}e^{-i\omega(\vec{n}\cdot\Delta\vec{r}_j/c)}\right|^2. \tag{2.34}$$

The last term in the above equation is called as the phase stacking, $F_\omega \equiv \left|\sum_j^N e^{-i\omega(\vec{n}\cdot\Delta\vec{r}_j/c)}\right|^2$, and can be evaluated analytically. For example, if all the electrons are at one point, e.g., $\Delta\vec{r}_j \simeq 0$, one has $F_\omega(N) = N^2$, which means that the spectrum has the same shape with the single charge, but is enhanced by a factor of N^2.

If we define a typical frequency $\omega_L = 2c/(L\cos\theta)$, being θ the observing angle, and obtained

$$F_\omega \simeq \begin{cases} N^2, & \omega << \omega_L, \\ N^2\left(\frac{\omega}{\omega_L}\right)^2, & \omega_L << \omega << \omega_m, \end{cases} \tag{2.35}$$

where $\omega_m \sim (\rho/L)^2\omega_L$ is a frequency boundary beyond which the emission becomes incoherent. For example, if we assume that the electrons have a power-law distribution, i.e., $N_e(\gamma) \propto \gamma^{-p}$, where $\gamma_m < \gamma < \gamma_{max}$, the resulting radiation spectrum has a break at $\omega_m \equiv \omega_c(\gamma_m)$ give by Equation 2.32 (the complete analytical expressions can be found in Reference [94]).

Although coherent emission mechanism by bunches has long been explored in the case of pulsar radio emission [97, 98], it remains controversial how the bunches could form effectively [99–101].

2.2.2 Relativistic plasma emission

In the plasma emission mechanism, which is a multi-stage process, some agent generates plasma turbulence that grows with time and can not escape directly from the source, and this turbulence leads to escaping in the form of electromagnetic waves in the radio band through some secondary process. In this scenario, the first stage of such mechanism is the generation of Langmuir waves (longitudinal electron plasma wave) by a streaming instability (electron stream) and then partial conversion of the wave energy into escaping radiation at the fundamental (F) and second harmonic (H) of the plasma frequency (see Reference [88] for a recent review about coherent emission by plasma).

The generation of Langmuir turbulence could occur when a beam of relativistic particles runs into a background plasma. The growth rate of beam instability depends on the dispersive properties of the plasma and should be relatively fast to ensure effective plasma emission [5].

Observationally, plasma emission is circularly polarized and an important qualitative result concerning the polarization is that conventional F emission processes produce radiation between the plasma frequency, given in Equation 2.2, and the cutoff frequency of the x mode [88, 102],

$$\omega_x = \frac{\Omega_e}{2} + \left(\omega_p^2 + \frac{\Omega_e^2}{4}\right)^{1/2}, \tag{2.36}$$

being $\Omega_e = eB/m_e$ the cyclotron frequency.

There are two main difficulties for this mechanism. First, it remains questionable if Langmuir waves through beam instabilities can be generated in the magnetosphere of neutron stars [103]. Second, usually, the growth rates for beam instabilities seem too small to allow effective wave growth [88].

2.2.3 Masers emission

The radiation emission mechanism by masers (microwave amplification by stimulated emission of radiation) corresponds to a 'negative absorption' of electromagnetic waves detached from the plasma, which causes a growth of amplitude of emission. Here we will discuss three models that invoke relativistic shocks to generate coherent radio emission.

I) Plasma synchrotron maser

This mechanism is a plasma version of synchrotron self-absorption [56] and can happen when the emitted synchrotron radio waves propagate in a weakly magnetized relativistic plasma with $\omega_B << \omega_p$.

The self-absorption coefficient (μ), that is the ratio of self-absorbed line intensity to intensity without self-absorption, can be written as [56, 104–106]:

$$\mu = -\frac{c^2}{8\pi\nu^2}\int_0^\infty E^2 \frac{dP}{d\nu}\frac{d}{dE}\left[\frac{N(E)}{E^2}\right]dE, \tag{2.37}$$

where $N(E)$ is the energy spectrum of the relativistic electrons and $E = \gamma m_e c^2$ is the electron energy. μ is positive in the case of relativistic electrons spiraling around the magnetic field in vacuum. The synchrotron masers can be realized for a specific distribution of relativistic electrons spiraling around the magnetic field in a cold plasma and in this case, μ is negative. A direct requirement is that the energy distribution of electrons grows faster than E^2, $\frac{d}{dE}\left[\frac{N(E}{E^2}\right] > 0$, and this means that population inversion [1] is necessary.

In an isotropic and sufficiently dilute plasma, for which $\omega_B/\omega << 1$, the synchrotron radiation power in the presence of a background plasma is [105, 106]:

$$\frac{dP}{d\omega} = \frac{\sqrt{3}e^2\gamma\omega_B \sin\alpha}{2\pi c\sqrt{1+\gamma^2\frac{\omega_p^2}{\omega^2}}}\frac{\omega}{\omega_c^{'}}\int_{\omega/\omega_c^{'}}^\infty K_{5/3}(x)dx, \tag{2.38}$$

being the critical frequency:

$$\omega_c^{'} = \frac{3}{2}\gamma^3\omega_B\sin\alpha\left(1+\gamma^2\frac{\omega_p^2}{\omega^2}\right)^{-3/2}. \tag{2.39}$$

In the limit of $\gamma^2\omega_p^2/\omega^2 << 1$, Equations 2.38 and 2.39 turn back to Equation 2.31.

Now let us consider the case when the influence of the ambient plasma on synchrotron radiation is significant, in which γ and ω_p are large. Replacing Equations 2.38 and 2.39 into 2.37, we obtain [106]

$$\mu \propto E^{-2}\frac{d}{dE}\left[E^2\frac{dP}{d\omega}\right] \propto z^2\Phi(z), \tag{2.40}$$

where

$$z = \frac{\omega}{\omega_c'} \simeq \frac{2}{3}\frac{\omega_p^3}{\omega^2\omega_B\sin\alpha}, \tag{2.41}$$

and

$$\Phi(z) = 2z\int_z^\infty K_{5/3}(x)dx - z^2K_{5/3}(z). \tag{2.42}$$

The function $\Phi(z)$ is positive in the low energy region $z < 1.35$ and in this energy

[1] Population inversion will occur when the number of excited electrons exceeds the number of electrons in the ground state. In this scenario, the rate of stimulated emission exceeds absorption and the radiation can be amplified [26].

range, the μ is always positive. On the other hand, $\Phi(z)$ is negative at high energies $z > 1.35$ and in this case, the μ is negative.

The specific intensity I_ω of electromagnetic radiation emitted by a homogeneous source of linear size L containing a system of relativistic electrons is

$$I_\omega = \frac{a_\omega}{\mu}\left[1 - e^{-\tau}\right], \tag{2.43}$$

being $a_\omega = \int (dP/d\omega)N(E)dE$ the emissivity and $\tau = \mu L$ the optical depth. As long as μ is negative and $|\mu|L >> 1$, that is achieved only for a narrow range of frequencies (maser emission has a narrow spectra), the radiation intensity is amplified exponentially [106]

$$I_\omega \simeq \frac{j_\omega}{|\mu|} e^{|\mu|L}, \tag{2.44}$$

indicating that a significant fraction of electron energy is converted to the strong synchrotron maser emission.

For plasma synchrotron maser to be in the radio band and to be a possible mechanism for FRBs, the B-field strength should be smaller than $\sim 10^3$G [92, 107].

II) Vacuum maser

This mechanism is a synchrotron emission in which the plasma effect is not important and for this reason is called as vacuum synchrotron maser. In this model is considered the possibility of a negative absorption (Eq. 2.37) when the distribution particles function has population inversion [92, 107]. In Reference [108], the authors showed that negative curvature absorption is possible when the magnetic field lines have torsion. So at some certain observing angle (θ), the self-absorption coefficient can be negative [5].

The emissivity for a single electron can be written as [56, 92]

$$\begin{aligned} j_\nu(\theta) \equiv \frac{dP}{d\nu d\Omega} &= \frac{9cB^2\sigma_T}{64\pi^4\nu_B}\left(\frac{\nu}{\nu_c}\right)^2\left(1+\gamma^2\theta^2\right) \\ &\times \left[\left(1+\gamma^2\theta^2\right)K^2_{5/3}(y) + \gamma^2\theta^2 K^2_{1/3}(y)\right], \end{aligned} \tag{2.45}$$

where $\nu_B = \omega_B/2\pi$, $\nu_c = \omega_c/2\pi$ and $y \equiv \nu/(2\nu_c)\cdot(1+\gamma^2\theta^2)^{3/2}$. The absorption coefficient in function of θ is given by

$$\mu(\theta) = \frac{1}{2m_e\nu^2}\int_1^\infty \frac{N(\gamma)}{\gamma p}\frac{\partial}{\partial\gamma}\left[\gamma p j_\nu(\theta)\right]dy, \tag{2.46}$$

being the electron momentum $p = (\gamma^2 - 1)^{1/2}$ in units of $m_e c$.

The differential absorption cross-section is directly related to the emissivity and is defined as [92]

$$\frac{d\sigma_s(\theta)}{d\Omega} = \frac{1}{2m_e\nu^2}\frac{1}{\gamma p}\frac{\partial}{\partial\gamma}\left[\gamma p j_\nu(\theta)\right]. \tag{2.47}$$

Replacing the expression for $j_\nu(\theta)$ (Equation 2.45) into above equation and considering $t \equiv \gamma^2\theta^2$, we obtain

$$\begin{aligned}\frac{d\sigma_s(\theta)}{d\Omega} &= \frac{2e}{9B}\frac{1}{\gamma^4\sin^2\alpha}\Big\{(13t-11)(1+t)K_{2/3}^2 + t(11t-1)K_{1/3}^2(y) - 6y(t-2) \\ &\times \left[(1+t)K_{2/3}(y)K_{5/3}(y) + tK_{1/3}(y)K_{4/3}(y)\right]\Big\}. \end{aligned}\tag{2.48}$$

If both conditions $\theta > \sqrt{2}/\gamma$ and $\nu/\nu_c >> (\gamma\theta)^{-3}$ are satisfied, the cross section is negative. The maser emission can be observed outside the $1/\gamma$ emission cone of the relativistic electrons [107].

This mechanism can explain coherent radio emission, but the model presents some issues that could make it impossible to be realized in nature. The problems of the model include how to maintain extremely ordered B-field (within $1/\gamma$ angle), how to accelerate particles to maintain a narrow pitch angle distribution (again within $1/\gamma$ angle) and how to accelerate particles to maintain a narrow energy distribution [11].

III) Synchrotron maser from magnetized shocks

This mechanism was introduced to explain FRBs emission in 2014 by the author in Reference [109] and can be understood as synchrotron maser emission that is generated by relativistic magnetized shock waves. As the shock propagates into the magnetized medium, the particles will achieve bunching gyrating around the magnetic field lines, forming a ring in the momentum space. Then, they radiate coherently at gyration frequency $\sim \omega_B^{'} = eB^{'}/(m_e c)$ [5, 11].

The physics of this mechanism shall be addressed by particle-in-cell numerical simulations (PIC) [110, 111]. However, here we will follow the Reference [5] (based on Reference [112]) and present the results of 1-D PIC simulations.

Let us first consider an ideal magnetohydrodynamics (MHD) plasma, that can be defined as a plasma represented by a single fluid with infinite electrical conductivity and zero ion gyro radius (for more explanations about MHD plasma, see Reference [113]). We will assume that the number density (N), proper energy density (e), proper pressure (p), as well as the electromagnetic fields $\mathbf{E}$ and $\mathbf{B}$, are assumed constants and uniform upstream and downstream of a thin shock layer that propagates with a (positive) constant velocity ($\beta_{\rm shock}$) toward the negative x-direction.

The conservation of particle number, energy, momentum, and magnetic flux can be defined, respectively, as [112]

$$\frac{N_2}{N_1} = \frac{1+\beta_{\rm shock}}{\beta_{\rm shock}}, \tag{2.49}$$

$$(1+\beta_{\rm shock})N_1 m\gamma_1 c^2(1+\sigma) = \beta_{\rm shock}\left(e_2 + \frac{B_2^2}{8\pi}\right), \tag{2.50}$$

$$(1+\beta_{\rm shock})N_1 m\gamma_1 c^2(1+\sigma) = p_2 + \frac{B_2^2}{8\pi} \tag{2.51}$$

$$\frac{B_2}{B_1} = \frac{1+\beta_{\rm shock}}{\beta_{\rm shock}}, \tag{2.52}$$

where the subscripts 1 and 2 refer to the upstream and downstream regions, respectively. The upstream is assumed to be ultrarelativistic ($\beta_1 \approx 1$) and that the shock is strong, the upstream thermal pressure is negligible ($p_1 \approx 0$ and $e_1 \approx n_1 mc^2$). For the downstream fluid, it is assumed the equation of state of an ultrarelativistic hot gas

$$e_2 \approx \frac{p_2}{(\Gamma-1)}, \tag{2.53}$$

being Γ the appropriate adiabatic index.

Introducing the magnetization parameter $\sigma = \frac{B_1^2}{4\pi N_1 mc^2\gamma_1}$, being σ an invariant under Lorentz transformations perpendicular to the magnetic field, we can obtain the equation for shock velocity from Equations 2.50 and 2.51 and using the Equation 2.53:

$$\left(1+\frac{1}{\sigma}\right)\beta_{\rm shock}^2 - \left[\frac{\Gamma}{2} + \frac{1}{\sigma}(\Gamma-1)\right]\beta_{\rm shock} - \left(1-\frac{\Gamma}{2}\right) = 0, \tag{2.54}$$

which has solution

$$\begin{aligned}\beta_{\rm shock} &= \frac{1}{2(1+1/\sigma)}\Bigg\{\left(\frac{\Gamma}{2}+\frac{\Gamma-1}{\sigma}\right) + \Bigg[\left(\frac{\Gamma}{2}+\frac{\Gamma-1}{\sigma}\right)^2 + 4\left(1-\frac{\Gamma}{2}\right) \\ &\times \left(1+\frac{1}{\sigma}\right)\Bigg]^{1/2}\Bigg\}.\end{aligned} \tag{2.55}$$

The ratio of shock jump is

$$\frac{N_2}{N_1} = \frac{B_2}{B_1} = 1 + \frac{1}{\beta_{\rm shock}}, \tag{2.56}$$

$$\frac{kT^2}{m\gamma_1 c^2} = \beta_{\rm shock}\left[1+\sigma\left(1-\frac{1+\beta_{\rm shock}}{2\beta_{\rm shock}^2}\right)\right], \tag{2.57}$$

being T_2 the temperature of downstream plasma. The downstream density, temperature, and magnetic field intensity are then obtained by substituting Equation 2.55

in the above equations.

However, the authors showed [112] that the measured value of N_2/N_1 is considerably higher and the measured downstream temperatures are systematically lower than the predictions of the ideal MHD shock jump conditions. These deviations can be due to the fact that the ideal MHD formalism does not account for the additional wave fluctuations that can dissipate the flow energy. So the solution is to modify shock jump conditions taking into account the energy and momentum in emitted waves.

The upstream field fluctuations are due to the electromagnetic (EM) precursor [2], which can be expressed with a parameter ξ

$$\frac{1}{8\pi}\left\langle \delta E_1^2 + \delta B_1^2 \right\rangle \approx -\frac{1}{4\pi}\left\langle \delta E_1 \delta B_1 \right\rangle \equiv \frac{1}{4\pi}\xi B_1^2. \tag{2.58}$$

In the case of downstream, there are two sub-dominant fluctuations, EM and electrostatic, that can be described in terms of parameters ζ and η, respectively,

$$\frac{1}{8\pi}\left\langle \delta E_2^2 + \delta B_2^2 \right\rangle \equiv \frac{1}{4\pi}\zeta B_1^2 \tag{2.59}$$

$$\frac{1}{8\pi}\left\langle \delta E_{es2}^2 \right\rangle \equiv \frac{1}{4\pi}\eta B_1^2. \tag{2.60}$$

While the equations for the conservation of particle number (2.49) and magnetic flux (2.52) remain unchanged, we can rewrite the equations of energy and momentum conservation (Eq. 2.50 and 2.51) taking into account the modifications in Eq. 2.58, 2.59 and 2.60

$$\begin{aligned} N_1 m\gamma_1 c^2(1+\beta_{\rm shock}) + \frac{1}{4\pi}B_1^2\left[(1+\beta_{\rm shock}) - \xi(1-\beta_{\rm shock})\right] \\ = \left[e_2 + \frac{1}{8\pi}B_2^2 + \frac{1}{4\pi}(\zeta+\eta)B_1^2\right]\beta_{\rm shock}, \end{aligned} \tag{2.61}$$

$$\begin{aligned} \left(N_1 m\gamma_1 c^2 + \frac{1}{4\pi}B_1^2\right)(1+\beta_{\rm shock}) + \frac{1}{4\pi}\xi B_1^2(1-\beta_{\rm shock}) \\ = p_2 + \frac{1}{8\pi}B_2^2 + \frac{1}{4\pi}(\zeta-\eta)B_1^2. \end{aligned} \tag{2.62}$$

Again using the Equation of State (2.53) to eliminate e_2 between (2.61) and

[2]The EM signal occurs before the radiation from downstream plasma, for this reason is called as precursor [5].

(2.62), one obtains an equation for $\beta_{\rm shock}$

$$\left(1+\frac{1}{\sigma}-\xi\right)\beta_{\rm shock}^3 + \left[(2-\Gamma)\left(\frac{1}{2}+\frac{1}{\sigma}+\xi-\zeta\right)+\Gamma\eta\right]\beta_{\rm shock}^2 - \left[1+(\Gamma-1)\left(\frac{1}{\sigma}-\xi\right)\right]\beta_{\rm shock}^3 - \frac{2-\Gamma}{2}=0. \quad (2.63)$$

The form of density jump (Eq. 2.56) remains the same, but the downstream temperature (Eq. 2.57) is now

$$\frac{kT_2}{m\gamma_1 c^2} = \beta_{\rm shock}\left[1+\sigma\left(1-\frac{1+\beta_{\rm shock}}{2\beta_{\rm shock}^2}\right)\right] + \frac{\sigma\beta_{\rm shock}}{1+\beta_{\rm shock}}[\xi(1-\beta_{\rm shock})-\zeta+\eta]. \quad (2.64)$$

From the energy conservation equation (2.61), it can be seen that the fraction of the total incoming upstream energy that is radiated away in the precursor and the total incoming energy that is transformed into each type of downstream wave are given by relations, respectively:

$$f_\xi \equiv \frac{\xi}{1+1/\sigma}\frac{1-\beta_{\rm shock}}{1+\beta_{\rm shock}} = \frac{\xi}{1+1/\sigma}\left(1-\frac{2N_1}{N_2}\right), \quad (2.65)$$

$$f_{\zeta,\eta} \equiv \frac{\zeta,\eta}{1+1/\sigma}\frac{\beta_{\rm shock}}{1+\beta_{\rm shock}} = \frac{\zeta,\eta}{1+1/\sigma}\frac{N_1}{N_2}. \quad (2.66)$$

For the simulations results obtained by the authors in Reference [112], the typical values for the efficiency are also much smaller ($f_\xi >> f_{\zeta,\eta}$), so that the downstream waves are much less significant than the precursor in the overall shock energetic. f_ξ has a peak value around 10% at $\sigma \sim 0.1$, and increasing σ leads to decreasing f_ξ. In Reference [110], the authors showed the following: i) for a very high magnetization $\sigma >> 1$, f_ξ has an asymptotic form of $7\times10^{-4}/\sigma^2$; ii) and the spectrum of EM precursor peaks at $\omega_{\rm peak} \simeq 3\omega_p \max[1,\sqrt{\sigma}]$ and is relatively narrow-banded with $\Delta\omega/\omega_{\rm peak} \sim$ a few.

In Reference [109], the author suggested that the FRB emission is probably just this kind of EM precursor. However, as well as plasma synchrotron masers, synchrotron masers from magnetized shocks suffer from the problem of low radiation efficiency.

2.3 Progenitor models

Many models have been proposed to explain the FRBs progenitors (see [26] for a detailed review of source models). However, since the FRB 200428 [27] was discovered to be associated with active magnetars, these models have been more explored as FRB sources in the literature. The FRBs progenitor models can be divided in several ways: repeating or non-repeating; long-lived or cataclysmic source, being the last one associated with non-repeating events; rotationally or magnetically powered; etc. Since there are more than 50 FRB source models discussed in the literature, here we will briefly discuss some examples of three types of progenitor models: neutron star models, non-neutron star models, and cataclysmic models. All these models except the last one discuss sources for repeating FRBs.

2.3.1 Neutron star progenitors

The large rotational energy and strong magnetic fields make the neutron stars (NSs) (see [114] for a recent review about NS) good potential candidates for progenitors of FRBs.

Magnetars

Magnetars are the majority of current FRB progenitor theories. We can define magnetars [115–117] as being a class of young and highly magnetized ($\sim 10^{34}$ G) NS. They can be observed as soft γ-ray repeaters (SGRs) and anomalous x-ray (AXPs), being both spinning down, without exception [117]. The current population consists of 30 magnetars known [117], but they represent at least 10% of the young NS population.

These models were suggested as FRBs progenitors for the first time by authors [118], who considered the Lorimer burst as SGR hyperflares. Since then many authors have proposed theories involving magnetars being FRBs sources within different contexts (see Reference [11] for a list of works). However, these versions of the magnetar models have the following common ingredients: energy budget and energy loss. The first one is associated with two energy reservoirs: the rotation energy of the magnetar and the magnetic energy of the magnetar. In the case of the energy loss, the average FRB emission luminosity should be bound by the average energy loss/dissipation rate of the magnetar.

The radiation mechanism invoked to produce FRB emission can differ in several aspects between the magnetar models. The bunched curvature radiation (discussed in the previous Section 2.2), bunched inverse Compton scattering [119], free electron laser [120], or direct EM generation due to non-uniform pair production [121, 122]

have been proposed for various versions of the magnetar models.

Other isolated neutron star models

Although magnetars models are the majority, there are other models of isolated NS suggested as the source of FRBs.

I) Giant pulses from young pulsars:

Giant pulses (GPs) [123] are short-duration bursts of individual radio pulses emitted from pulsars, in which the peak flux density of GPs can exceed the peak flux density of regular pulses in hundreds and even thousands of orders of magnitude. GPs have been observed in both millisecond pulsars and young pulsars.

GPs from young pulsars have been proposed as FRBs source [124–126]. However, GPs could only be detected up ~ 100 Mpc and not at cosmological distances, while most FRBs originate from cosmological distances (> 100 Mpc). For this reason, this model is not capable of interpreting the observational properties of FRBs unless much brighter GPs are invoked.

II) Pulsar lightening:

The authors in Reference [127] argued that there are phenomenological similarities between FRBs and atmosphere lightening and conjectured that FRB may occur in neutron star magnetospheres whose plasma is believed to be divided by vacuum gaps. In this model, the limitation of FRB energetics is associated with the spin-down power of the underlying pulsar.

Interacting neutron star models

Some FRB models involve NS interaction with an external agent (its environment or a less massive object), in which the models present different energy budgets to explain FRB bursts. The FRB emission is generated in the NS magnetosphere or through a reaction from an interaction of the two bodies.

I) Cosmic comb:

This model [128] invokes an interaction between an astrophysical plasma stream from a nearby source of a foreground regular pulsar, in which the ram pressure of the stream is greater than the magnetic pressure of the pulsar magnetosphere. The sources of the stream may originate from energetic events such as SNe, GRB, or NS merger events or more moderate events such as AGN flare or even a stellar flare from a binary companion of the pulsar. In this scenario, an FRB signal is observed when the "combed" magnetosphere sweeps across the line of sight.

II) Binary cosmic comb:

Binary comb model [129] proposes that FRBs are produced by a highly magnetized pulsar, whose magnetic field is "combed" by the strong wind from a companion

star, either a massive star or a millisecond pulsar. The interaction between the companion and the NS perturbs the FRB pulsar magnetosphere and may trigger the emission of FRBs, being the role of the companion is no longer to directly provide the power of FRBs.

2.3.2 Non-neutron star progenitors

I) Stellar-mass black hole sources:

Stellar mass black holes (BH) are the only other kind of objects whose sizes are small enough to accommodate the millisecond duration of FRBs, like NS, being the difference between these two objects their engine. BH may or may not have a clean magnetosphere as NS does because of the dirty accretion environment, so the magnetospheric radiation mechanisms associated with NS models may not be straightforwardly applied [11].

There are many models in the literature that explain the origin of FRBs from a system composed of a BH. For instance, the authors in References [130–132] suggested that FRB originate in the accretion disc funnels of intermediate mass black holes, in which the FRB emission site and the coherent radiation mechanism did not be specified. While the authors [133, 134] proposed models that the accreting stellar-mass BH binary systems produce FRB bursts via the synchrotron maser mechanism as the radiation mechanism.

II) Supermassive black hole sources:

Supermassive black holes (SMBH) are a class of BH with a mass greater than $10^5 M\odot$ existent at the centre of galaxies or AGNs. Since SMBH has a characteristic timescale $r_s/c \sim 10^3$s $(M/10^8 M\odot)$ (where $r_s = 2GM/c^2$ is the Schwarzschild radius of a black hole with mass M) much longer than milliseconds, it is natural to invoke models that involve a SMBH as a source of FRB burst (emission is confined in a region much smaller than the event horizon). In References [135, 136], the authors proposed a model that a turbulent plasma hit by an AGN relativistic jet can emit short bursts consistent with the ones observed in FRBs. The emission is generated by the interaction of the electrons with cavitons, which are the result of beam-excited Langmuir turbulence in a plasma traversed by the jet, resulting in coherent radiation.

2.3.3 Cataclysmic progenitors

Although only a few FRBs have been observed to repeat, being the majority of FRBs non-repeating, it is not possible to prove that a non-repeating will ever repeat. For this reason, the cataclysmic events are not taken seriously. There are also two problems involving these models: i) the energy budget of FRBs is much smaller than

the energy available in this type of events; ii) the FRB event rate density is much greater than the rate densities of all known cataclysmic events [137]. The cataclysmic models that are more attractive are those destined to produce brief electromagnetic radiation signals, being them blitzars and compact binary coalescence models.

I) Blitzars:

The blitzar model [138] invokes the implosion of supermassive neutron stars (SMNSs) to power an FRB. More specifically, in this model, an isolated and magnetized NS massive enough, whose non-spinning mass already exceeds the maximum NS mass allowed by the NS Equation of State, will inevitably collapse to a BH as it is spun down via magnetic dipolar radiation or even gravitational wave radiation [11]. During the collapse, the magnetic field lines previously anchored on the surface of the star can either follow it as the surface is trapped behind the event horizon, snapping violently. Furthermore, the traveling large-scale magnetic shock that propagates outwards can accelerate free electrons which will produce radio signals dissipating the radiated energy [138, 139].

II) Compact binary coalescence:

Compact binary coalescence (CBC) are binary system composed of two compact objects that are so close to each other to merge, being these the members of such system white dwarfs (WDs), NSs, BHs, and their combinations, e.g., black hole–neutron star binary (BH-NS) systems. Such models have been proposed as one of the main scenarios to explain the origin of some non-repeating FRBs [140].

In Reference [141], the authors proposed, as the source of FRB a binary white-dwarf mergers, in which the burst are produced by coherent emission from the polar region of a rapidly rotating, magnetized massive WD formed after the merger.

In the case of binary BHs (BBH) and binary NSs (BNs) systems, a way of such merger power an FRB is if at least one of the members of the binary system carries a certain amount of charge (NSs as spinning magnets, are guaranteed to be charge) [142, 143]. So both dipole electric radiation and dipole magnetic radiation would be emitted from the system during the inspiral phase. The emission powers increase sharply at the final phase of the coalescence. This would produce a brief electromagnetic signal, which may manifest itself as an FRB if coherent radio emission can be produced from the global magnetosphere of the system [142, 143].

For binary NSs (BNS) mergers, there are several proposals to explain the origin of some non-repeating FRBs. A way of such merger produces a FRB signal is from synchronization of the magnetosphere of the two NSs shortly after the merger that can power bright coherent radio emission in a manner similar to radio pulsars [144]. If the BNS merger product is a SMNS [145, 146], the FRB burst can be powered by the blitzar [138]. If the BNS merger results in a stable massive magnetar, the standard magnetar mechanism may operate and power repeating FRBs.

2.4 Summary

In this chapter, we presented the physical theory of the FRBs. We discussed about the propagation effects that can affect the radio waves along the path from the source to the observer in the Earth. We also showed how we can obtain the observed and derived properties of FRBs from these propagation effects, being the dispersion measure the fundamental property in the application of FRBs in cosmology, when we combine it with the redshift.

We also presented five models of radio emission that can generate coherent emission processes, but it is unclear which mechanism is responsible for the brightness, duration, spectrum, pulse spectrum, polarization, repetition, and periodicity of FRBs. Currently, the coherent curvature emission and synchrotron maser emission from magnetized shocks are in the leading position.

We discussed about some examples of FRB source models, in which the magnetars models are leading in the position of isolated NS to power repeating FRBs. In the case of non-neutron stars, stellar mass BH are good model. And if the non-repeating FRBs exist, blitzars, and CBCs are the best guesses.

Chapter 3

Observational aspects of FRBs

When a FRB is detected, the next important step that is very challenging is to infer the intrinsic physical properties of the FRB. Such information can give important clues about the progenitor. For this reason, in this chapter, we will present observational features of FRBs, explaining the basic idea of techniques to observe a FRB and its population features.

3.1 Radiation fundamentals

Firstly, we introduce some basic concepts of radiation in astronomy, following the Reference [6]. A source is studied by measuring the strength of its radiation as a function of direction in the sky (by mapping or imaging) and frequency (spectroscopy). It is also possible to measure other quantities from the source, like time and polarization. In the case of FRBs, it is possible to measure directly from the observations its sky position, duration of the burst, DM (see Section 2.1.1), and fluence. Such concepts are essential to understand how the parameters of a FRB are determined.

3.1.1 Brightness and intensity

Let us consider the simplest possible case of radiation traveling from a source through empty space. It means that there is no absorption, scattering, or emission along the path from the source to an observer on the Earth. Now we construct an area dA normal to the direction of the given ray (where is placed a detector in the Earth), where all rays passing through doing an angle θ and whose direction is within a solid angle $d\Omega$ of the given ray, which is illustrated Figure 3.1.

If the energy dE from within the solid angle $d\Omega$ flows through the projected area

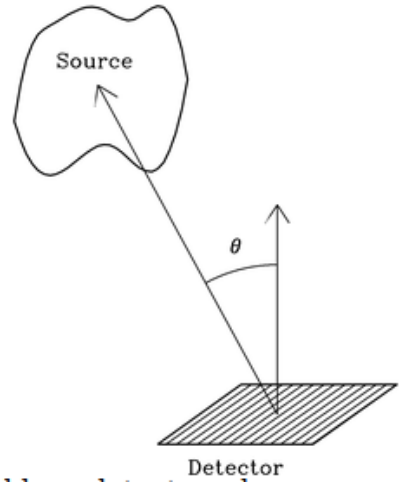

Figure 3.1: Specific intensity measured by a detector whose normal is at an angle θ from the line of sight. **Credit:** [6]

$\cos\theta dA$ in time dt and in a narrow frequency band of width $d\nu$, then

$$dE = I_\nu \cos\theta \, dA \, dt \, d\Omega \, d\nu, \tag{3.1}$$

where I_ν is the specific intensity or brightness.

Now let us introduce the definition of the specific intensity or brightness being the number of photons falling on the detector in the Earth per unit area per unit time per unit solid angle, which can be written in terms of the power ($dP = dE/dT$) as:

$$I_\nu = \frac{dP}{\cos\theta \, dA \, d\Omega \, d\nu}, \tag{3.2}$$

being the specific brightness is quoted in units of $\mathrm{Wm^2Hz^{-1}sr^{-1}}$. Note that I_ν depends on location in space, on direction, and on frequency.

If we integrate Equation 3.2 over all frequencies, we will obtain the total (integrated) intensity

$$I = \int_0^\infty I_\nu d\nu. \tag{3.3}$$

Now consider a ray of length r in which dA_1 and dA_2 are two infinitesimal surfaces along it. The energy is conserved, so the energy carried by that set of rays passing through both dA_1 and dA_2 can be expressed as

$$I_{\nu_1} \cos\theta_1 \, dA_1 \, dt \, d\Omega_1 \, d\nu = I_{\nu_2} \cos\theta_2 \, dA_2 \, dt \, d\Omega_2 \, d\nu. \tag{3.4}$$

For $d\Omega_1 << 1$ rad, it can be the solid angle subtended by dA_2 as seen from the center of the surface dA_1. The same is valid for $d\Omega_2 << 1$ rad, which can be the

solid angle subtended by dA_1 as seen from the center of the surface dA_2. So we can replace the relations

$$d\Omega_1 = \frac{\cos\theta_2 dA_2}{r^2},$$
$$d\Omega_2 = \frac{\cos\theta_1 dA_1}{r^2},$$

in Equation 3.4 and obtain

$$I_{\nu_1} = I_{\nu_2}. \tag{3.5}$$

The above relation implies that the specific intensity is conserved along a ray and it leads to two important consequences: i) brightness is not dependent on distance; and, ii) brightness is the same at the source and the observer.

3.1.2 Flux

Now let us consider the source at distance r from the observer on the Earth where there is a detector, which is illustrated in Figure 3.2.

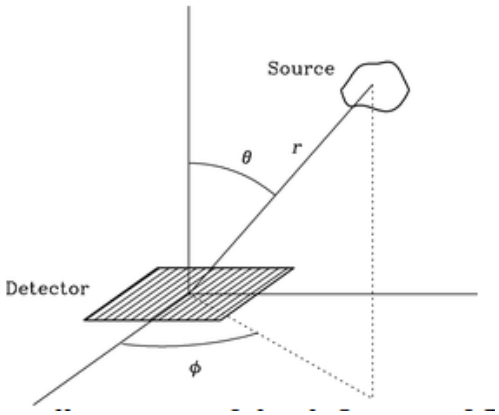

Figure 3.2: An illustration of the definition of flux density. **Credit:** [6]

If the source is discrete, it means: that if the source subtends a well-defined solid angle, we can define the flux density ($\mathcal{S}_\nu$) as being a measure of power carried by all rays passing through a given area. We can write the flux density from Equation 3.1 integrating over the solid angle subtended by the source

$$\mathcal{S}_\nu \equiv \int_{source} I_\nu(\theta,\phi)\cos\theta\, d\Omega, \tag{3.6}$$

where $\mathcal{S}_\nu$ cam be measured in $\mathrm{Wm^{-2}Hz^{-1}}$. The usual unit used for flux density in radio astronomy is Jansky unit, where 1 Jy = 10^{-26} $\mathrm{Wm^{-2}Hz^{-1}}$.

We can also write the total flux or flux from a source integrating the flux density over frequency

$$\mathcal{S} \equiv \int_0^\infty \mathcal{S}_\nu \, d\nu, \tag{3.7}$$

being quoted in units of Wm^{-2}.

Note that, unlike specific intensity or brightness that is an intrinsic property of a source, the flux density of a source is not, because it depends on the distance between the source and the observer.

3.1.3 Luminosity

The next important quantity to describe the radiation from an astrophysical source is the luminosity. So let us define the spectral luminosity L_ν of a source as the total power per united bandwidth radiated by the source at frequency ν

$$L_\nu = \int_{source} \mathcal{S}_\nu \, dA, \tag{3.8}$$

begin L_ν usually quoted in units of WHz^{-1}.

If we consider the area being the area of a sphere of radius d, where $\int_{source} dA = 4\pi d^2$, the spectral luminosity in the function of flux density of an isotropic source radiating in free space will be

$$L_\nu = 4\pi d^2 \mathcal{S}_\nu, \tag{3.9}$$

where the distance d between the source and the observer is much larger than the dimensions of the source itself. Note that L_ν is an intrinsic property of the source because it does not depend on the distance d between the source and the observer ($\mathcal{S}_\nu \propto d^{-2}$).

The total luminosity of a source is defined as the integral over all frequencies of the spectral luminosity:

$$L \equiv \int_0^\infty L_\nu \, d\nu, \tag{3.10}$$

which has the dimension of W.

3.1.4 Fluence

The last quantity of radiated source that we will introduce is the fluence. We can define the fluence ($\mathcal{F}$) being the amount of energy received over time duration of the burst and it is usually quoted in units of $\mathrm{Jm}^{-2}\mathrm{Hz}^{-1}$. So we can write the specific fluence in terms of the flux density from the relation

$$\mathcal{F}_\nu = \int_{burst} \mathcal{S}_\nu \, dt. \tag{3.11}$$

We can rewrite the above equation considering the expression for spectral luminosity (Eq. 3.9)

$$\mathcal{F}_\nu = \frac{1}{4\pi d^2} \int_{burst} L_\nu \, dt, \tag{3.12}$$

where $\int_{source} L_\nu \, dt$ is the definition of specific energy (E_μ). Then we obtain a final expression for specific fluence in terms of the energy received from the source

$$\mathcal{F}_\nu = \frac{E}{4\pi d^2}. \tag{3.13}$$

Now, the total fluence can be obtained by integrating the specific fluence over frequency:

$$\mathcal{F} \equiv \int_0^\infty \mathcal{F}_\nu \, d\nu, \tag{3.14}$$

which has dimension of Jm^{-2}.

3.2 Observational techniques

The radio band has a very broad spectrum: it spans between 10 MHz and 1 THz at the low-frequency end of the electromagnetic spectrum. Because of that: (i) major types of astronomical sources, thermal and nonthermal radiation mechanisms, and propagation phenomena can be observed at radio frequency; and (ii) a wide variety of radio telescopes and observing techniques are needed to cover the radio window effectively [6]. For this reason, in the following section, we will focus on how we search for and discover FRBs using two types of radio telescopes: single-dish and interferometric. We will also briefly discuss how the observed properties of FRBs can be determined.

3.2.1 Data capture

The radio telescopes can measure the electromagnetic waves from the sky as a function of time using feeds. The antenna and feed response are typically measured over a radio frequency range, called as bandwidth, which is amplified and discretely sampled by a number of frequency channels. These data can be saved to a disk and the resulting data cube contains the intensities at each time and frequency channel. Searching for dispersed pulses in these data cubes requires several steps, but in the end, the total intensity data is analyzed to produce a list of candidate FRB signals [3].

3.2.2 Preliminary radio frequency interference excision

Artificial radio frequency interference (RFI) is an issue in radio astronomical data because it will be mixed with the desired signal (see [147–149] for more details about RFI), overwhelming the intensity of the source and matching some of the expected properties to masquerade as an astrophysical signal. RFI can have a broad or narrow band and can be persistent or impulsive. Usually in the searches for FRBs, the first step is to remove or mitigate RFI before searching for the signal in the data.

The most common approaches involve masking time samples and frequency channels, masking as much RFI as possible without removing any real data. The frequency channels can be automatically masked when there are known in-band artificial emitters. Additionally, the data cube can be searched for impulsive RFI by looking for peaks in the DM = 0 pc/cm^3 time series (where dispersed astrophysical bursts should be smeared out) and masking the contaminated time samples. One can also subtract the DM = 0 pc/cm^3 time series from the time series at higher DM trials [3].

3.2.3 Dedispersion

The DM of a new observed FRB is not known at the first moment, for this reason, it is necessary to search for a large number of DM trials. Since narrowband signals could be missed in the case that DM is not sufficiently close to one of trial DM values, a fine spacing of trials is required.

Instrumental broadening of the signal within a single-frequency channel can be calculated as

$$\Delta t_{\mathrm{DM}} = 8.3 \times 10^6 \ \mathrm{DM} \ \Delta\nu_{ch} \ \nu^{-3} \ \mathrm{ms}, \tag{3.15}$$

where ν and $\Delta\nu_{ch}$ are the observing frequency and channel bandwidth, respectively, and are both in MHz. The next step in the sequence is the choice of a DM trial that should be sensitive to a dispersed pulse that never drops below a specified level. However, this process comes with an added computational cost.

The dedispersion corresponds to the process that corrects DM to maximize the signal-to-noise ratio (S/N) of the FRB signal. Such a process is the most computationally expensive step in a single-pulse search and it is a very important task to reduce this complexity. There are several implementations of dedispersion algorithms that are commonly used and here we will follow the authors in Reference [3], listing two main categories: incoherent and coherent dedispersion.

Incoherent dedispersion: This implementation applies corrections to individual frequency channels and its accuracy depends on the bandwidth of individual frequency channels. After the calculation of the dispersion delay across a band-

width for a given DM (see Section 3.2.9 to know how to calculate it), the delay is subtracted from each frequency channel to arrive at a channelized dataset with propagation delays removed. This kind of implementation is usually applied when the DM of the signal is not known at the first moment, such as in the cases of FRBs searches that search thousands of DM trials.

Coherent dedispersion: Unlike the incoherent dedispersion, coherent dedispersion implementation recovers the intrinsic shape of the signal and it is assumed that there is no significant scattering. This is achieved by operating on raw voltage data. The ISM effects on the signal can be modeled as a filter, and the reverse filtering operation can be applied in the Fourier domain [3]. The impulse response of the ISM filter depends on the bandwidth of the observations and the DM of the signal. Then it is possible to recover the high-resolution pulsed signal. Such implementation is only applied for a single value, when the DM of the is already known, such as in the case of a repeating FRB.

3.2.4 Time series

The next step for each DM trial of incoherent dedispersion is to sum the data over all frequencies in a way that follows the dispersive sweep. In the case of coherent dedispersion, the data are summed in each time sample. The times series is a one-dimensional array of total signal versus time resulting in integrated intensity, where astrophysical signals can be searched.

However, before the search for astrophysical signals, it is necessary to remove a stable baseline from the times series, because the mean signal level can vary due to instrumental effects and RFI. This variation can result in a non-uniform baseline in the times series, affecting the extraction of the signal. The baseline can be measured by calculating the running median (or mean) of the time series, clipping outliers above a specified threshold, and then re-calculating the median [3, 147–149].

3.2.5 Normalization

In order to estimate the S/N of the FRB signal [3], first it is necessary to determine the noise properties. To do that some FRB search codes first calculate the median absolute deviation (MAD) and then estimate the noise as rms = $k\times$ MAD, where k is the scale factor. In the case of Gaussian noise, which is typically valid for radio data in the absence of strong RFI, $k \simeq 1.4826$. Then, the S/N can be calculated in a single time sample x as S/N = timeseries(x)/rms.

3.2.6 Matched filtering

In the cases in which the data is wider than a single time sample, the time series are convolved to find the FRB signal in these data using a boxcar function of width W for multiple trial pulse durations. On the other hand, for a pulse duration greater than a single time sample, the S/N must be normalized by the boxcar width such that S/N = timeseries(x)/(rms $\times\sqrt{W}$). Peaks in the time series (dedispersed, normalized, and boxcar-convolved) are usually reported as candidates are typically reported as candidates.

3.2.7 Candidate classification

After the identification of the single-pulse candidates in the times series, candidate grouping should be performed to match the single pulse events with promising candidates. One way to group the candidates is by a machine learning-based approach that will automatically identify and classify single pulses in candidate data [150].

3.2.8 Localizing the burst

When a burst signal is detected in the beam formed data (defined as the field of view of the radio telescope, which is typically diffraction limited), the raw data (data that has not been beam-formed) will be saved, including its spatial information. The raw data can be correlated and imaged in order to localize the burst. This means that the burst can be localized to the host galaxy, and possibly to regions within the host galaxy.

3.2.9 Dispersion measure and fluence

As we mentioned before, the dispersion measure and fluence of FRBs bursts are considered observational properties because both quantities can be determined directly from the observations. The amount of dispersion is calculated by the relation of the time delay of the burst

$$\Delta t = \frac{e^2}{2\pi m_e c}(\nu_1^{-2} - \nu_2^{-2})\text{DM} \approx 4.15(\nu_1^{-2} - \nu_2^{-2})\text{DM ms}, \tag{3.16}$$

where ν_1 and ν_2 are the lowest and highest radio frequencies of the observation, respectively, in units of GHz. In practice, the DM can be measured with a precision of about 0.1 pc/cm^3, depending on the observational setup and S/N.

After the DM value has been optimized and S/N maximized, the intensity can be converted to flux density as a function of time $\mathcal{S}(t)$, and the pulse can be charac-

terized in terms of its width and peak flux density ($\mathcal{S}_{peak}$). For a signal of arbitrary shape, it is also common to quote the equivalent width W_{eq} of a top-hat pulse with the same $\mathcal{S}_{peak}$. Then the burst has an energy or fluence

$$\mathcal{F} = W_{eq}\,\mathcal{S}_{peak} = \int_{source} \mathcal{S}(t)dt. \tag{3.17}$$

Due to the non-uniform sensitivity of the beam, most non-repeating FRB fluxes and fluences determined so far are lower limits.

3.2.10 Radio telescopes

At the beginning of this section, we mentioned that the radio band is very wide (five decades in wavelength) and for this reason, there are different types of radio telescopes and many of these have been observing FRBs (the radio telescopes that search for FRBs and the number of detected events are listed in [1]).

Single-dish

Single-dish radio telescopes are basically circular paraboloidal reflector that focuses incoming radio frequency energy onto a detector. For these types of radio telescopes, its limiting sensitivity is inversely proportional to the effective area. The diameter of the dish (D) determines the size of the telescope half power beam width [6]

$$\theta_{\mathrm{HPBW}} \simeq 1.22\frac{\lambda}{D}, \tag{3.18}$$

where λ is the observed wavelength.

Single dishes offer raw sensitivity and broad frequency coverage (using a suite of receivers) to study FRB emission. The advantages of single dishes in FRB searches include: their large collecting areas (and thus high sensitivity) and low signal processing complexity; their large focus cabins are useful for studying FRB emission and polarization; and, their sensitivity makes them ideal to follow up other bursts of repeating FRBs. On the other hand, the greatest disadvantage of such telescopes is their poor localization of an FRB discovery.

There are several single dishes radio telescopes searching for FRBs around the world, but here we will present three examples that have more highlights. The first example is the radio telescope that discovered the first FRB the *Parkes* telescope [151] that has an area of the dish equal to 64 m. The second is *Arecibo* telescope [152] that was the world's largest single-aperture telescope for 53 years, because it had a 305 m spherical reflector dish. Finally, the last one is the Five-hundred-meter

[1] https://blinkverse.alkaidos.cn/

Aperture Spherical radio Telescope (*FAST*) [153], being currently the world's largest single-dish radio telescope with a diameter dish of the spherical reflector is 500 m.

Interferometers

Interferometers are a type of radio telescope that are composed of many antennas or dishes, whose signals are combined to achieve the resolution of a single large telescope with a diameter equivalent to the longest baseline.

The use of interferometers to search for FRBs can be done in a variety of ways [154]. In the case of incoherent searches, the phase information is discarded and the individual element intensities are summed; these have the advantage of large fields-of-view (equal to the primary field of view of the elements), but sensitivity scales as $\sqrt{N}$ for N elements and poor localization precision. For the coherent searches, these cases create tied-array beams (TABs) by applying differential weights to different elements and summing the signals in phase; in this case, sensitivity scales as N, leading to an improvement of both sensitivity and localization. One issue associated with beam-forming with many elements is the high computational complexity because such case requires a powerful hardware [155].

The advantages of using these types of radio telescopes to detect FRBs are their flexible nature in terms of pointing, localizing, and beam-forming, particularly if voltage data are recorded from each element upon detection of an FRB. On the other hand, combining data streams from many elements requires enormous computational power and large data rates.

About the interferometers radio telescopes searching for FRBs, there are many of them with different sizes and shapes. Here we will point to the Australian Square Kilometre Array Pathfinder (*ASKAP*) [156] and the Canadian Hydrogen Intensity Mapping Experiment (*CHIME*) [157]. ASKAP consists of 36 identical dish antennas, each 12 m in diameter, working together as a single astronomical interferometer. It was responsible for identifying the second FRB host galaxy, the FRB 180924 [158]. CHIME consists of four antennas consisting of 100×20 m cylindrical parabolic reflectors. It has collected by far the largest sample of bursts, detecting well over ~ 1000 FRBs bursts.

3.3 Population study

In Section 2.1 we presented several properties of FRBs derived from the propagates effects of radio waves. Now, we will discuss general properties obtained directly from observations, including the host galaxy and the luminosity distribution, in which we will present the energy and brightness of FRBs. With the new

surveys, it is expected that the number of FRBs will increase and for this reason, the understanding of observational properties becomes very important, because it will help us: to optimize future FRB searches, to classify and compare with model predictions, giving constraints on the progenitor.

3.3.1 Spectral properties

As was mentioned before, the FRBs have so far only been detected in the radio band within the range from 110 MHz [23] to at least 8 GHz [24]. The bursts were first exploited at the L-band at frequencies around 1.4 GHz because several available facilities can observe at these frequencies and archival data. The repeating FRB 121102A was first observed at frequency 1.5 GHz [9] and, currently, is the FRB which has been observed at higher frequencies, with detections up to 8 GHz [24].

The non-detection of FRBs at lower frequencies could be explained due to an intrinsic hardening of the spectrum at low frequencies related to a certain absorption process [159]. On the other hand, the non-detection of bursts at higher frequencies could be assigned to limited sensitivity [160], because single dishes are not extremely well suited for surveys of the entire sky that is the needed for FRBs, or the difficulty to achieve strong coherence. The range of the observed emission has been extended by CHIME [77, 161] with its first discoveries to frequencies down to 400 MHz, and they made it clear that emissions at low frequencies were not exceptions.

The spectral shape of FRBs was initially not well measured and thought to be flat due to the burst detection at high frequencies. The simplest way to fit the spectral shape is to approximate it to a power-law function $F_\nu \propto \nu^{-\alpha}$, where α is the power-law index that was observed to vary according to the situation. For example, the power-law index for Lorimer burst [1] and for FRB 110523A [162] is $\alpha = 4 \pm 1$ and $\alpha = 7.8 \pm 0.4$, respectively. In the case of repeating FRBs, it is possible that the same source has α varying for different bursts. For example, for FRB 121102A the α values of bursts ranged from -10.4 to $+13.6$ [8], and this large variation may be the indication that the intrinsic spectrum of FRBs is narrow.

The search of some repeater bursts using multi-telescopes often shows that the bursts detected in one band are not detected in another, that is the case of FRB 121102A [160] and FRB 180916B [85], suggesting that the spectra of these bursts are not simple power laws. Indeed, the dynamical spectra of FRBs often show that the bursts are bright only in part of the whole observing bandpass, which we can see dynamic spectra of FRB 121102A in Figure 3.3. For example, it was observed for FRB 200428 two bursts by CHIME [163], but only the second one with higher peak frequency was detected by STARE2 [27], which has a higher bandpass than CHIME, indicating that the FRB spectra could be narrow.

The FAST performer a deep-search of the spectral properties of more than 700 bursts from FRB 201124A [164] suggests that the majority of repeating FRBs have narrow spectra, with the typical spectral bandwidth of ~ 275 MHz.

3.3.2 Repeating and non-repeating

Currently, we can divide FRBs into two groups: repeating and non-repeating and there are more than 60 FRBs reported to repeat (see [2] for a list of repeating events). Generally, a FRB is identified as repeating when a second burst or more is detected in the same position of the sky, that means from the same source. A remaining question is about the existence of non-repeating FRB sources because it is quite possible that all FRBs repeat with a wide range of repetition rate and the next generation of survey telescopes will place constraints on the existence of such population.

The first FRB identified as a repeater is the FRB 121102, whose first burst was observed in 2014 by the Arecibo telescope [165]. In 2016, the Arecibo telescope detected 10 new bursts of FRB 121102 [8], in which some bursts had a different spectrum being substantially brighter compared with the first-detected burst. In Figure 3.4 we note such a difference between 11 bursts of FRB 121102.

There are three main factors that influence the identification of a repeating FRB, making it appear to be non-repeating. i) The first one is the selection bias of the receiver. In the case of the second burst, if it has a pulse width close to the instrumental sampling or smearing timescale, then this signal is probably being missed [166, 167]. ii) The second factor is the energy distribution function of individual FRBs. If the second burst is much dimmer than the original one, it may fall below the detection threshold. For example, in the case of FRB 171019, two bursts have been detected ~ 590 fainter than the discovered burst [168]. iii) And last, the statistics of repeating sources could differ for each repeater. For instance, the waiting time for several FRBs may be much longer than those of the frequent repeaters like the case of FRB 121102 which we will discuss in the next section.

Although several works disfavored a single population showing that there are some differences in the observational properties, including burst morphology, between repeaters and apparent non-repeating FRBs, the question about all FRBs being repeaters still in debate and the answer to this question is not simple [166]. The authors in Reference [25, 77, 169] showed that repeaters tend to have a narrower spectrum and wider widths than the other group. Another important aspect reported by [7, 161] was the fact that several repeating FRBs presented a frequency down-drift. The authors [170] and [171] applied supervised and unsupervised ma-

[2] https://blinkverse.alkaidos.cn/

chine learning algorithms, respectively, on the first CHIME FRB catalog [25] and both obtained that repeaters and non-repeating seem to have a different origin.

The observation of repeaters provides very important information about the origin of FRBs: these bursts cannot come from a cataclysmic event and whatever is producing the bursts must be able to sustain this activity over a period of many years. Another important aspect provided by the repeaters is that these bursts make it possible to precisely localize its source using a radio telescope.

3.3.3 Periodicity

The periodicity of repeating FRBs is a new property that was discovered in early 2020 and has been searched extensively. The early targeted periods in the searches were similar to the periods of known pulsars and magnetars, within the range from milliseconds to seconds. However, several works search the periodicity in this period range for the repeaters FRB 121102A [9, 172, 173] and FRB 201124A [10, 174, 175], but they obtained null results, suggesting that rotating neutron star are not progenitors of FRB bursts.

Unlike what was initially thought, it was found that some repeating sources present very long periods or active cycles, that is the case of FRB 180916 observed by CHIME with a period of $\sim$ 16 days and active window of $\sim$ 5 days [176]. The duration and phase of the active window seem to be frequency-dependent, with the windows appearing earlier in phase and being narrower at higher frequencies [23, 85]. In the case of FRB 121102A, long-term monitoring revealed a possible long-term period of $\sim$ 160 days [177, 178]. On the other hand, the search for the FRB 201124A global periodicity was not found [175].

The authors in References [9, 10, 164, 174, 175] showed an interesting feature about the waiting time of active repeaters, that is the bursts of a repeating FRB source present two distinct peaks, as we can see in Figure 3.5. The first peak is around milliseconds and the exact value depends on how distinct bursts are defined. The second peak actually depends on the activity level of the source, ranging from 10s of seconds to 100s of seconds, even for the same source at different epochs [11].

Several models have been proposed to explain the periodical activity of FRBs and here we will present two main hypotheses, which both involve a highly magnetized neutron star, known as magnetar, being the FRB source (see Reference [179] for details about both models). In the first, the periodicity is the result of the orbital motion of a binary system, composed of magnetar and its companion can be an O/B type star or a compact object, that has a strong wind that obscures the FRB radiation, except through a rather narrow channel [129, 180]. However, this model was ruled out by the authors [85], because it predicts a wider activity window

for higher frequencies. The second model associates the periodicity with the free precession of the magnetar due to a slight non-spherical deformation of the magnetar [181, 182].

The information that some repeating FRBs have a periodicity raises the question if all repeaters have periodicity and more observations are needed to answer this question.

3.3.4 Host galaxy

Although more than 1000 bursts have been detected, only it was possible to identify the host galaxy of a few of these events, being a very important aspect in the study of FRBs. The host galaxies of FRBs play a very important role in the understanding of the environment and origin of FRBs, because the properties of the host galaxy can give clues about the progenitors of FRBs.

The first FRB with a host galaxy identified was the repeating FRB 121102 detected by Arecibo telescope [165, 183]. The FRB was localized to a low-metallicity, dwarf star-forming galaxy, being the source of the bursts located in an active star formation region of the host galaxy [184, 185]. Such type of galaxy is a common host of superluminous supernovae (SLSNe) and long gamma-ray bursts (LGRB), which were previously hypothesized to be powered by the electromagnetic spin-down of newly-formed, strongly-magnetized neutron stars with millisecond birth rotation periods ('millisecond magnetars') [185]. For this reason, young active magnetars have been suggested as FRBs burst progenitors [184, 185]. On the other hand, the repeating FRB 201124A [186] has a Milky Way-like massive host galaxy with a high star formation rate [187–189], being inconsistent with the environment expected for SLSNe and LGRB.

In the case of non-repeating FRBs, its localization is a big challenge, because it is difficult to precise its location in real-time using the initial discovery burst. However, several non-repeating events have also been localized (for more details see Table 3.1 that we will comment on in the next paragraphs). For instance, the FRB 190523 was localized using the Deep Synoptic Array ten-antenna prototype (DAS-10) at $z = 0.66$ [137, 190]. Unlike FRB 121102A, most part of non-repeating FRBs apparently are not located in an active star formation region [190, 191].

The global properties of FRBs indicate SNe type II as a progenitor of the bursts, but all of them are not inconsistent with being produced by magnetar engines and multiple formation channels are also possible [192].

Another important aspect in the identification of the host galaxy is related to the fact that we can use the well-localized (with redshift) FRBs to study cosmology. When the origin of the burst is confirmed, the host galaxy can be identified, and

the redshift of the event can be measured directly. Then, it is possible to combine the dispersion measure with the redshift to obtain DM $- z$ relation [29]. From this relation, the FRBs can be used to constrain cosmological and astrophysical parameters and test aspects of fundamental physics (for recent reviews about FRBs as cosmological probes, see References [3, 5, 11]).

The most up-to-date FRB data set currently available has 39 well-localized events of FRBs (for an overview of the observed events see References [193, 194] and the databases [3][4], respectively) within the redshift range $0 \lesssim z \lesssim 1$. In Table 3.1 we listed all of them with their main properties: name, redshift, the Galaxy contribution ($\mathrm{DM_{MW,ISM}}$) estimated from the NE2001 model [59], observed dispersion measure ($\mathrm{DM_{obs}}$) and $\mathrm{DM_{obs}}$ uncertainty (σ_{obs}). Since there is no universal convention to name FRBs repeating sources, we added the prefix 'r' before the FRB name to specify that. In the next chapter, when we present our methodology for our analysis, we will show which of these FRBs we need to remove and explain the reason for doing this.

The current FRBs sample is not large enough, but we are expecting that the number of well-localized FRBs will increase with the new instruments that are being built to localize FRBs in the next few years. Among these are the coherent upgrade CRACO system of ASKAP [51], the CHIME outriggers [52], and the Square Kilometre Array (SKA) [53].

3.3.5 Luminosity, energy, and brightness temperature

After the identification of the host galaxy and consequently direct measurement of the redshift, the isotropic-equivalent energy and peak luminosity of FRBs can be determined precisely. However, the best estimate of such quantities depends on the spectral shape of the FRB.

In the case of FRBs that have a narrow-band spectra with emission contained within the telescope observing band, which is the most common case of bursts from repeaters (e.q. [164]), it is more appropriate to multiply the bandwidth $\Delta\nu$ by the specific flux to obtain luminosity. On the other hand, for FRBs with a broad-band spectra with the emission extending beyond the telescope observing band, which is the case of some non-repeating FRBs (e.g. [1]), it is more appropriate to multiply the band central frequency ν_c by the specific flux to obtain luminosity [207]. The isotropic peak luminosity, defined at the beginning of this chapter (given by Eq.

[3]https://www.herta-experiment.org/frbstats/
[4]https://blinkverse.alkaidos.cn/

Name	Redshift z	$DM_{MW,ISM}$ [pc/cm^3]	DM_{obs} [pc/cm^3]	σ_{obs} [pc/cm^3]	Reference
rFRB 121102A	0.19273	188.0	557.0	2.0	[183]
FRB 171020A	0.0087	37.0	114	0.2	[195]
rFRB 180301A	0.3305	152.0	536.0	8.0	[196]
rFRB 180916B	0.0337	200.0	348.8	0.2	[197]
rFRB 180924B	0.3214	40.5	361.42	0.06	[158]
FRB 181030	0.0039	41.0	103.5	0.3	[198]
FRB 181112A	0.4755	102.0	589.27	0.03	[199]
FRB 190102C	0.291	57.3	363.6	0.3	[191]
rFRB 190520B	0.241	60.0	1204.7	4.0	[200]
FRB 190523A	0.66	37.0	760.8	0.6	[137, 190]
FRB 190608B	0.1178	37.2	338.7	0.5	[201]
FRB 190611B	0.378	57.83	321.4	0.2	[190]
FRB 190614	~ 0.6	83.5	959.2	0.5	[202]
rFRB 190711A	0.522	56.4	593.1	0.4	[190]
FRB 190714A	0.2365	38.0	504.13	2.0	[190]
FRB 191001A	0.234	44.7	506.92	0.04	[190]
FRB 191228A	0.2432	33.0	297.5	0.05	[196]
rFRB 200120E	$\sim$ -0.0001	40.0	87.75	0.5	[203]
FRB 200430A	0.16	27.0	380.25	0.4	[190]
FRB 200906A	0.3688	36.0	577.8	0.02	[196]
rFRB 201124A	0.098	123.2	413.52	0.5	[186]
FRB 210117	0.2145	34.4	730.0	1.0	[204]
FRB 210320	0.2797	42.2	384.8	0.3	[204]
FRB 211127	0.0469	42.5	234.83	0.08	[205]
FRB 211212	0.0715	27.1	206.0	5.0	[205]
FRB 220207C	0.043040	79.3	262.38	0.01	[206]
FRB 220307B	0.248123	135.7	499.27	0.06	[206]
FRB 220310F	0.477958	45.4	462.24	0.005	[206]
FRB 220319D	0.011228	133.3	110.98	0.02	[206]
FRB 220418A	0.622000	37.6	623.25	0.01	[206]
FRB 220506D	0.30039	89.1	396.97	0.02	[206]
FRB 220509G	0.089400	55.2	269.53	0.02	[206]
FRB 220610A	1.016	31.0	1458.15	0.2	[12]
FRB 220825A	0.241397	79.7	651.24	0.06	[206]
FRB 220914A	0.113900	55.2	631.28	0.04	[206]
FRB 220920A	0.158239	40.3	314.99	0.01	[206]
FRB 221012A	0.284669	54.4	441.08	0.7	[206]

Table 3.1: Properties of the most up-to-date FRB data set with known host galaxies

3.9), can be written as [11]

$$L_p \simeq 4\pi d_L^2 \mathcal{S}_{\nu,p} \begin{cases} \Delta\nu, & \text{(narrow spectrum)} \\ \nu_c, & \text{(broad spectrum)} \end{cases} \tag{3.19}$$

where $\mathcal{S}_{\nu,p}$ is the peak flux density (Eq. 3.6) and d_L is the luminosity distance. The isotropic peak luminosities of known FRBs vary from $\sim 10^{38}$ erg s^{-1} to a few 10^{46} erg s^{-1} [27, 137].

From Equation 3.19 we can obtain the isotropic energy of the FRB burst

$$E \simeq \frac{4\pi d_L^2}{1+z} \mathcal{F}_\nu \begin{cases} \Delta\nu, & \text{(narrow spectrum)} \\ \nu_c, & \text{(broad spectrum)} \end{cases} \tag{3.20}$$

where $\mathcal{F}_\nu$ is the specific fluence (Eq. 3.13). The isotropic energies vary from a few 10^{35} erg to a few 10^{43} erg.

In Figure 3.6, the authors [12] compare the burst to the fluence of the brightest radio pulse observed from a galactic magnetar (Galactic magnetar soft gamma repeater (SGR) $1935+21$ (31, 32)) with a wider sample of FRBs. They obtained that the burst energy integrated over the instrument bandwidth of FRB 220610A is $\sim 2 \times 10^{42}$ erg, which is higher than most localized FRBs and is a factor of 10^5 more luminous than the burst observed from a galactic magnetar.

The luminosity of FRBs is extremely high by the radio pulsar standard, but is very small when we consider the GRB standard. In the case of the energy, the true energetics of FRBs should be reduced by a beaming factor $f_b = max(\Delta\Omega/4\pi, 1/4\gamma^2) \leq 1$, $\Delta\Omega$ is the solid angle of the geometric beam, and γ is the Lorentz factor of the FRB emitter ($1/\gamma$ is the half kinetic beaming angle for an FRB emitter traveling close to speed of light). For a one-off FRB, a successful FRB engine should at least generate a luminosity and an energy of the order of $f_b L_p$ and $f_b E$, respectively [11].

The high luminosity and short variability timescale of the FRBs leads to an extremely high brightness temperature T_b, which can be obtained from the observed specific intensity [208]:

$$I_\nu(\nu) = \frac{\mathcal{S}_\nu}{\Delta\Omega}, \tag{3.21}$$

where $\mathcal{S}_\nu$ is the observed specific flux and the solid angle of the source viewed at the observer frame is $\Delta\Omega = \pi(c\Delta t_0)^2/d_A^2$, being $\Delta t_0 = \Delta t/(1+z)$ the rest-frame duration of the burst and d_A is the angular diameter distance from the observer to the source.

Now let us consider a blackbody emitter with temperature $T_b(\nu_0)$ with source frequency ν_0 at the rest frame frequency defined as $\nu_0 = (1+z)\nu$. The intensity at

the Rayleigh-Jeans regime is defined as [56]

$$I_\nu(\nu_0) = 2k_B T_b(\nu_0)\frac{\nu_0^2}{c^2}, \tag{3.22}$$

being k_B Boltzmann constant.

Noticing that $I_\nu(\nu_0) = I_\nu(\nu)(1+z)^3$, we can combine Equations 3.21 and 3.22 and obtain the expression for the brightness temperature at the source frequency

$$T_\nu(\nu_0) = \frac{\mathcal{S}_\nu d_A^2 (1+z)^3}{2\pi k_B (\nu \Delta t)^2}. \tag{3.23}$$

The typical value of the brightness temperature for a FRB is $T_b \sim 10^{36}$ K, being greater than any temperature allowed for incoherent radiation and for this reason, the radiation mechanism of FRBs must be coherent, as we discussed in Section 2.2.

Before the discovery of FRBs, radio pulsars have been the only known sources of producing extremely high T_b (typically $\sim (10^{25} - 10^{30})$ K). FRBs further push the limit of the degree of coherent radiation in the Universe [207].

3.4 Summary

In this chapter, we discussed the observational features of FRBs. We introduced basic concepts of radiation in the scenario of astronomy, defining some quantities that can be measured from observations of FRBs, e.g. brightness and flux density. After that, we briefly explained observational techniques to search for and discover FRBs, including some examples of radio telescopes that detect such events.

We also presented a population study, in which we discussed properties obtained directly from observations, like spectral shape and repeating or not. Such properties are very important to help us understand the progenitor of the bursts and improve the future searches for FRBs. For instance, from the brightness temperature of FRBs ($T_b \sim 10^{36}$ k), we know that the radiation emission must be coherent, which gives us some clues about their progenitor. Another important topic discussed is the host galaxy of the bursts, because one can help to understand the environment of these events, and also plays an important role in the use of FRBs in cosmology. Therefore, we presented the main features of FRBs.

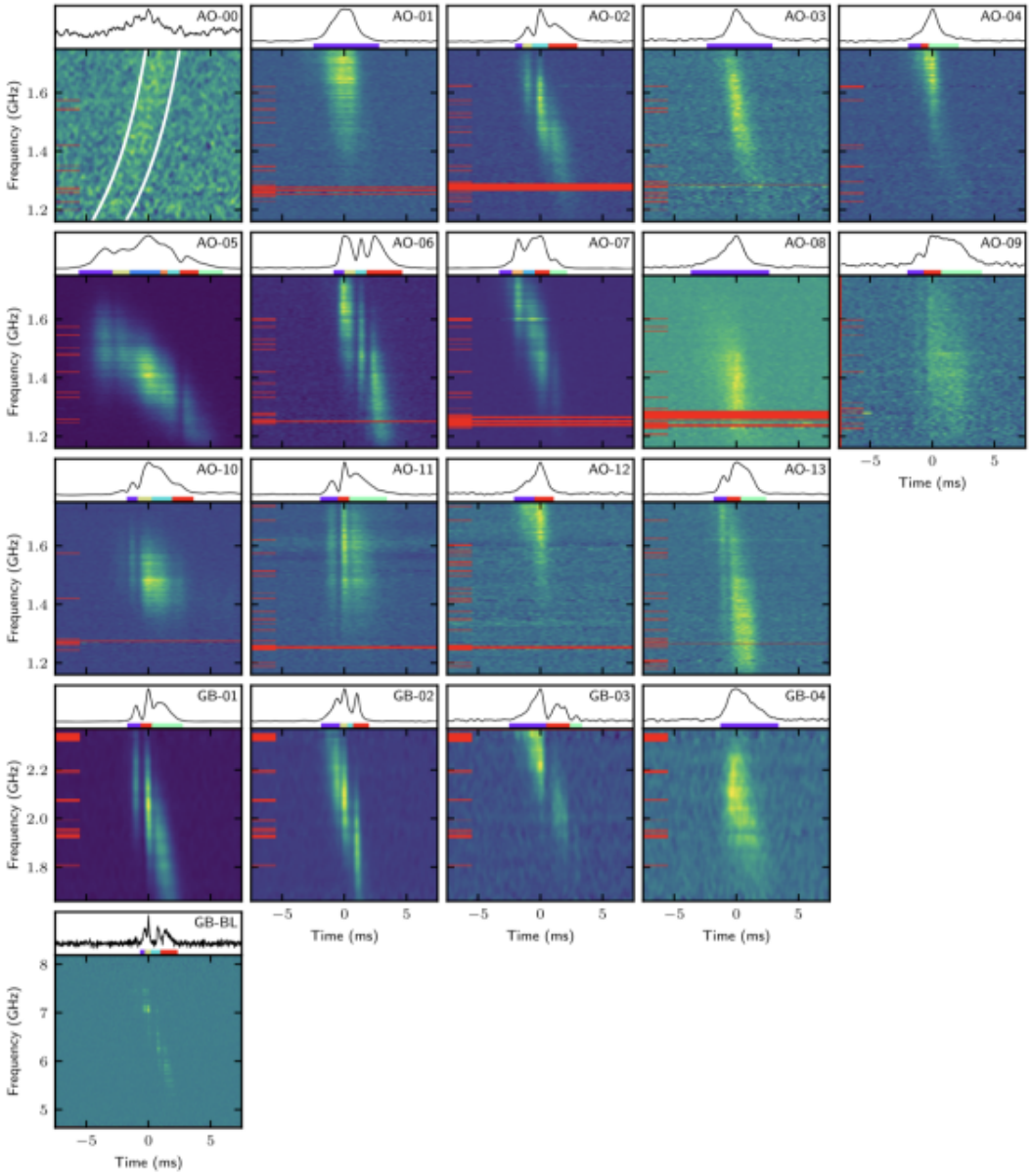

Figure 3.3: The dynamic spectra of individual bursts from the repeater FRB 121102A that show down-drifting of pulses with frequency. **Credit:** [7]

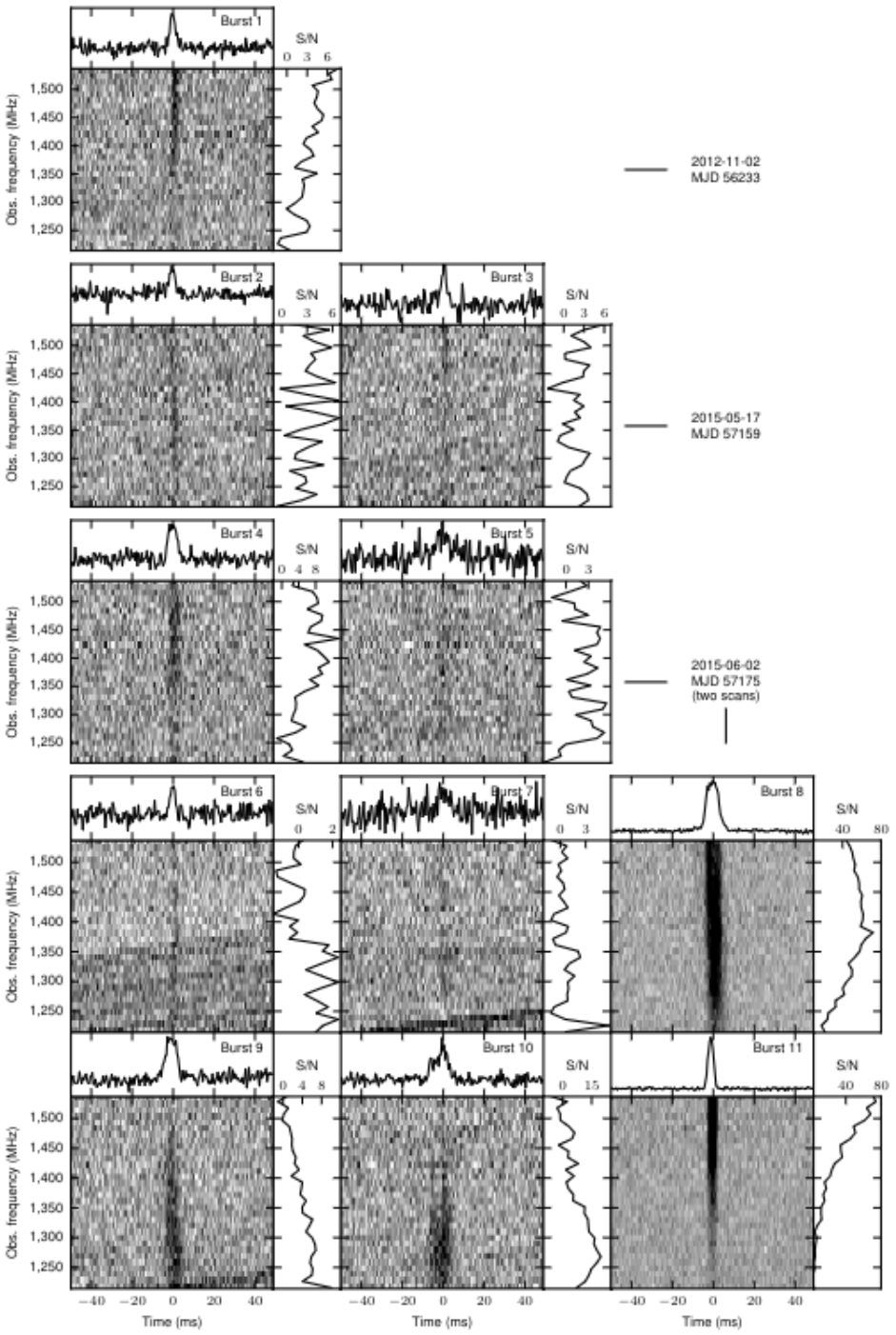

Figure 3.4: The morphologies and spectra of 11 bursts of FRB 121102. The central greyscale (linearly scaled) panels show the total intensity versus observing frequency and time. The upper sub-panels are burst profiles summed over all frequencies. The band-corrected burst spectra are shown in the right sub-panels. The signal-to-noise scales for the spectra are shown on each sub-panel. **Credit:** [8]

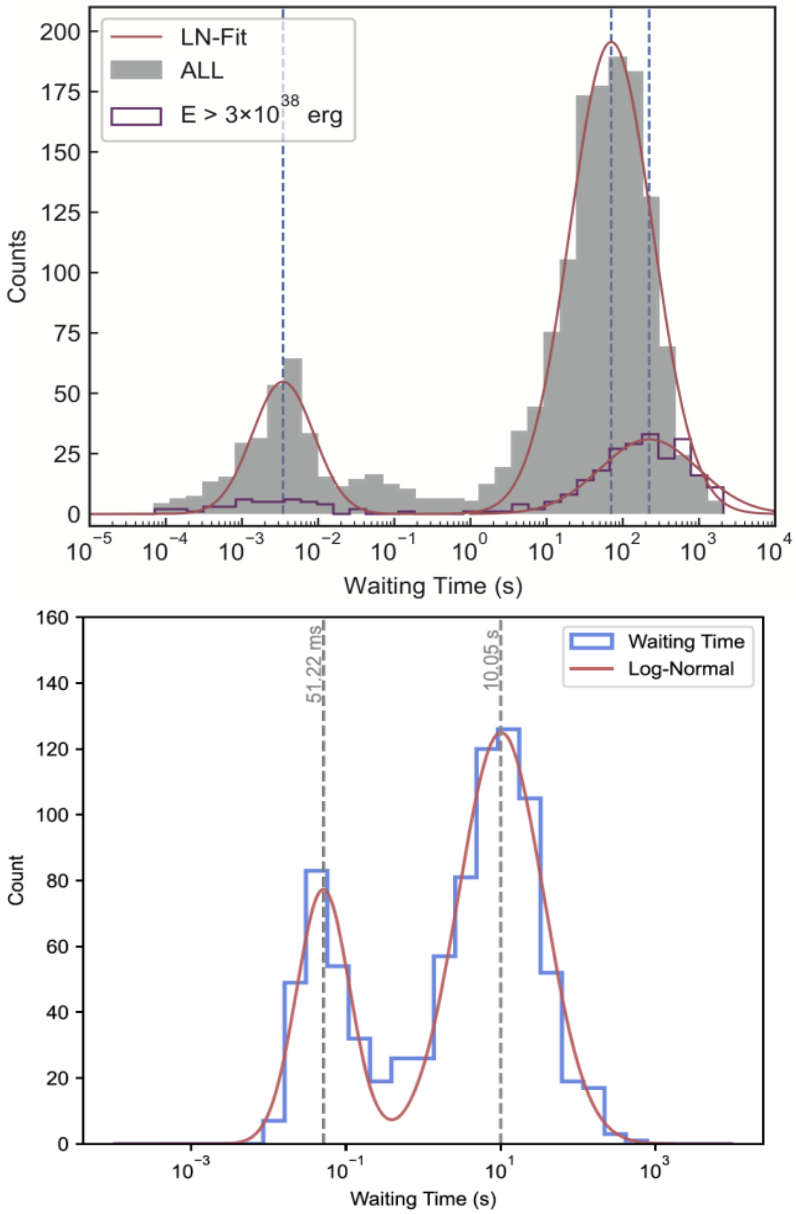

Figure 3.5: *Upper:* The grey bar and solid red curve denote the distribution of waiting time and its log-normal (LN) fit of FRB 121102A [9]. The high energy component ($E > 3 \times 10^{38}$ erg) is shown as the solid purple line. The two peaks are at a few milliseconds and ~ 100 s, respectively. *Bottom:* The blue step and red line show the distribution of waiting time and two log-normal fitting of FRB 201124A [10]. The second peak is at ~ 1 s, suggesting a very active episode. **Credit:**[11]

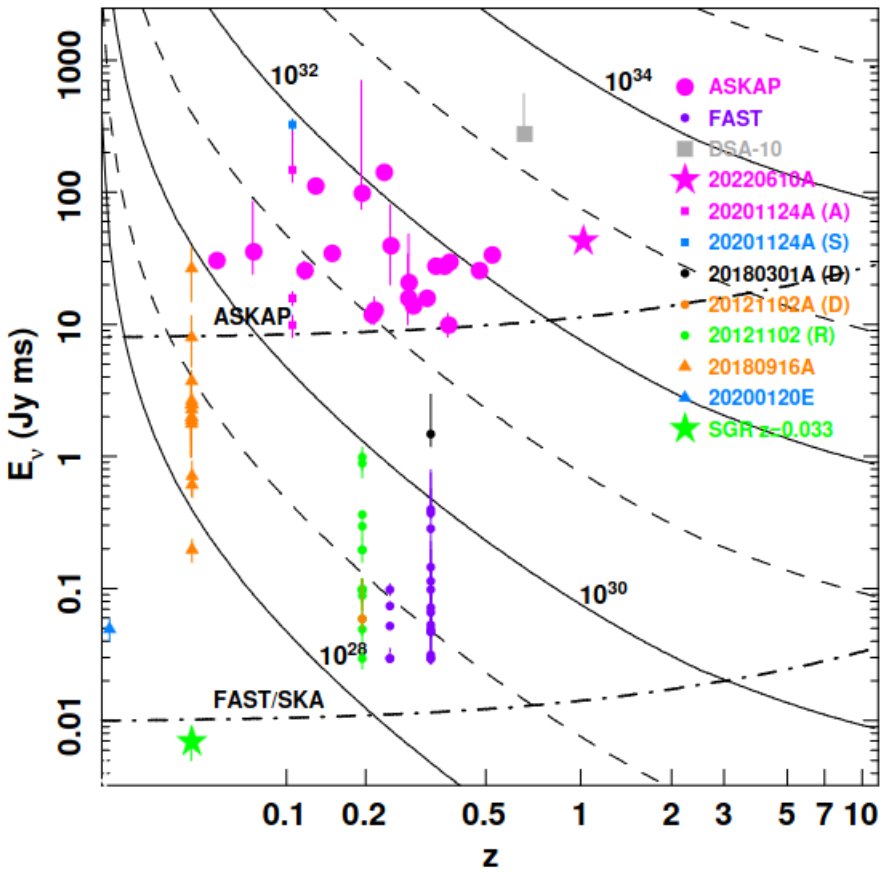

Figure 3.6: Logarithmic plot of fluence as a function of redshift for localized FRBs. The magenta star is FRB 20220610A. The green star shows the expected fluence of the FRB-like burst from Galactic magnetar soft gamma repeater (SGR) $1935 + 21$ $(31, 32)$. The curved solid and dashed contours indicate the energy density in units of erg Hz^{-1}. The dash-dotted lines show the detection sensitivity of the current ASKAP incoherent sum FRB search system, and the Five-hundred-meter Aperture Spherical Telescope and Square Kilometre Array telescopes (labeled FAST/SKA). **Credit:**[12]

PART II

FRB's applications in Cosmology

Chapter 4

Cosmological model-independent constraints on the baryon fraction in the IGM from fast radio bursts and supernovae data

This chapter presents the analysis reported in [209], in which we constrain the baryon fraction in the IGM combining well-localized FRBs with SNe observations.

4.1 Introduction

In Subsection 3.3.4, we commented on the importance of the host galaxy of FRBs and how is difficult to identify it. However, when it is possible to identify the host galaxy of the event, the redshift can be measured directly. Combining z with DM, we can use the DM $- z$ relation of these events as a tool to study the underlying cosmology. For instance, it is possible to constrain cosmological parameters [32, 33], such as the Hubble parameter $H(z)$ [34] and Hubble constant H_0 [35, 36], to probe the anisotropic distribution of baryon matter in Universe [31], as well as to constrain the fraction of baryon mass in the intergalactic medium (IGM) [37–39].

However, the uncertainties on the evolution of the fraction of baryon mass in the IGM ($f_{\rm IGM}$) and its degeneracy with the cosmological parameters restrict the application of FRBs in cosmology. The $f_{\rm IGM}$ represents the fraction of cosmic baryons that reside in IGM in relation to the total of baryons in the Universe. Since it is difficult to measure with most cosmological observations, $f_{\rm IGM}$ still is not well constrained. In this concern, some studies have been performed to discuss the baryon distribution in the IGM using both numerical simulations [45–47] and observations [48–50]. The authors in Reference [47] performed numerical simulations and found

that about 90% of the baryons produced by the Big Bang are contained within the IGM at $z \geq 1.5$ (i.e., $f_{\rm IGM} \approx 0.9$) whereas in Reference [49], the authors showed that the baryons existent in the collapsed phase at $z \geq 0.4$ represent $18 \pm 4\%$ or, equivalently, $f_{\rm IGM} \approx 0.82$. From these results, one may naively infer that the $f_{\rm IGM}$ grows with redshift.

Here we propose a new cosmological model-independent method to constrain a possible evolution of $f_{\rm IGM}(z)$ directly from observations of FRBs dispersion measure DM(z) and d_L from type Ia supernovae (SNe) data. In our analysis, we use 16 FRBs with known redshifts [137, 158, 183, 186, 190, 191, 196, 197, 199, 201, 202] along with the Pantheon SNe catalog [210]. We consider both constant and time-dependent parameterizations for $f_{\rm IGM}$ and discuss their observational viability through a Bayesian model selection analysis. We organized as follows. In Section 4.2 we introduce our method to study the evolution of $f_{\rm IGM}$ with redshift. The data sets used in the analysis and their application are presented in Section 4.3. Our main results are displayed in Section 4.4. The role of the DM fluctuations in the determination of the $f_{\rm IGM}$ evolution is discussed in Section 4.5.

4.2 A new method to determine the baryon fraction

As we mentioned earlier, one issue involving the application of FRBs in cosmology is related to the fact that the evolution of $f_{\rm IGM}$ with redshift is still not well understood. In order to investigate this matter further, we assume in our analysis two parameterizations for the baryon fraction, in which one is constant with z and another one is time-dependent, respectively:

$$f_{\rm IGM}(z) = f_{\rm IGM,0}, \tag{4.1}$$

$$f_{\rm IGM}(z) = f_{\rm IGM,0} + \alpha \frac{z}{1+z}. \tag{4.2}$$

In Equations 4.1 and 4.2, the parameter $f_{\rm IGM,0}$ is the present value of $f_{\rm IGM}$ whereas the constant α [1] quantifies a possible evolution of $f_{\rm IGM}$. In our analysis, both are free parameters and since $f_{\rm IGM}$ is understood to be an increasing function of the redshift, α assumes only positive values ($\alpha \geq 0$).

From equations that we presented in Section 2.1.1, one can constrain a possible evolution of the baryon fraction by modeling both $\rm DM_{host,0}$ and $\rm DM_{IGM}$ and comparing the theoretical predictions with the observed values of $\rm DM_{ext}$. To do that, the Equation 2.19 can be rewrite considering $\chi(z) = 7/8$

[1] Here α represents the parameter of $f_{IGM}(z)$ model, while in Chapter 6 α denotes the fine-structure constant.

$$\mathrm{DM_{IGM}}(z) = A \int_0^z f_{\mathrm{IGM}}(z') \frac{(1+z')}{H(z')} dz', \tag{4.3}$$

where $A = \frac{21 c \Omega_b H_0^2}{64 \pi G m_p}$.

Now we can calculate the above equation by parts using the above parameterizations.

4.2.1 Constant case

In this subsection, we will consider the constant parametrization for f_{IGM} (Eq. 4.1). Replacing Eq. 4.1, we can solve integral in Equation 4.3 using integration by parts, i.e.,

$$u = 1 + z' \longrightarrow du = dz',$$
$$dv = \frac{dz'}{H(z')} \longrightarrow v = \frac{d_L(z)}{(1+z)c},$$

where in the equation above we used the definition of luminosity distance [211]

$$d_L(z) = (1+z)c \int_0^z \frac{dz'}{H(z')}.$$

Equation 4.3 becomes

$$\mathrm{DM_{IGM}}(z) = A f_{\mathrm{IGM},0} \left[\frac{d_L(z)}{c} - \int_0^z \frac{d_L(z')}{(1+z')c} dz' \right]. \tag{4.4}$$

In order to calculate the 2nd term of the above equation using the current samples of SNe Ia to estimate $d_L(z)$, we numerically solved as [212]:

$$\int_0^z \frac{d_L(z')}{(1+z')c} dz' = \frac{1}{2c} \sum_{i=1}^{N} (z_{i+1} - z_i) \left[\frac{d_L(z_{i+1})}{(1+z_{i+1})} + \frac{d_L(z_i)}{(1+z_i)} \right], \tag{4.5}$$

using a simple trapezoidal rule. Since the error on z measurements is negligible, we only take into account the uncertainty on the values of $d_L(z)$. The error associated to the i^{th} bin is given by

$$\sigma_S^2 = \frac{1}{2c} \sum_{i}^{N} (z_{i+1} - z_i) \left[\frac{\sigma^2_{d_L(1+z_{i+1})}}{(1+z_{i+1})^2} + \frac{\sigma^2_{d_L(1+z_i)}}{(1+z_i)^2} \right]^{1/2}. \tag{4.6}$$

4.2.2 Time-dependent case

Now we will consider the time-dependent parameterization for the baryon fraction (Eq. 4.2). However, we will first assume a general case in which $f_{\mathrm{IGM}}(z)$ is dependent on z and solve the integral in the Equation 4.3 using integration by parts

$$u = (1+z')f_{\rm IGM}(z') \longrightarrow du = \left(f_{\rm IGM}(z') + (1+z')f'_{\rm IGM}(z')\right)dz',$$
$$dv = \frac{dz'}{H(z')} \longrightarrow v = \frac{d_L(z)}{(1+z)c},$$

where in the equation above we used the definition of luminosity distance and $df_{\rm IGM}/dz = f'_{\rm IGM}$. Then, the Equation 4.3 becomes

$$\mathrm{DM_{IGM}}(z) = A\left[f_{\rm IGM}(z)\frac{d_L(z)}{c} - \int_0^z \frac{d_L(z')}{(1+z')c} f_{\rm IGM}(z')dz' - \int_0^z \frac{d_L(z')}{c} f'_{\rm IGM}(z')dz'\right]. \tag{4.7}$$

Since the above equation is for a general case, now let us assume the parameterization $f_{\rm IGM}(z) = f_{\rm IGM,0} + \alpha\frac{z}{1+z}$

$$\mathrm{DM_{IGM}}(z) = A\Bigg[\left(f_{\rm IGM,0} + \alpha\frac{z}{1+z}\right)\frac{d_L(z)}{c} - \int_0^z \frac{d_L(z')}{(1+z')c}\left(f_{\rm IGM,0} + \alpha\frac{z'}{1+z'}\right)dz' - \int_0^z \frac{d_L(z')}{c}\frac{d}{dz'}\left(f_{\rm IGM,0} + \alpha\frac{z'}{1+z'}\right)\Bigg]dz', \tag{4.8}$$

where

$$\frac{d}{dz'}\left(f_{\rm IGM,0} + \alpha\frac{z'}{1+z'}\right) = \frac{\alpha}{(1+z')^2}. \tag{4.9}$$

Remembering that the parameters $f_{\rm IGM,0}$ and α are constant quantities in relation to redshift and considering the above relation, the equation 4.8 can be written as:

$$\mathrm{DM_{IGM}}(z) = A\left[\left(f_{\rm IGM,0} + \alpha\frac{z}{1+z}\right)\frac{d_L(z)}{c} - (f_{\rm IGM,0} + \alpha)\int_0^z \frac{d_L(z')}{(1+z')c}dz'\right], \tag{4.10}$$

where the last term and its uncertainty can solved using equations 4.5 and 4.6. Note that if we assume $\alpha = 0$ in the above expression, we return to constant case (Eq. 4.4).

Since we have new expressions for $\mathrm{DM_{IGM}}$ independent of cosmological parameters (Equations 4.3 and 4.10), it is possible to constrain the evolution of $f_{\rm IGM}(z)$ with redshift cosmological model-independent combining FRBs and SNe Ia dataset.

4.3 Data and methodology

In order to discuss a possible evolution of the baryon fraction, we use obser-

Name	Redshift z	$DM_{MW,ISM}$ [pc/cm^3]	DM_{obs} [pc/cm^3]	σ_{obs} [pc/cm^3]	Reference
FRB 180916B	0.0337	200.0	348.8	0.2	[197]
FRB 201124A	0.098	123.2	413.52	0.5	[186]
FRB 190608B	0.1178	37.2	338.7	0.5	[201]
FRB 200430A	0.16	27.0	380.25	0.4	[190]
FRB 121102A	0.19273	188.0	557.0	2.0	[183]
FRB 191001A	0.234	44.7	506.92	0.04	[190]
FRB 190714A	0.2365	38.0	504.13	2.0	[190]
FRB 191228A	0.2432	33.0	297.5	0.05	[196]
FRB 190102C	0.291	57.3	363.6	0.3	[191]
FRB 180924B	0.3214	40.5	361.42	0.06	[158]
FRB 180301A	0.3305	152.0	536.0	8.0	[196]
FRB 200906A	0.3688	36.0	577.8	0.02	[196]
FRB 190611B	0.378	57.83	321.4	0.2	[190]
FRB 181112A	0.4755	102.0	589.27	0.03	[199]
FRB 190711A	0.522	56.4	593.1	0.4	[190]
FRB 190523A	0.66	37.0	760.8	0.6	[137, 190]

Table 4.1: Properties of 16 well-localized FRB

vational data for the dispersion measures and luminosity distance. The former is obtained directly from FRBs measurements whereas the latter comes from SNe observations.

4.3.1 Data

FRBs

As was mentioned earlier, the current sample of FRBs contains 39 well-localized events (see Table 3.1). However, at the time of writing this work only 19 FRBs events with localized host galaxy and redshifts have been observed. Our subsample excludes the following bursts: the repeating burst FRB 20200120E [203] at $z = -0.0001$, observed in the direction of M81; the FRB 20181030A [198] since there is no SNe in the Pantheon catalog near its redshift ($z = 0.0039$); and, finally, the FRB 190614D whose redshift estimate lies in the interval $0.4 \lesssim z \lesssim 0.75$ (68% confidence interval), because can be associated with two host galaxies [202]. Our remaining sample contains 16 FRBs within the redshift interval $0.0337 \leq z \leq 0.66$ [137, 158, 183, 186, 190, 191, 196, 197, 199, 201], that are shown in Table 4.1, namely: redshift, $DM_{MW,ISM}$, DM_{obs} and observed DM error of all localized FRBs. The values of $DM_{MW,ISM}$ are estimated from the NE2001 model [59].

From Table 4.1, we can calculate our observational quantity, DM_{ext}, using Eq.

2.15, whose uncertainty is given by

$$\sigma^2_{\rm ext} = \sigma^2_{\rm obs} + \sigma^2_{\rm MW}, \tag{4.11}$$

where the average galactic uncertainty $\sigma_{\rm MW}$ is assumed to be 10 pc/cm^3 [213].

SNe Ia

For the current SNe data set, we used the largest combined sample of supernovae type Ia having a total of 1048 events ranging in the redshift range $0.01 < z < 2.3$ and named as "Pantheon Sample" [210]. It is possible to estimate $d_L(z)$ from current SNe Ia observations, using the definition of the distance moduli ($\mu(z)$) that is related to $d_L(z)$ by relation [211]

$$\mu(z) = m_B - M_B = 5\log_{10}\left[\frac{d_L(z)}{1{\rm Mpc}}\right] + 25\ , \tag{4.12}$$

where m_B is the apparent magnitude of SNe and M_B is the the absolute peak magnitude. As long as Type Ia supernovae are standardizable candles, after calibration the absolute peak magnitude can be considered equal for all redshifts. For this reason, in our analysis, we fix the absolute peak magnitude at $M_B = -19.214 \pm 0.037$ mag, as given by [214].

We perform a Gaussian Process (GP) reconstruction of the Pantheon data to obtain estimates of $d_L(z)$ at the same redshifts of the FRBs (for more details about GP see Appendix A) [2].

4.3.2 Methodology

Here, we will summarize the steps of our analysis to constrain the free parameters. In the first moment, we calculate ${\rm DM_{ext}}(z_i)$ observed and $\sigma_{\rm ext}$ (z_i) given by Equations 2.15 and 4.11), respectively, using the FRBs dataset in Table 4.1. Second, the luminosity distance is calculated from Equation 4.12 at the same ${\rm DM_{ext}}(z_i)$ redshift (z_i), using the GP reconstruction of Pantheon catalog. The integral given by Eq. 4.5 is then calculated with the SNe data, considering that the redshift limit of the sum (z_L) must be equal to the redshift of the FRB ($z_L = z_i$). Finally, we use the Monte Carlo Markov Chain (MCMC) method to fit the free parameters of our analysis, i.e., $f_{\rm IGM}$ and ${\rm DM_{host,0}}$ in the constant case (Eq. 4.4) and $f_{\rm IGM,0}$, α and ${\rm DM_{host,0}}$ for the time-dependent parameterization (Eq. 4.10).

[2] An alternative approach is to define a redshift interval centered at the redshifts of each FRB and calculate the average values of $d_L(z)$ from the SNe data within the interval. We verified this approach and obtained results (not shown here) very similar to the ones derived through the GP reconstruction.

The MCMC analysis is performed with the emcee sample [215]. Following Reference [216], in which the author use simulations to show that the probability distribution of DM can be close to Gaussian, we assume Gaussian individual likelihoods to observe a dispersion measure $\mathrm{DM}_{\mathrm{ext},i}$ at a given redshift z_i,

$$\mathcal{L}(\mathrm{DM}_{\mathrm{ext},i}, z_i) = \frac{1}{\sqrt{2\pi\sigma_i^2}} \exp\left[\frac{\left(\mathrm{DM}_{\mathrm{ext},i} - \mathrm{DM}_{\mathrm{ext}}^{\mathrm{th}}(z_i)\right)^2}{2\sigma_i^2}\right], \tag{4.13}$$

where $\mathrm{DM}_{\mathrm{ext}}^{\mathrm{th}}(z_i)$ is given by Eq. 2.16 and the component σ_i is the uncertainty for the DM measurement of each FRB given by Equation 4.11.

Since we are interested in a cosmological model-independent approach and to be consistent with our choice of M_B in Eq. 4.12, we adopt the value of the Hubble constant from the SH0ES collaboration, $H_0 = 74.03 \pm 1.4$ kms^{-1}Mpc^{-1} [214]. We also assume the baryon density parameter, $\Omega_b h^2 = 0.02235 \pm 0.00037$, from Big Bang Nucleosynthesis (BBN) analysis reported by [217].

4.4 Results

In Figure 4.1, we show the posterior probability density function and $1-2\sigma$ constraint contours of the free parameters ($f_{\mathrm{IGM},0}$, α, $\mathrm{DM}_{\mathrm{host},0}$) for the constant case (left Panel) and the time-dependent parameterization (right Panel). We also present in Table 4.2 the results for the baryon fraction for both cases. For the constant case, we obtain $f_{\mathrm{IGM},0} = 0.764 \pm 0.013$ and the estimate for the host galaxy contribution $\mathrm{DM}_{\mathrm{host},0} = 158.1 \pm 5.4$ pc/cm^3, both at 1σ level. In this case, the result for the baryon fraction is in good agreement with previous results obtained from observations [48–50, 218] and numerical simulations [36, 45, 46]. For the time-dependent case, we obtain $f_{\mathrm{IGM},0} = 0.483 \pm 0.066$ (1σ) for the present value of the baryon fraction and $\alpha = 1.21 \pm 0.28$ (1σ). We also estimate the host galaxy contribution at $\mathrm{DM}_{\mathrm{host},0} = 190.1 \pm 9.1$ pc/cm^3 (1σ). On the other hand, in this case, we note that the values of $f_{\mathrm{IGM},0}$ and α do not show agreement with other recent studies that used the same parameterization (4.2) – see e.g. [38, 219]. We believe that such discrepancy may be primarily related to the fact that these works do not consider the contribution of the host galaxy $\mathrm{DM}_{\mathrm{host}}$ as a free parameter in their analyses, as well as to the more up-to-date FRB data used in our analysis.

	$f_{\mathrm{IGM},0}$	α	$\mathrm{DM}_{\mathrm{host},0}$ [pc/cm^3]
Constant	0.764 ± 0.013	-	158.1 ± 5.4
Time-dependent	0.483 ± 0.066	1.21 ± 0.28	190.1 ± 9.1

Table 4.2: Estimates of the parameters $f_{\mathrm{IGM},0}$, α and $\mathrm{DM}_{\mathrm{host},0}$ for the two parameterizations considered in the analysis.

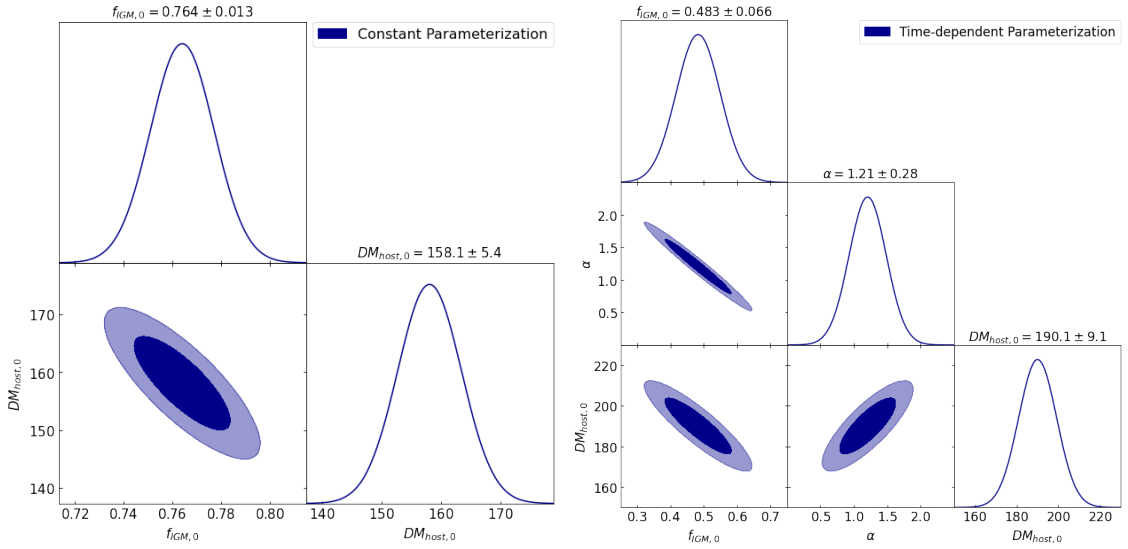

Figure 4.1: *Left:* Constraints on the baryon fraction $f_{\rm IGM}$ and the mean host galaxy contribution of dispersion measure $\rm DM_{host,0}$ considering the constant case (4.4). *Right:* Constraints on the present-day baryon fraction $f_{\rm IGM,0}$, α and the mean host galaxy contribution of dispersion measure $\rm DM_{host,0}$ for the time-dependent parameterization (4.10).

Another important aspect of the above results concerns the observational evidence for an evolution of the baryon fraction $f_{\rm IGM}$ with redshift. In order to evaluate the two parameterization cases studied in this work and quantify such evidence, we perform a Bayesian model comparison. This kind of analysis offers a way to assess if the extra complexity of a given model or parameterization (here represented by the parameter α) is required by the data, preferring the model that describes the data well over a large fraction of their prior volume (for more details about Bayes analyses see Appendix B).

By defining the evidence as the marginal likelihood of the models, we calculate the Bayes' factor B_{ij}:

$$B_{ij} = \frac{\mathcal{E}_i}{\mathcal{E}_j} \,, \tag{4.14}$$

where $\mathcal{E}_i$ and $\mathcal{E}_j$ correspond to the evidence of parameterizations $\mathcal{P}_i$ and $\mathcal{P}_j$, respectively. We adopted the Jeffreys' scale [220] to interpret the values of $\ln B_{ij}$ for the reference parameterization $\mathcal{P}_j$: $\ln B_{ij} = 0 - 1$, $\ln B_{ij} = 1 - 2.5$, $\ln B_{ij} = 2.5 - 5$, and $\ln B_{ij} > 5$ indicate, respectively, an inconclusive, weak, moderate and strong preference of the parameterization $\mathcal{P}_i$ with respect to $\mathcal{P}_j$. Negative values of $\ln B_{ij}$ mean preference in favour of $\mathcal{P}_j$.

We use the MultiNest algorithm [221–223] to compute the Bayesian evidence ($\ln \mathcal{E}$) and then calculate the Bayes' factor. Adopting the constant case (4.1) as

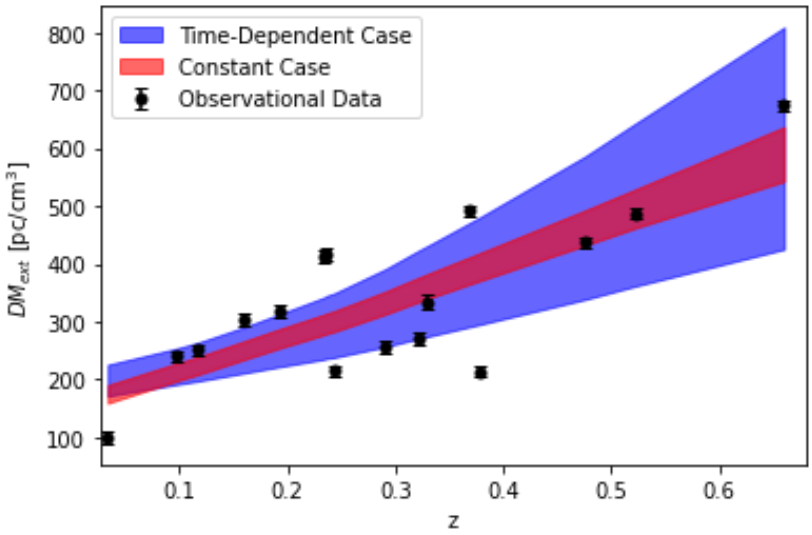

Figure 4.2: The 3σ envelope for the evolution of $\mathrm{DM_{ext}}$ with redshift considering the constant (red) and time-dependent (blue) parameterizations.

reference, we obtain $\ln \mathcal{E}_j = -565.349$ and $\ln \mathcal{E}_i = -557.032$ for the reference and time-dependent cases, respectively, which results in $\ln B_{ij} = 8.32$. Such a result indicates a strong evidence in favor of the time-dependent parameterization (4.2) with respect to the constant case (4.1), with the interval of values of the parameters $f_{\mathrm{IGM},0}$, α and $\mathrm{DM_{host,0}}$ given by Table 4.2. For completeness, we also show in Figure 4.2 the 3σ envelope for the evolution of $\mathrm{DM_{ext}}$ with redshift (eq. 2.16) considering both parameterizations. We note that the analysis above clearly shows the potential of the method proposed here to probe a possible evolution f_{IGM} with redshift.

4.5 Dispersion measure fluctuations

The spatial distribution of baryons in the IGM, including those ejected from galactic halos through feedback processes, plays a very important role in the $\mathrm{DM}-z$ relation. The variance of the large-scale structures leads to a large variance in the observed DM (see e.g. [42, 43] for a detailed discussion on the DM fluctuations). Such fluctuations are not currently well determined by observations and can be treated as a probability distribution or as fixed value in the statistical analyses [35, 41, 216].

In Reference [40], the authors show that the inhomogeneities effect in the baryon distribution leads to substantial scatter around the mean $\mathrm{DM}(z)$, whose standard deviation is $100 - 400$ pc/cm^3 at $z = 0.5 - 1$. Another work [216] found $\sim 13\%$ in

DM to a source at $z = 1$ and $\sim 7\%$ at $z = 3$ (for 1σ), where the DM distribution is closed to Gaussian. The authors in Reference [41] demonstrated that the variance can be approximated from relation $\delta = Fz^{-0.5}$ pc/cm^3, where F is the fluctuation parameter. While the authors [42] presented an analytical function for the variance of the DM ($\delta = 230\sqrt{z}$ pc/cm^3) obtained from simulations, which is consistent with predictions from References [40, 41].

In the previous sections, we presented and applied our method to constrain the $f_{\rm IGM}$ evolution without considering the DM fluctuations (δ). In order to assess the impact of these fluctuations in the results presented in section 4.4, we take into account this variance in our analyses assuming three different values for this quantity, $\delta = 10, 50, 100$ pc/cm^3, being the latter in agreement with the results reported in [42]. We perform our analysis by adding this additional term in quadrature to Equation 4.11

$$\sigma^2_{\rm ext} = \sigma^2_{\rm obs} + \sigma^2_{\rm MW} + \delta^2, \tag{4.15}$$

and then we follow the procedure described in section 4.3.

The results of our analysis are displayed in Figure 4.3 and Table 4.3. Figure 4.3 shows the posterior probability density function and 1-2σ contours on the parametric spaces for different values of the DM fluctuations. The quantitative results of the analysis, displayed in Table 4.3, show the impact of the DM fluctuations in the determination of the $f_{\rm IGM}$ evolution, as the evidence varies from moderate (in favor of a growing evolution of $f_{\rm IGM}$ with redshift) to inconclusive and inconclusive for $\delta = 10, 50, 100$ pc/cm^3, respectively. Therefore, differently from the results presented in the previous section ($\delta = 0$), these results show that a conclusive answer about the time-evolution of $f_{\rm IGM}$ depends strongly on the DM fluctuations and cannot be achieved from the current FRB observational data.

δ [pc/cm^3]	$f_{\rm IGM,0}$	α	DM$_{\rm host,0}$ [pc/cm^3]	$\ln \mathcal{E}_i$	$\ln B_{ij}$
10	0.76 ± 0.02	-	158.3 ± 7.5	- 286.458 ± 0.007	-
50	0.76 ± 0.07	-	158.3 ± 30.0	- 25.328 ± 0.005	-
100	0.76 ± 0.13	-	162.0 ± 50.0	- 7.917 ± 0.003	-
10	0.48 ± 0.09	1.21 ± 0.39	190.44 ± 12.70	- 282.452 ± 0.007	4.006 ± 0.007
50	0.43 ± 0.22	1.22 ± 0.39	197.22 ± 35.26	- 24.757 ± 0.004	0.571 ± 0.006
100	0.40 ± 0.26	1.56 ± 1.08	196.56 ± 53.62	- 7.670 ± 0.004	0.247 ± 0.005

Table 4.3: Estimates of the $f_{\rm IGM}$ parameters for different values of the DM fluctuations.

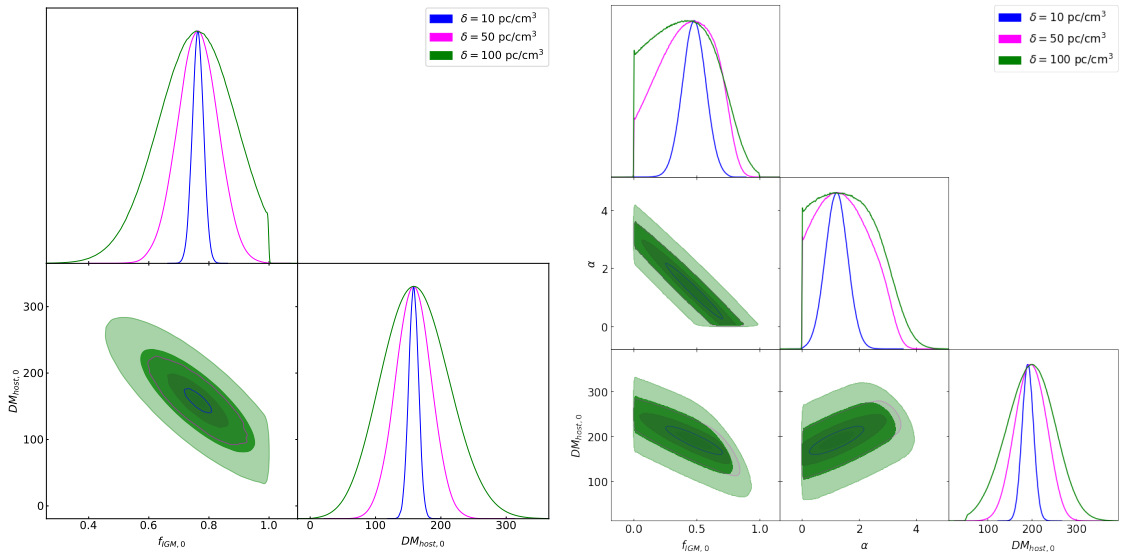

Figure 4.3: The same as in figure 4.1 considering fluctuations in the FRB's DM.

4.6 Summary

In this chapter we followed a semi-analytical method described, in which $\mathrm{DM_{IGM}}(z)$ is written in terms of $d_L(z)$, to investigate the current constraints on the baryon fraction. We considered two different behaviors for this quantity, the constant and time-dependent parameterizations. We used 16 FRB observations, the most up-to-date data currently available, and a GP reconstruction of 1048 SNe from the Pantheon catalog to perform a MCMC analysis considering the host galaxy contribution for the dispersion measure $\mathrm{DM_{host,0}}$ as a free parameter and no DM fluctuation ($\delta = 0$). For the constant case, we found $f_{\mathrm{IGM,0}} = 0.764 \pm 0.013$ and $\mathrm{DM_{host,0}} = 158.1 \pm 5.4$ pc/cm^3 (1σ) whereas for the time-dependent case we obtained $f_{\mathrm{IGM,0}} = 0.483 \pm 0.066$, $\alpha = 1.21 \pm 0.28$, and $\mathrm{DM_{host,0}} = 190.1 \pm 9.1$ pc/cm^3 at 1σ level. In order to evaluate the observational viability of the two cases considered in the analysis we also performed a Bayesian model comparison. Such results showed a strong evidence ($\ln B_{ij} = 8.32 \pm 0.01$ at 1σ) in favor of an increasing evolution of f_{IGM} with redshift.

On the other hand, when the DM fluctuations due to the spatial variation in cosmic electron density are considered in the analysis the results are much less conclusive. In this case, we considered three values of δ and showed that the strong evidence in favor of a growing evolution of f_{IGM} with redshift obtained in the case of $\delta = 0$ pc/cm^3 changes to moderate ($\delta = 10$ pc/cm^3) and inconclusive ($\delta = 50$ and 100 pc/cm^3). These results clearly show the impact of DM fluctuations in the determination of the f_{IGM} evolution. They also reinforce the interest in searching for a larger sample of FRBs and the need for a better understanding of their physical

properties.

As we mentioned in Subsection 3.3.4, it is expected that the new instruments, such as CHIME [52], CRACO [51] and SKA [53] will detect several thousands of FRBs in the next years. These observations will improve significantly the constraints on $f_{\rm IGM}$ from the method proposed here, bringing important information about the matter distribution in the Universe as well as demonstrating the potential of FRBs observations for precision measurements of cosmological parameters.

Chapter 5

Forecasting constraints on the baryon mass fraction in the IGM from fast radio bursts and type Ia supernovae

This chapter presents the analysis reported in [224], in which we forecast constraints on the baryon fraction using the method discussed in the previous chapter.

5.1 Introduction

As we see in previous chapters, FRBs can be used in both astrophysical and cosmological contexts. From the DM $-$ z relation, FRBs can be used to probe the anisotropic distribution of baryon matter in the Universe [31], to test the weak equivalence principle [30] or to constrain cosmological parameters [32, 33], such as the Hubble constant [34–36] and the baryon mass fraction in the intergalactic medium ($f_{\rm IGM}$) [37–39]. However, it is necessary to understand better some of their observational properties to explore the full potential of these objects. For instance, the host galaxy contribution of the FRBs ($\rm DM_{host}$) is not well constrained and depends on many factors such as the galaxy type, the relative orientation between the FRB source with respect to the host as well as the mass of the host galaxy [44]. Another limitation is the density fluctuations in the dispersion measure (DM) due to the spatial variation in cosmic electron distribution [42].

The $f_{\rm IGM}$ is another issue that restricts the application of FRBs in cosmology because this parameter is not well constrained and it is also degenerated with the cosmological parameter (see Eq. 2.19). In Reference [49], the authors found $f_{\rm IGM} \approx 0.82$ at $z \geq 0.4$, while in [47] the authors estimated $f_{\rm IGM} \approx 0.9$ at $z \geq 1.5$. These

results show a possible variation of $f_{\rm IGM}$ with respect to redshift. In this context, in a previous work [209], we used a cosmological model-independent method to constrain $f_{\rm IGM}$ (see Sec. 4.2), assuming both constant and time-dependent parameterizations, and found that the time-evolution of $f_{\rm IGM}$ depends strongly on the DM fluctuations due to the spatial variation in cosmic electron density.

Although more than one hundred FRBs have been detected, thanks to new telescopes since their first discovery by Parkes Telescope in 2007 [1], only a few FRBs in the literature are well localized, with the correspondent redshift (see Subsec. 3.3.4), being the current sample not large enough to perform robust statistical analysis. However, new instruments are being built to localize FRBs in the next few years. Such as the coherent upgrade CRACO system [51] of ASKAP, the CHIME outriggers [52], SKA1-Mid [53] and the BINGO Interferometry System (BIS) of Baryon Acoustic Oscillations (BAO) from Integrated Neutral Gas Observations (*BINGO*) radio telescope [55]. While BIS is expected to localize 23 FRBs per year, the number for ASKAP/CRACO and CHIME/FRB is $\sim$ 100 and $\sim$ 500 FRBs per year, respectively.

In this scenario, understanding the constraining power of the upcoming observations through numerical simulations is, therefore, an important and necessary task. Since the physical mechanism responsible for the FRB burst is still in debate, the redshift distribution of these events is unknown. For this reason, it is necessary to combine astrophysical assumptions with numerical simulations to obtain the redshift distribution models of these events. The literature has explored distributions based on general aspects, such as star formation history/rate [225] or by assuming a specific astrophysical origin, such as gamma-ray bursts [226]. For a general analysis of the possible distributions, we refer the reader to [227] and references therein.

In this context, we investigate the impact of different FRB redshift distribution models and the number of FRB events on the constraints of mass of baryon fraction in the IGM and host galaxy contribution through Monte Carlo simulations. We also consider the role of different values of DM fluctuations on the free parameters estimates. We calculate the $f_{\rm IGM}$ cosmological-model independent using the same method presented in our previous work [209] (see Sec. 4.2), but now FRBs data from Monte Carlo simulated data are combined with SNe Ia observations.

5.2 Analysis

In what follows, we describe the observational datasets used in this work and our methodology to estimate the $f_{\rm IGM,0}$ and $\rm DM_{host,0}$. Following [209] for the constant case, the observational data points are obtained by combining the $\rm DM - z$ relation with $d_L(z)$ estimates from SNe observations.

Name	Redshift z	$DM_{MW,ISM}$ [pc/cm^3]	DM_{obs} [pc/cm^3]	σ_{obs} [pc/cm^3]	Reference
FRB 180916B	0.0337	200.0	348.8	0.2	[197]
FRB 201124A	0.098	123.2	413.52	0.5	[186]
FRB 190608B	0.1178	37.2	338.7	0.5	[201]
FRB 200430A	0.16	27.0	380.25	0.4	[190]
FRB 121102A	0.19273	188.0	557.0	2.0	[183]
FRB 191001A	0.234	44.7	506.92	0.04	[190]
FRB 190714A	0.2365	38.0	504.13	2.0	[190]
FRB 191228A	0.2432	33.0	297.5	0.05	[196]
FRB 190102C	0.291	57.3	363.6	0.3	[191]
FRB 180924B	0.3214	40.5	361.42	0.06	[158]
FRB 200906A	0.3688	36.0	577.8	0.02	[196]
FRB 190611B	0.378	57.83	321.4	0.2	[190]
FRB 181112A	0.4755	102.0	589.27	0.03	[199]
FRB 190711A	0.522	56.4	593.1	0.4	[190]
FRB 190523A	0.66	37.0	760.8	0.6	[137, 190]

Table 5.1: A list of 15 FRB with known host galaxies.

5.2.1 Data

Although we listed in Table 3.1 the most up-to-date sample of well-localized FRBs with 39 events (see Subsection 3.3.4), at the time of performing this work, there were 20 well-localized FRBs events detected. In our analysis, we exclude the events FRB 20200120E, FRB 20191228, FRB 20190614D, FRB 20190520B and FRB 20181030A due to the following reasons: the host of FRB 20200120E [203] is near our Galaxy and a Milky Way halo origin cannot be rejected; FRB 20190614D [202] has no measurement of spectroscopic redshift and can, in principle, be associated with two host galaxies. FRB 20190520B [200] has a host contribution much larger than the other FRBs, whereas FRB 20191228 [196] has the uncertainty of observed dispersion measure much larger than the others ($\sigma_{obs} = 8$ pc/cm^3); and finally, there is no SNe in the Pantheon catalog with the redshift close to FRB 20181030A [198] ($z = 0.0039$).

Our remaining subsample contains 15 FRBs with well-measured redshift [137, 158, 183, 186, 190, 191, 197, 199, 201], and is listed in Table 5.1 with the observed dispersion measure (DM_{obs}), the Galaxy contribution ($DM_{MW,ISM}$) estimated from the NE2001 model [59], and the uncertainty of DM_{obs} (σ_{obs}).

The observational quantity DM_{ext} (Eq. 2.15) can be obtained using data from Table 5.1 with its uncertainty calculated by the expression given in Equation 4.15, where the average galactic uncertainty σ_{MW} is assumed to be 10 pc/cm^3 [213] and δ stands for the DM fluctuations discussed in Sec. 4.5. Such fluctuations are due to the spatial variation in cosmic electron density and can be treated as a probability distribution or as a fixed value in the statistical analyses [35, 41, 216]. In this work,

δ [pc/cm^3]	$f_{\rm IGM,0}$	DM$_{\rm host,0}$ [pc/cm^3]
0	0.77 ± 0.01	158.8 ± 5.3
100	0.76 ± 0.11	158.0 ± 50.0
200	0.74 ± 0.16	152.0 ± 65.0
400	0.66 ± 0.17	142.0 ± 70.0
$230\sqrt{z}$	0.81 ± 0.12	133.0 ± 30.0

Table 5.2: Estimates of the $f_{\rm IGM}$ and DM$_{\rm host,0}$ from current observational data.

we will consider three different values for $\delta = 0, 100, 200, 400, 230\sqrt{z}$ pc/cm^3, in agreement with recent results presented in the literature [42, 209].

In order to estimate the luminosity distance in Equation 4.4, we use the current SNe observations, Pantheon catalog [210] and convert the SNe distance modulus into luminosity distances using Equation 4.12. In our analysis, we adopt the absolute peak magnitude at $M_B = -19.214 \pm 0.037$ mag [214] or, equivalently, $H_0 = 74.03 \pm 1.4$ km Mpc^{-1}s^{-1}.

5.2.2 Methodology

In Reference [209] (which we detailed in the previous chapter) we presented a cosmological model-independent method to constrain $f_{\rm IGM}$ considering two parameterizations for it, for simplicity, here we consider only the constant case (Eq. 4.1). The steps of our analysis are followed: First, since we need to estimate $d_L(z)$ at the same redshift of the FRBs, we perform a GP reconstruction of the Pantheon data (see Appendix A); Second, we calculated $d_L(z)$ and the integral given by Equation 4.5 at the same redshift of FRBs; Finally, we estimate the two free parameters ($f_{\rm IGM,0}$, DM$_{\rm host,0}$) in Equation 4.4 performing a MCMC analysis using the *emcee* package [215], assuming a Gaussian distribution likelihood (Eq. 4.13). The results of our observational data analysis for $\delta = 0, 100, 200, 400, 230\sqrt{z}$ pc/cm^3 are displayed in Table 5.2.

5.3 Simulations

In order to study the cosmological impact of a larger sample of FRBs than the one currently available, we perform a Monte Carlo (MC) simulation to generate random points of DM$_{\rm ext}$. In general, there are 5 important steps to simulations, which we will describe below.

I) Redshift distribution

As we discussed in Section 2.3, many progenitor models have been proposed for FRBs, but it is unclear which one is responsible for these events. For this reason, the

distribution of these bursts is still uncertain. Since we need a redshift distribution of FRBs to generate the points for the MC simulation method, many distribution models of FRBs have been proposed in the literature. In Reference [227], the authors studied the effects of nine different redshift distributions of FRBs to constrain the density of matter in the Universe (Ω_m) and found that three of them present strong constraining power on Ω_m. For this reason, we will consider these three distributions, namely:

- *Gamma-Ray Bursts:* Several studies assume the gamma-ray bursts distribution for FRBs due to the similarity between these two events [228]. The density function is written as
$$P_{\rm GRB}(z) \propto z \exp(-z). \tag{5.1}$$

- *Star Formation Rate:* The star formation rate distribution was proposed by [229] (see also Reference [225] for the first proposal of redshift distribution for FRBs). The spatial distribution of FRBs is expected to closely trace the cosmic one for young stellar FRB progenitors. The cosmic SFR function can be written as
$$\psi(z) = 0.015 \frac{(1+z)^{2.7}}{1+[(1+z)/2.9]^{5.6}}. \tag{5.2}$$

- *Uniform:* The uniform distribution assumes that the FRBs distribution is constant and its density function is given by
$$P_{\rm Uniform} = \frac{1}{z_{max} - z_{min}}. \tag{5.3}$$

For completeness, we also consider an additional distribution, where the FRBs redshifts are picked at equidistant points (ED) between z_{min} and z_{max}. In Figure 5.1 we present the three redshift distribution models for FRBs.

Since for $z > 1.5$, the GP reconstruction of the Pantheon data overestimates the uncertainty values (given the small number of points in such interval), we generate random points using these distributions in the redshift range $0.022 \leq z \leq 1.5$ (Fig. 5.1). We consider samples with N = 15, 30, 100, and 500 points.

II) Fiducial points

To estimate the fiducial values of extragalactic contribution ($\rm DM_{ext}^{fid}$), we use Equation 2.16, being $\rm DM_{host}$ given by Equation 2.17 and $\rm DM_{IGM}$ by Eq. 2.19 considering flat-ΛCDM model, where the $H(z)$ is written as $H(z) = H_0\sqrt{\Omega_m(1+z)^3 + 1 - \Omega_m}$. We adopt the mean values of baryon fraction and host contribution as reported in [209] for the constant case, i.e., $f_{\rm IGM,0} = 0.764$ and $\rm DM_{host,0} = 158.1\ pc/cm^3$. In our simulations, we also adopt the values of

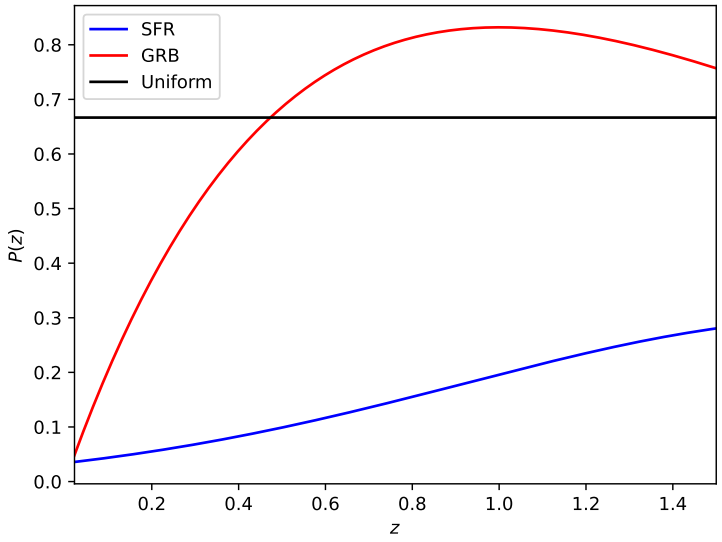

Figure 5.1: The normalized redshift distributions for FRBs.

$H_0 = 74.03 \pm 1.4$ km Mpc^{-1}s^{-1} [214], $\Omega_m = 0.3153$ [15] and $\Omega_b h^2 = 0.02235 \pm 0.00037$ [217].

III) Uncertainty of simulated data

The $\mathrm{DM_{IGM}}$ and $\mathrm{DM_{host,0}}$ are not well constrained, so we can not estimate the uncertainty of $\mathrm{DM_{ext}}$ simulated ($\sigma_{\mathrm{ext}}^{\mathrm{sim}}$) from these quantities. So we calculate $\sigma_{\mathrm{ext}}^{\mathrm{sim}}$ performing a regression of observational data of relative error ($\eta = \sigma_{\mathrm{ext}}^{\mathrm{obs}}/\mathrm{DM_{ext}^{obs}}$). As long as the relative error decreases with z and cannot be negative, we consider the relative error described by a hyperbolic function which is

$$\eta = \sigma_{\mathrm{ext}}^{\mathrm{obs}}/\mathrm{DM_{ext}^{obs}} = A/z, \tag{5.4}$$

where A hyperbolic regression free parameter.

IV) Standard deviation

Now to calculate the standard deviation (sd) that we will assume in the normal distribution, we consider a different approach. We adopt sd being the mean distance between the observed extragalactic quantity ($\mathrm{DM_{ext}^{obs}}$) and fiducial points generated ($\mathrm{DM_{ext}^{fid}}$)

$$sd = \sum \frac{|\mathrm{DM_{ext}^{obs}} - \mathrm{DM_{ext}^{fid}}|}{N}. \tag{5.5}$$

V) Simulated data

Finally, we calculate the simulated $\mathrm{DM_{ext}}$ by assuming a normal distribution, given by relation

$$\mathrm{DM_{ext}^{sim}}(z) = \mathcal{N}(\mathrm{DM_{ext}^{fid}}, sd), \tag{5.6}$$

where the mean is the fiducial value and sd is the standard deviation of the Gaussian Distribution.

We perform the steps above 50 times for each sample size of the distribution models, which is enough to obtain convergence. In each simulation, we calculate the free parameters while considering different values of DM fluctuations $\delta = 0, 100, 200, 400, 230\sqrt{z}$ pc/cm^3. Regarding the $\mathrm{DM_{host,0}}$, we assume in our MCMC analysis a Gaussian prior for this parameter, with the mean value and standard deviation being the best-fit values shown in Table 5.2. Subsequently, we calculate the average of each ensemble of 50 simulations. In Appendix C we show the figures with the best-fit results of our 50 realizations probing the convergence of our simulations.

5.4 Results

In Figures 5.2 and 5.3, we present the 1σ error bars for the free parameters $f_{\mathrm{IGM,0}}$ and $\mathrm{DM_{host,0}}$, considering different redshift distributions and values of fluctuations $\delta = 0, 100, 200, 400, 230\sqrt{z}$ pc/cm^3. Tables 5.3 and 5.4 are displayed the numerical values obtained separately for all distributions and different numbers of points in each realization ($N = 15, 30, 100, 500$).

For all distributions (except for the sample $N = 15$) the constraints on $f_{\mathrm{IGM,0}}$ and $\mathrm{DM_{host,0}}$ are compatible within 2σ. Comparing the results of simulations for $N = 15$ with the results for the current observational data (Table 5.2), which also comprises 15 points, we find that: (i) for $\delta = 0$ pc/cm^3, all distributions are not in agreement for $f_{\mathrm{IGM,0}}$ within 2σ; (ii) for $\mathrm{DM_{host,0}}$, differently from the SFR distribution, GRB, Uniform and ED distributions agree at 2σ; (iii) for the other values of the DM fluctuation, the results from the redshift distributions are in agreement within 1σ for both parameters $f_{\mathrm{IGM,0}}$ and $\mathrm{DM_{host,0}}$.

Finally, it is worth mentioning that the errors on the $f_{\mathrm{IGM,0}}$ and $\mathrm{DM_{host,0}}$ parameters depend on the number of points and the DM fluctuations. Our results show that such errors are smaller for a given value of the DM fluctuations as larger as the number of points considered. On the other hand, the errors increase for results with the same number of points N and higher values of δ. Therefore, these results show that larger data samples, as expected by the next generations of surveys, play a crucial role in this kind of analysis, along with a better understanding of the DM

fluctuations parameter.

5.5 Summary

In this chapter, we investigated the impact of the DM fluctuations and the number of FRBs observations to constrain the parameters $f_{\rm IGM,0}$ and $\rm DM_{host,0}$ from simulated data considering distinct probability distributions for the sources. We generated data sets from Monte Carlo simulations considering four redshift distributions, namely Gamma-ray Bursts, Star Formation Rate, Uniform, and Equidistant distributions. The number of points in the analyses varied from $N = 15, 30, 100, 500$, as expected from upcoming projects, whereas the DM fluctuations assumed values of $\delta = 0, 100, 200, 400, 230\sqrt{z}$ pc/cm^3.

Our results showed an agreement within 2σ between the GRB, SFR, Uniform, and ED distributions, regardless of the values of δ. In particular, our analysis highlighted the crucial role of DM fluctuations in the results, which reinforces the need for more investigations into this quantity. As an example, for $N = 100$, as expected by the ASKAP/CRACO per year [51], we found that the expected relative error for $f_{\rm IGM,0}$ varies from $\sim 0.2\%$ ($\delta = 0$ pc/cm^3) to 6% ($\delta = 400$ pc/cm^3) and from $\sim 2\%$ ($\delta = 0$ pc/cm^3) to 60% ($\delta = 400$ pc/cm^3) for $\rm DM_{host,0}$ (see Tables 5.3 and 5.4), which have improved compared with the observed relative error (see Table 5.2).

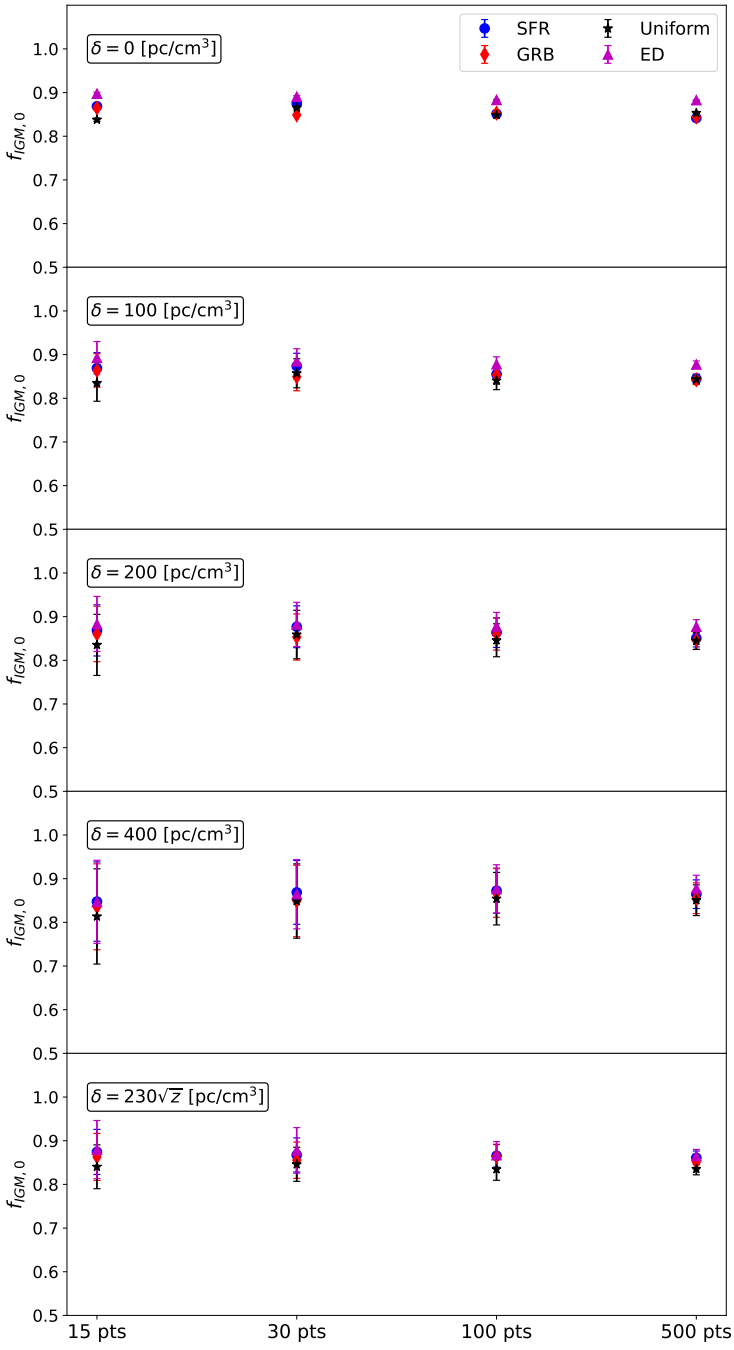

Figure 5.2: The results of our simulations for $f_{\mathrm{IGM},0}$. The data points represent the average values of these parameters for each distribution model discussed in the text, considering different sizes of samples and values of DM fluctuations.

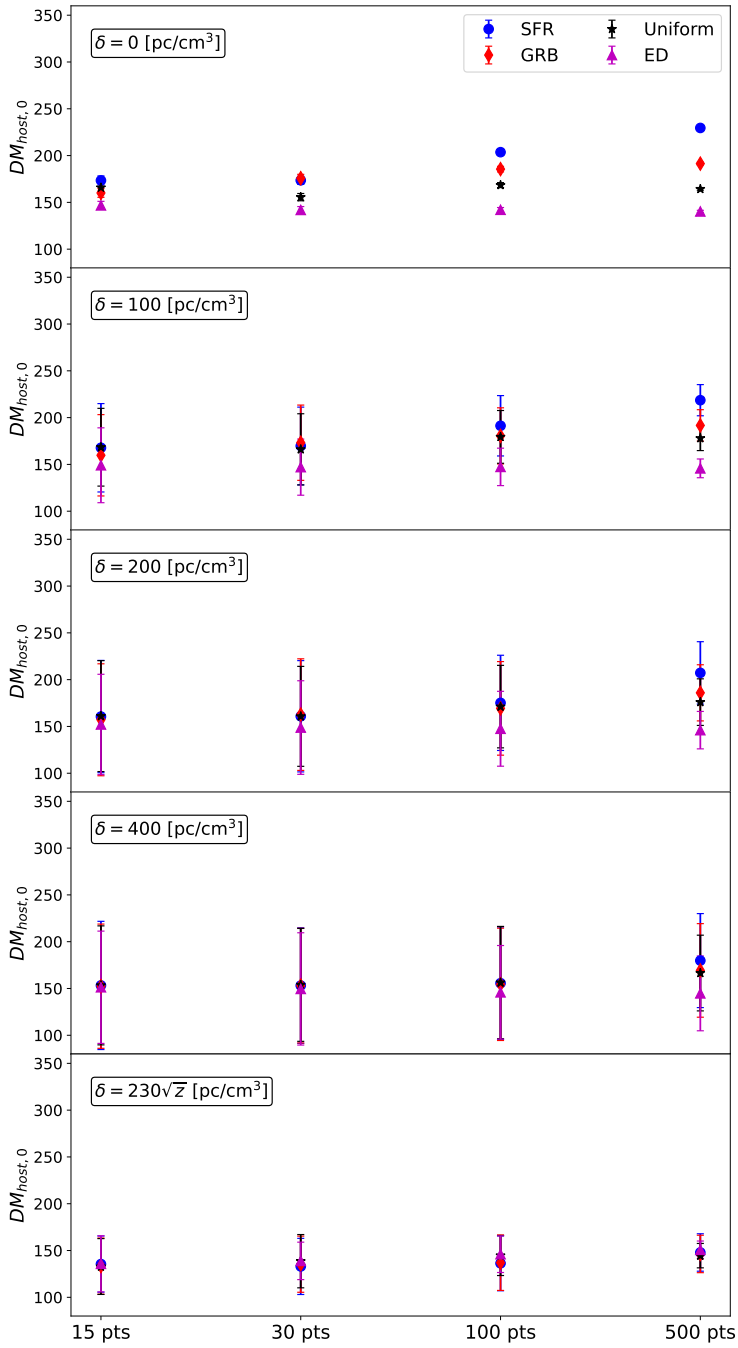

Figure 5.3: The same as in Figure 5.2 but now are the results of our simulations for $\mathrm{DM_{host,0}}$.

N	$f_{\rm IGM,0}$	$\rm DM_{host,0}$ [pc/cm^3]	$f_{\rm IGM,0}$	$\rm DM_{host,0}$ [pc/cm^3]
	SFR		GRB	
$\delta = 0$ pc/cm^3				
15	0.8686 ± 0.0032	173.43 ± 4.82	0.8645 ± 0.0034	160.05 ± 4.66
30	0.8743 ± 0.0026	173.55 ± 4.34	0.8487 ± 0.0029	175.80 ± 4.15
100	0.8512 ± 0.0018	203.64 ± 3.21	0.8529 ± 0.0019	185.53 ± 2.97
500	0.8417 ± 0.0009	229.52 ± 1.69	0.8442 ± 0.0009	191.39 ± 1.52
$\delta = 100$ pc/cm^3				
15	0.8689 ± 0.0357	167.76 ± 47.22	0.8638 ± 0.0385	159.74 ± 43.45
30	0.8737 ± 0.0294	169.66 ± 41.55	0.8491 ± 0.0320	173.18 ± 40.22
100	0.8551 ± 0.0201	191.28 ± 32.25	0.8537 ± 0.0214	180.48 ± 30.00
500	0.8447 ± 0.0108	218.62 ± 16.65	0.8423 ± 0.0110	191.68 ± 16.79
$\delta = 200$ pc/cm^3				
15	0.8685 ± 0.0586	160.56 ± 60.00	0.8603 ± 0.0635	157.12 ± 59.82
30	0.8768 ± 0.0479	160.88 ± 59.45	0.8533 ± 0.0528	162.64 ± 59.63
100	0.8634 ± 0.0340	175.20 ± 50.87	0.8601 ± 0.0367	169.30 ± 50.00
500	0.8505 ± 0.0199	207.24 ± 33.32	0.8456 ± 0.0207	185.92 ± 30.00
$\delta = 400$ pc/cm^3				
15	0.8475 ± 0.0908	153.26 ± 68.50	0.8356 ± 0.0984	152.44 ± 66.38
30	0.8686 ± 0.0731	153.12 ± 61.71	0.8489 ± 0.0818	153.06 ± 61.29
100	0.8725 ± 0.0515	155.64 ± 60.00	0.8674 ± 0.0558	154.42 ± 60.00
500	0.8645 ± 0.0327	179.80 ± 50.22	0.8552 ± 0.0351	169.30 ± 50.00
$\delta = 230\sqrt{z}$ pc/cm^3				
15	0.8743 ± 0.0516	135.50 ± 30.00	0.8629 ± 0.0538	133.36 ± 30.00
30	0.8674 ± 0.0391	133.00 ± 30.00	0.8554 ± 0.0416	135.38 ± 30.00
100	0.8654 ± 0.0257	136.32 ± 29.32	0.8646 ± 0.0272	137.00 ± 29.66
500	0.8608 ± 0.0156	147.90 ± 20.00	0.8511 ± 0.0161	146.32 ± 20.00

Table 5.3: The results of our simulations for $f_{\rm IGM,0}$ and $\rm DM_{host,0}$ considering the distribution models for SFR and GRB

N	$f_{\rm IGM,0}$	$\rm DM_{host,0}$ [pc/cm^3]	$f_{\rm IGM,0}$	$\rm DM_{host,0}$ [pc/cm^3]
	Uniform		ED	
$\delta = 0$ pc/cm^3				
15	0.8377 ± 0.0037	165.83 ± 4.47	0.8975 ± 0.0032	146.79 ± 4.30
30	0.8656 ± 0.0030	155.59 ± 3.89	0.8905 ± 0.0025	141.92 ± 3.60
100	0.8487 ± 0.0019	168.44 ± 2.66	0.8832 ± 0.0015	142.08 ± 2.40
500	0.8534 ± 0.0009	164.28 ± 1.31	0.8827 ± 0.0007	140.31 ± 1.20
$\delta = 100$ pc/cm^3				
15	0.8350 ± 0.0418	168.36 ± 41.54	0.8927 ± 0.0372	149.08 ± 40.00
30	0.8573 ± 0.0332	166.10 ± 38.03	0.8847 ± 0.0288	147.08 ± 30.00
100	0.8406 ± 0.0209	179.40 ± 28.19	0.8779 ± 0.0170	147.34 ± 20.00
500	0.8434 ± 0.0100	177.98 ± 13.21	0.8774 ± 0.0080	145.78 ± 10.02
$\delta = 200$ pc/cm^3				
15	0.8353 ± 0.0699	161.04 ± 59.26	0.8833 ± 0.0631	152.12 ± 53.61
30	0.8590 ± 0.0555	160.78 ± 53.40	0.8821 ± 0.0507	148.82 ± 50.00
100	0.8459 ± 0.0377	171.20 ± 44.07	0.8777 ± 0.0320	147.52 ± 40.00
500	0.8445 ± 0.0195	175.98 ± 24.90	0.8772 ± 0.0160	146.04 ± 20.00
$\delta = 400$ pc/cm^3				
15	0.8135 ± 0.1090	153.32 ± 63.58	0.8470 ± 0.0951	151.30 ± 60.00
30	0.8488 ± 0.0851	153.84 ± 60.32	0.8645 ± 0.0794	149.54 ± 60.00
100	0.8542 ± 0.0601	156.32 ± 60.00	0.8766 ± 0.0553	145.90 ± 50.00
500	0.8507 ± 0.0352	166.50 ± 40.45	0.8779 ± 0.0300	144.80 ± 40.00
$\delta = 230\sqrt{z}$ pc/cm^3				
15	0.8403 ± 0.0502	132.90 ± 29.83	0.8797 ± 0.0666	135.78 ± 30.00
30	0.8460 ± 0.0390	138.60 ± 28.46	0.8778 ± 0.0522	138.92 ± 20.00
100	0.8347 ± 0.0253	144.66 ± 21.39	0.8670 ± 0.0310	146.08 ± 19.58
500	0.8354 ± 0.0135	144.52 ± 13.03	0.8651 ± 0.0150	150.75 ± 9.40

Table 5.4: The same as in Table 5.3 except that we are considering now the Uniform and ED distributions.

Chapter 6

A search for the fine-structure constant evolution from fast radio bursts and type Ia supernovae data

This chapter presents the analysis originally reported in [230], in which we test a possible variation of the fine structure constant (α) from the method discussed in the previous chapters.

6.1 Introduction

The constancy of the fundamental constant of nature was probably first discussed by Dirac in his work named "Large numbers hypothesis" [231], marking the initial exploration of the constants of physics. This hypothesis suggested that the universal constants should be considered as variables characterizing the state of the Universe. The most of physical theories are based on the assumption that fundamental constants are truly constants. In this context, investigations on the space-time evolution of such constants are crucial in physics, as any deviation from our current physical theories could indicate the presence of new physics [232, 233].

The time evolution of the fundamental constants could arise from different physical mechanisms, such as the existence of new particles of dark matter, magnetic monopoles, or fundamental strings (see [234] for a recent review). From the cosmological point of view, there are several works that search for possible time evolution of these constants, such as the speed of light c [235], the gravitational constant G [236], the proton-to-electron mass ratio μ [237], among others [234]

An important fundamental constant of nature is the fine-structure constant ($\alpha \equiv$

$e^2/\hbar c$), which is associated with the electromagnetic interaction between elementary charged particles. Many works have recently suggested that the time variation of α as a way to alleviate some problems in cosmology, such as the Hubble tension [238–240] and the primordial helium-4 abundance tension [241] (see [242, 243] to discussion of time variation of α with other Big Bang Nucleosynthesis observations). However, a non-constant α has also several observational consequences related to the possible non-conservation of the number of photons along the geodesic, leading to a direct violation of the cosmic distance duality relation [244, 245] and a deviation from a black body spectrum of the cosmic microwave background (CMB) radiation [246, 247].

Most theories in which the fine-structure constant presents a time dependence involve a scalar field controlling such dependence [248–250]. In this scenario, there is the so-called runaway dilaton model, in which the dilaton plays the role of the scalar field responsible for coupling, yielding a time evolution of α [251, 252]. At low and intermediate redshifts, such evolution is given by $\frac{\Delta\alpha}{\alpha} = -\gamma \ln(1+z)$, where the constant parameter γ is the product of the current value of the coupling between the dilaton and hadronic matter and the variation of the dilaton field with respect to the scale factor at the present time (see e.g. [253, 254]). In this context, γ is the parameter of the model to be constrained, and any deviation from $\gamma = 0$ hints at the evidence for a temporal variation of the fine structure constant.

As was mentioned before, the FRBs can be used as an astrophysical and cosmological probe when DM is combined with the redshift of the host galaxy (see [30–33, 35, 209, 224], but there are some limitations in its application. Such as the limited number of well-localized FRBs events, and the poor knowledge about the dispersion measure's density fluctuations (δ), due to the spatial variation in cosmic electron distribution. Another issue when studying FRBs in cosmology is the host galaxy contribution of the FRBs ($\mathrm{DM_{host}}$), which depends on factors such as the galaxy type, the mass of the host galaxy as well as the relative orientation between the FRB source and the host [44].

Here we propose a cosmological model-independent method to test a possible time evolution of the fine-structure constant using the DM of FRBs combined with SNe data considering the runaway dilaton scenario. We derive all the relevant expressions for the DM dependence concerning the fine-structure constant and constrain the parameter γ from measurements of 17 well-localized FRBs and SNe data from the Pantheon compilation. We also use Monte Carlo simulations to investigate the potential of the method proposed when applied to larger samples of FRB measurements, we also forecast constraints on γ for data sets with $N = 500$ and $N = 1000$ points.

6.2 Dispersion Measure as a function of α

In this section, we aim to search for a time variation of α based on the DM features. In what follows, we will review the well-established concepts of the FRBs' time delay and dispersion measure (see Subsection 2.1.1).

Since the fine structure constant is give by relation $\alpha = e^2/\hbar c$, the plasma frequency (Eq. 2.2) can be written as a function of α

$$\omega_p^2 = \frac{2nhc\alpha}{m}. \tag{6.1}$$

Now let us replace it in the equation of the rate change of the arrival time with respect to observed frequency (Eq. 2.10), and assuming that the parameters n_e and α vary with respect to the redshift

$$\frac{dt_p}{d\omega} = \frac{1}{2}\frac{d}{d\omega}\int_0^z \frac{2nhc\alpha}{m}\frac{1}{(1+z')^2}\frac{dz'}{H(z')}. \tag{6.2}$$

The difference between integrals in the Equations 2.10 and 6.2 are the $\alpha(z')$ factor in the above equation. Then we multiple by a factor of α_0/α_0 and thus it is possible to recover Equation 2.10, if α is a constant in the redshift

$$\frac{dt_p}{d\omega} = -\frac{2h\alpha_0}{\omega_0^3 m}\int_0^z n(z')\frac{\alpha(z')}{\alpha_0}\frac{1}{(1+z')^2}\frac{cdz'}{H(z')}, \tag{6.3}$$

where $\alpha_0 = \alpha(z=0)$.

Consequently, the dispersion measure in IGM for a possible variation on the fine structure constant is

$$\mathrm{DM_{IGM}} = \int_0^z n(z')\frac{\alpha(z')}{\alpha_0}\frac{1}{(1+z')^2}\frac{cdz'}{H(z')}. \tag{6.4}$$

As long as the quantity usually measured is $\Delta\alpha(z)/\alpha_0$, we express the above equation in terms of this quantity and we also write the electronic density $n(z)$ following [29]

$$\mathrm{DM_{IGM}}(z) = \frac{7}{8}\cdot\frac{3c\Omega_b H_0^2}{8\pi G m_p}\int_0^z f_{\mathrm{IGM}}(z')\left(\frac{\Delta\alpha}{\alpha_0}(z')+1\right)\frac{(1+z')}{H(z')}dz'. \tag{6.5}$$

As expected, the last equation reduces to the standard case when $\alpha = \text{const}$. From the above relation, α is related to DM of FRBs. In what follows, we will focus on a phenomenological approach, using FRBs observations, to constrain cosmological parameters.

6.3 Runaway dilaton model

The most of theories that lead to a spacetime dependence of constants will involve a non-minimal coupling between a scalar field responsible for the variation and the matter fields [248–250], leading to violations of the Einstein Equivalence Principle. In our analysis, we focus on the runaway dilaton model [251, 252], which is a particular case of scalar-tensor theories of gravity inspired by a multiplicative coupling between an extra scalar field and the usual matter Lagrangian. In this case, the dilaton (ϕ) plays the role of the scalar field responsible for the coupling.

The basic idea behind this model is exploiting the string-loop modification of the (four-dimensional) effective low-energy action where the Lagrangian can be written as [252]:

$$\mathcal{L} = \frac{R}{16\pi G} - \frac{1}{8\pi G}(\nabla\phi)^2 - \frac{1}{4}B_F(\phi)F^2 + \dots, \tag{6.6}$$

where R is the Ricci scalar and B_F is the gauge coupling function. In this context, the time variation of fine structure constant is given by [252]

$$\frac{\Delta\alpha}{\alpha_0}(z) = \frac{1}{40}\beta_{\rm had,0}\left[1 - e^{(\phi(z)-\phi_0)}\right], \tag{6.7}$$

where $\beta_{\rm had,0}$ is the current value of the coupling between the dilaton and hadronic matter, and $\phi_0^{'} \equiv \frac{\partial\phi}{\partial \ln a}$. Since we are interested in the evolution of α at low redshift, it is a reasonable approximation to linearize the field evolution by

$$\phi \sim +\phi_0 + \ln a, \tag{6.8}$$

being a the scalar factor. In such way, Equation 6.7 becomes [252]

$$\frac{\Delta\alpha}{\alpha_0}(z) \approx -\frac{1}{40}\beta_{\rm had,0}\phi_0^{'}\ln(1+z) \equiv -\gamma\ln(1+z), \tag{6.9}$$

where $\gamma \equiv \frac{1}{40}\beta_{\rm had,0}\phi_0^{'}$ is the parameter of the model. It is important to stress that Eq. 6.9 can be considered in low and intermediate redshifts.

6.4 Dispersion Measure Components

Here we will discuss the components of the dispersion measure considering a possible time evolution of the fine structure constant given by relation 6.9. As we mentioned in Subsection 2.1.1, the host galaxy contribution is a poorly understood parameter due to the challenges in measurement and modeling. For this reason, we will write as

$$\mathrm{DM_{host}}(z) = \frac{\mathrm{DM_{host,0}}}{(1+z)} f(\alpha, z)\ , \tag{6.10}$$

where we will consider two parameterizations for $\mathrm{DM_{host}}$. The first is the case when $f(\alpha, z) = 1$ (hereafter named Fixed host), which corresponds to the usual approach that assumes contributions from all host galaxies are the same. The second parameterization takes into account the contribution from the fine-structure constant for each host galaxy. In this case (named α-dependent host), considering the runaway dilaton model discussed earlier, we have $f(\alpha, z) = -\gamma \ln(1+z) + 1$.

A cosmological model is typically assumed to solve the integral for $\mathrm{DM_{IGM}}(z)$ (eq. 4.3). In our analysis, we follow the approach discussed in [209] and integrate eq. 6.5 by parts using the definition of luminosity distance (Eq. 4.2.1) [211]

$$\begin{aligned} u &= (-\gamma \ln(1+z') + 1)(1+z') \longrightarrow du = (-\gamma - \gamma \ln(1+z') + 1)\, dz', \\ dv &= \frac{dz'}{H(z')} \longrightarrow v = \frac{d_L(z')}{(1+z')c}. \end{aligned} \tag{6.11}$$

By assuming the runaway dilaton model's parameterization for α and considering f_{IGM} as a constant in redshift ($f_{\mathrm{IGM}}(z) = f_{\mathrm{IGM,0}}$), the Equation 6.5 becomes

$$\begin{aligned} \mathrm{DM_{IGM}}(z) &= A f_{\mathrm{IGM,0}} \Bigg[(-\gamma \ln(1+z) + 1) \frac{d_L(z)}{c} + (\gamma - 1) \int_0^z \frac{d_L(z')}{(1+z')c} dz' \\ &+ \gamma \int_0^z \frac{d_L(z')}{(1+z')c} \ln(1+z') dz' \Bigg], \end{aligned} \tag{6.12}$$

where the above integrals can be numerically solved. The first integral is calculated using Eq. 4.5 and the second integral is obtained from the relation

$$\begin{aligned} \int_0^z \frac{d_L(z')}{(1+z')c} \ln(1+z') dz' &= \frac{1}{2c} \sum_{i=1}^{N} (z_{i+1} - z_i) \times \Bigg[\frac{d_L(z_{i+1})}{(1+z_{i+1})} \ln(1+z_{i+1}) \\ &+ \frac{d_L(z_i)}{(1+z_i)} \ln(1+z_i) \Bigg]. \end{aligned} \tag{6.13}$$

Note that in the case of $\gamma = 0$, the last equation returns to the constant case given by Eq. 4.4 (see Sec. 4.2).

From the above expressions, one can constrain a possible evolution of the fine structure constant by modeling both $\mathrm{DM_{host,0}}$ and $\mathrm{DM_{IGM}}$ and comparing the theoretical predictions with the observed values of $\mathrm{DM_{ext}}$. Specifically, by combining FRBs with the SNe dataset we can obtain cosmological model-independent con-

straints on γ, $f_{\rm IGM,0}$ and $\rm DM_{host,0}$, from the observational data sets described below.

6.5 Data set

In this work, we desire to constrain the possible evolution of α described in the previous section. Our analysis is based on observational and simulated FRBs data and SNe measurements.

FRBs: In Section 3.3.4, we show the most up-to-date sample of well-localized FRBs, which contains 39 events listed in Table 3.1. However, at the time of performing the analysis of this work, there were only 23 well-localized FRBs available in the literature. In our analysis, we exclude the following events: FRB 190614 [202], as it has no measurement of spectroscopic redshift and can be associated with two host galaxies; FRB 200110E [203] is estimated to be in the direction of M81, but a Milky Way halo origin can not be rejected; FRB 181030 [198] has a low-redshift ($z = 0.0039$) and it can not be associated with any SNe in the Pantheon catalog; FRB 20190520B [200] has a host galaxy contribution significantly larger than the other events; FRB 210117 [204] has an observed DM much larger for its redshift ($z = 0.2145$); and finally, FRB 20220610A [12] at $z = 1.016$, which will be removed from our sample for reasons discussed in Section 6.7.

In Table 6.1 we listed our working sample that contains 17 FRBs [137, 158, 183, 186, 190, 191, 196, 197, 199, 201, 204] and their main properties: redshift, the Galaxy contribution ($\rm DM_{MW,ISM}$) estimated from the NE2001 model [59], observed dispersion measure ($\rm DM_{obs}$), $\rm DM_{obs}$ uncertainty ($\sigma_{\rm obs}$) and the references.

The observational quantity $\rm DM_{ext}$ can be obtained from Table 3.1 using Equation 2.15 and its uncertainty can be expressed considering the total uncertainty given by the relation

$$\sigma_{\rm tot}^2 = \sigma_{\rm obs}^2 + \sigma_{\rm MW}^2 + \sigma_{\rm IGM}^2 + \left(\frac{\sigma_{\rm host,0}}{1+z}\right)^2 + \delta^2 \,, \tag{6.14}$$

where $\sigma_{\rm obs}$ is given in Table 3.1, the average galactic uncertainty $\sigma_{\rm MW}$ is assumed to be 10 pc/cm^3 [213] and δ is the fluctuations of DM which is related to the spatial variation in cosmic electron density along the line-of-sight (see Section 4.5). Therefore, we will treat them as a fixed value, $\delta = 230\sqrt{z}$ pc/cm^3 [42, 209], in the statistical analyses. Following reference [255], we adopt $\sigma_{\rm host,0} = 30$ pc/cm^3 as the uncertainty of $\rm DM_{host,0}$. Furthermore, the uncertainty of IGM contribution ($\sigma_{\rm IGM}$) can be calculated from error propagation of Eq. 6.12 given by

$$\sigma_{\rm IGM} = A f_{\rm IGM,0}\left[\left(-\gamma \ln\left(1+z\right)+1\right)^2 \frac{\sigma_{d_L}^2}{c^2} + (\gamma-1)^2\sigma_{\rm S}^2 + \gamma^2\sigma_{\rm I}^2\right]^{1/2}, \tag{6.15}$$

Name	Redshift z	DM_{ISM} [pc/cm^3]	$\mathrm{DM}_{\mathrm{obs}}$ [pc/cm^3]	σ_{obs} [pc/cm^3]	Reference
FRB 180916B	0.0337	200.0	348.8	0.2	[197]
FRB 201124A	0.098	123.2	413.52	0.5	[186]
FRB 190608B	0.1178	37.2	338.7	0.5	[201]
FRB 200430A	0.16	27.0	380.25	0.4	[190]
FRB 121102A	0.19273	188.0	557.0	2.0	[183]
FRB 191001A	0.234	44.7	506.92	0.04	[190]
FRB 190714A	0.2365	38.0	504.13	2.0	[190]
FRB 191228A	0.2432	33.0	297.5	0.05	[196]
FRB 190102C	0.291	57.3	363.6	0.3	[191]
FRB 180924B	0.3214	40.5	361.42	0.06	[158]
FRB 180301A	0.3305	152.0	536.0	8.0	[196]
FRB 200906A	0.3688	36.0	577.8	0.02	[196]
FRB 190611B	0.378	57.83	321.4	0.2	[190]
FRB 181112A	0.4755	102.0	589.27	0.03	[199]
FRB 190711A	0.522	56.4	593.1	0.4	[190]
FRB 190523A	0.66	37.0	760.8	0.6	[137, 190]
FRB 210320	0.2797	42.2	384.8	0.3	[204]

Table 6.1: Properties of FRB with known host galaxies

where σ_{d_L} is the luminosity distance uncertainty that is calculated from the SNe dataset, σ_{S} (Eq. 4.6) and σ_{I} are the uncertainties of the quantities in Equations 4.5 and 6.13, respectively. The last one is expressed by the equation below

$$\sigma_{\mathrm{I}}^2 = \frac{1}{2c}\sum_{i}^{N}(z_{i+1}-z_i)\left[\left(\frac{\ln(1+z_{i+1})}{1+z_{i+1}}\right)^2\sigma_{d_L(1+z_{i+1})}^2+\left(\frac{\ln(1+z)}{1+z}\right)^2\sigma_{d_L(1+z)}^2\right]^{1/2}. \tag{6.16}$$

SNe: We also use the largest combined sample of SNe having a total of 1048 events ranging in the redshift range $0.01 < z < 2.3$ named as "Pantheon Sample". We obtain d_L from the distance moduli ($\mu(z)$) relation given by Equation 4.12, where we fix $M_B = -19.214 \pm 0.037$ mag [214]. The error in luminosity distance can be expressed as

$$\sigma_{d_L} = \frac{\ln 10}{5} d_L \cdot \sqrt{\sigma_{m_B}^2 + \sigma_{M_B}^2}, \tag{6.17}$$

being σ_{m_B} and σ_{M_B} the apparent and absolute magnitude uncertainties, respectively.

To estimate d_L and its uncertainty at the same redshift of FRBs, we follow [209] and perform a GP reconstruction of the Pantheon data, using GaPP python library (see Appendix A).

	γ	$f_{\rm IGM,0}$	$\rm DM_{host,0}$ [pc/cm^3]
Fixed	$+0.04^{+0.47}_{-1.40}$	$0.75^{+0.16}_{-0.16}$	142^{+42}_{-36}
α-dependent	$-0.07^{+0.44}_{-1.39}$	$0.75^{+0.15}_{-0.25}$	142^{+40}_{-37}

Table 6.2: Results for γ, $f_{\rm IGM,0}$ and $\rm DM_{host,0}$ using the current FRB and SNe data and considering two cases of host contribution. The error bars correspond to 1σ level.

6.6 Results

We perform a MCMC analysis using the *emcee* package [215] to constrain the runaway dilaton model's parameter γ, $f_{\rm IGM,0}$ and $\rm DM_{host,0}$. In the analysis, we assume $\Omega_b h^2 = 0.02235 \pm 0.00037$, as reported in [217].

Figure 6.1 shows the posterior probability density function and $1-2\sigma$ contours for combinations of the parameters γ, $f_{\rm IGM,0}$ and $\rm DM_{host,0}$, considering parametrizations fixed host (top Panel) and α-dependent host (bottom Panel). The numerical results are presented in Table 6.2. As physically expected, both parameterizations have little impact on the estimates of $f_{\rm IGM,0}$ and $\rm DM_{host,0}$, and show results consistent with $\Delta\alpha/\alpha = 0$. However, in comparison with other cosmological constraints on the time-evolution of α, which place constraints on $\Delta\alpha/\alpha$ ranging from 10^{-2} to 10^{-7} over a large redshift interval (see, e.g. [253, 256–264]), the results shown in Table 6.2 reflect the limitation of the current FRB observations in tightly constraining cosmological parameters. In what follows, we simulate and forecast the constraining power of larger samples of FRBs to limit a possible time variation of α.

6.7 Simulations

As discussed in the previous chapter, there are only a few FRBs in the literature with measured redshift and the number of events is not enough to perform robust statistical analysis. For this reason, we perform a MC simulation to generate random points of $\rm DM_{ext}$ to study the impact of a larger sample of FRBs in constraining α.

As the redshift distribution of FRBs is not known, we consider two different redshift distribution models (see [224] for more explanation about the impact of the redshift distribution models of FRBs) described below:

- **Gamma-Ray Bursts:** Due to the similarities between GRBs and FRBs, many works in the literature assume this distribution for FRBs[228]. In this case, the density function is given by Equation 5.1.

- **Star Formation Rate:** The star formation rate distribution was proposed

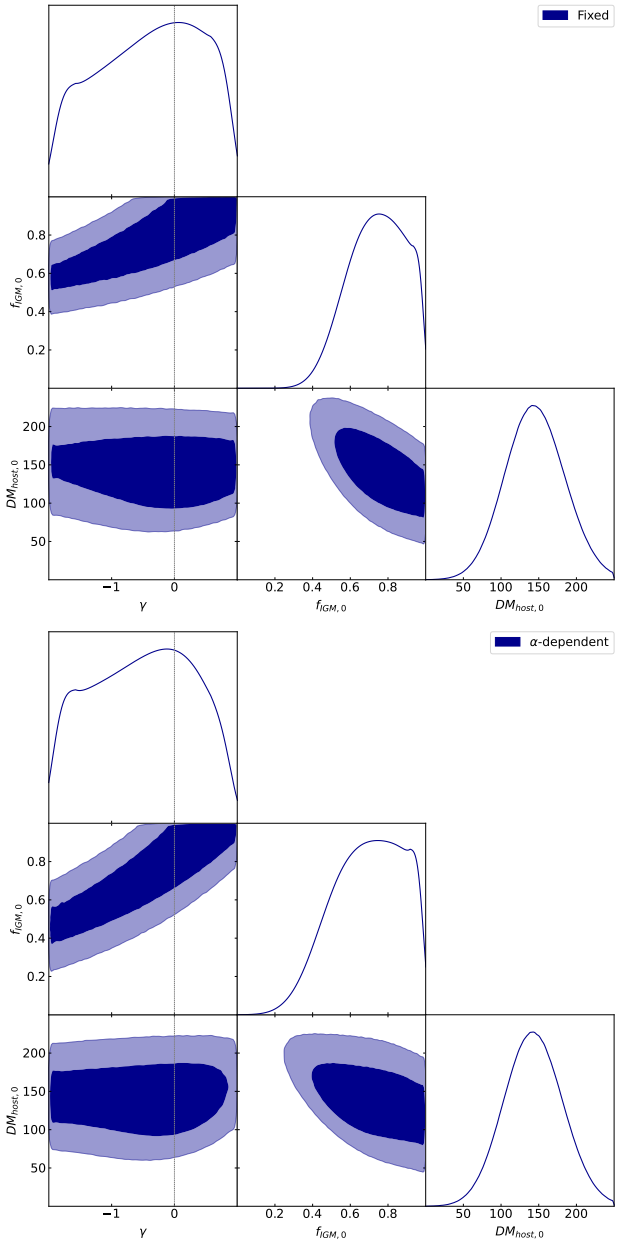

Figure 6.1: Constraints on the parameter of runaway dilaton model γ, the baryon fraction $f_{\rm IGM}$ and the host galaxy contribution $\rm DM_{host,0}$ for parameterizations Fixed (*top*) and α-dependent (*bottom*).

by [229] (for the first proposal of redshift distribution for FRBs, see Reference [225]). The spatial distribution of FRBs is expected to closely trace the cosmic one for young stellar FRB progenitors. The cosmic SFR function is written in Equation 5.2.

We follow the steps of simulations that we described in Section 5.3 (see also [224]):

1. We generate random points using both redshift distribution models presented above, within the redshift range $[0.022, 1.5]$, considering FRB samples with $N = 500$ and 1000 points.

2. The fiducial $\mathrm{DM_{ext}}$ ($\mathrm{DM_{ext}^{fid}}$) is calculated using Eq. 2.16, where $\mathrm{DM_{IGM}}$ is given by Eq. (2.19) and $\mathrm{DM_{host,0}}$ by in Eq. 6.10. However, for the last one, we consider two parameterizations: $f(\alpha, z) = 1$ (Fixed host) and $f(\alpha, z) = -\gamma \ln(z+1) + 1$ (α-dependent host). We adopt as fiducial values for the mean values of baryon fraction and host contribution the results obtained for the case $\gamma = 0$. In our simulations, we also adopt the values of $H_0 = 74.03 \pm 1.4$ $\mathrm{kms^{-1}Mpc^{-1}}$ [214], $\Omega_m = 0.3153$ [15] and $\Omega_b h^2 = 0.02235 \pm 0.00037$ [217].

3. We calculate the uncertainty of the simulated $\mathrm{DM_{ext}}$ ($\sigma_{\mathrm{ext}}^{\mathrm{sim}}$), by performing a hyperbolic regression fit of the observational relative error ($\eta = \sigma_{\mathrm{ext}}^{obs}/\mathrm{DM_{ext}^{obs}}$), given by $\eta = A/z$, where A is a hyperbolic regression free parameter.

4. The standard deviation of the Gaussian Distribution (sd) is obtained from the average distance between the observed ($\mathrm{DM_{ext}}$) and fiducial points ($\mathrm{DM_{ext}^{fid}}$) using Eq. 5.5.

5. Finally, we calculate the simulated $\mathrm{DM_{ext}}$ by assuming a normal distribution, given by $\mathrm{DM_{ext}^{sim}}(z) = \mathcal{N}(\mathrm{DM_{ext}^{fid}}, sd)$.

We perform the steps above 100 times for each sample size of the distribution models, which is enough to obtain convergence. In each simulation, we calculate the best fit of the free parameters and, subsequently, the average of each ensemble of 100 simulations. We present in Appendix C the figures with the best-fit results of our 100 realizations, probing the convergence of our simulations.

In Tables 6.3 and 6.4 we listed the numerical values obtained separately for all distributions and different numbers of points in each realization ($N = 500$ and 1000) for both host cases. For the redshift distribution models considered, the constraints on γ are significantly stronger than the current limits displayed in Table 6.2, with the error bar reaching 10^{-2} in most cases, and similar to the results obtained in References [253, 259, 261]. It is also worth mentioning that the results do not

	γ	$f_{\rm IGM,0}$	$\rm DM_{host,0}$ $[\rm pc/cm^3]$
SFR			
$N = 500$			
Fixed	$+0.0888^{+0.0365}_{-0.0972}$	$0.9993^{+0.0062}_{-0.0570}$	$125.20^{+21.31}_{-15.86}$
α-dependent	$+0.0197^{+0.0338}_{-0.1069}$	$0.9991^{+0.0067}_{-0.0641}$	$133.13^{+17.46}_{-15.99}$
$N = 1000$			
Fixed	$+0.0856^{+0.0364}_{-0.0938}$	$0.9993^{+0.0058}_{-0.0548}$	$123.20^{+14.90}_{-15.86}$
α-dependent	$+0.0338^{+0.0240}_{-0.0571}$	$0.9995^{+0.0036}_{-0.0351}$	$131.35^{+11.73}_{-11.32}$

Table 6.3: The results of our simulations for γ, $f_{\rm IGM,0}$ and $\rm DM_{host,0}$ considering the SFR distribution model.

	γ	$f_{\rm IGM,0}$	$\rm DM_{host,0}$ $[\rm pc/cm^3]$
GRB			
$N = 500$			
Fixed	$+0.2327^{+0.0477}_{-0.1997}$	$0.9733^{+0.0189}_{-0.1012}$	$110.21^{+21.32}_{-16.41}$
α-dependent	$+0.0138^{+0.0350}_{-0.1508}$	$0.9990^{+0.0095}_{-0.0871}$	$132.07^{+17.46}_{-15.55}$
$N = 1000$			
Fixed	$+0.2678^{+0.0318}_{-0.1262}$	$0.9868^{+0.0111}_{-0.0722}$	$105.47^{+14.90}_{-11.49}$
α-dependent	$+0.0317^{+0.0261}_{-0.0785}$	$0.9993^{+0.0050}_{-0.0478}$	$128.38^{+11.73}_{-10.92}$

Table 6.4: The at in Table 6.3, but now we are considering GRB distribution model.

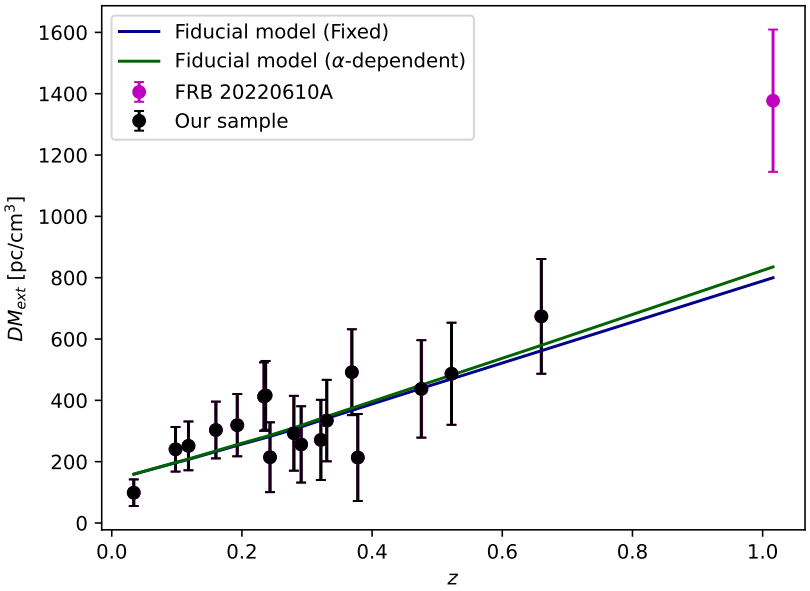

Figure 6.2: The evolution of $\mathrm{DM_{ext}}$ with redshift. Black points correspond to the 17 FRBs observations used in our analysis, while the pink point stands for the FRB 20220610A. Blue and green lines represent Fixed and α-dependent parameterizations, respectively. As discussed in the text, the fiducial model is calculated using Eq. (2.16), where $\mathrm{DM_{IGM}}$ is given by Eq. (2.19).

show significant improvements on the limits to γ (the same happens to $f_{\mathrm{IGM},0}$ and $\mathrm{DM_{host,0}}$) from $N = 500$ to $N = 1000$ cases, which may indicate that to improve the constraints on $\Delta\alpha/\alpha$ further (beyond $\sigma \simeq 10^{-2}$), the quality of the FRB data will play a crucial role in the future analyses.

Finally, as mentioned in Sec. 6.5, we removed from our analysis the FRB 20220610A [12] at $z = 1.016$. This FRB, observed in 2022 by the ASKAP [156], has a very high dispersion measure when we compare it with the other events (see Table 6.1). We performed tests including this FRB in our analysis and found significantly different values of the parameter of the runaway dilaton model for Fixed host and α-dependent host, i.e., $\gamma = -1.00^{+0.99}_{-0.15}$ and $\gamma = -0.96^{+0.92}_{-0.12}$ at 1σ, respectively. As shown in Figure 6.2, these results are inconsistent with the values found considering the sample with 17 FRBs (see Table 6.2), and that was the reason which led us to remove it from our analysis.

6.8 Summary

In this chapter, we presented a cosmological model-independent test of a possible time variation of the fine-structure constant based on the dispersion measure of

FRBs, combining FRBs data and SNe observations. We derived all the relevant expressions for the analyses and considered the runaway dilaton scenario, for which $\frac{\Delta\alpha}{\alpha} = -\gamma \ln(1+z)$. Our analysis constrained the parameter γ combining measurements of 17 well-localized FRBs and the Pantheon SNe compilation. We obtained results consistent with no variation of α and errors of the order of 10^{-1}, reflecting the current data's limitation to impose tight limits on $\alpha(z)$.

We also simulate the FRBs data using Monte Carlo method, testing the potential of the method proposed when applied to larger samples of FRB measurements. We extended the samples to $N = 500$ and $N = 1000$ data points and analyzed two distribution models for the FRBs: Star Formation Rate (SFR) and Gamma Ray Burst (GRB). The results demonstrated that the uncertainties on γ can be improved by one order of magnitude ($\sigma \sim 10^{-2}$), making it a competitive test when compared to other cosmological probes at the same redshift range. The lack of significant differences in the results regarding the number of points suggests that limits on $\frac{\Delta\alpha}{\alpha}$ beyond $\sigma \sim 10^{-2}$ will depend crucially on the quality of upcoming FRB data. Our results show the potential of the proposed method to impose constraints on a possible time evolution of the fine-structure constant with larger and more precise samples of FRBs, as expected from current and planned observational projects (see e.g. [52, 53, 156]).

Chapter 7

Conclusion

In this thesis, we investigated the main aspects of FRBs focusing on their main astrophysical characteristics and some cosmological applications. The FRBs are transient radio events with duration in the order of milliseconds and frequency of a few hundred to a few thousand MHz. Although many FRBs have been detected since the first burst discovered in 2007 by Parkes telescope [1], their source origin is still in debate. More than 50 source models have been proposed to explain their progenitor origin (Sec. 2.3), in which magnetars models are considered the best candidates because FRB 200428 [27] was discovered to be associated with active magnetars, but the physical mechanism responsible for the bursts is not known. The high brightness temperature ($T_b > 10^{32}$ K) and short duration (milliseconds or less) of FRBs bursts imply a coherent emission process (Sec. 2.2). From the processes to generate coherent radio emissions, coherent curvature emission and synchrotron maser emission from magnetized shocks are in the leading position.

Although almost one thousand events have been detected, only about 30 bursts had the host galaxy observed (Subsec. 3.3.4). For this reason, the current sample of FRBs with redshift known is not large enough for a good statistical analysis. This occurs because the identification of the host galaxy is very difficult, but when the host galaxy of the burst is identified, the redshift of the event can be measured directly. In this situation, z and DM can be combined, forming the $\mathrm{DM} - z$ relation. From this relation, it is possible to use FRBs as an astrophysical and cosmological probe. However, there are some limitations when studying FRBs in cosmology. For instance, the density fluctuations in the dispersion measure due to the spatial variation in cosmic electron distribution need to be better determined. Another limitation is the poor knowledge of the host galaxy contribution of the FRBs, which depends on many factors, such as the type of galaxy, the mass of the galaxy as well as the relative orientation between the FRB source with respect to the host. The last issue associated with the application of FRBs is related to the evolution of f_{IGM}, which is degenerated with cosmological parameters (Eq. 2.19).

In this scenario, we developed a cosmological-model independent method to determine the evolution of $f_{\rm IGM}$ and the local value of the $\rm DM_{host,0}$ (Sec. 4.2), by combining the 16 FRBs observations with localized host galaxy and GP reconstruction of current supernovae data from the Pantheon catalog. We adopted two parameterizations to $f_{\rm IGM}$, constant and time-dependent case (Eqs. 4.1 and 4.2, respectively), and consider different values of DM fluctuations (δ), which are due to the spatial variation in cosmic electron density. Our results show through a Bayesian model selection analysis, that a conclusive answer about the time-evolution of $f_{\rm IGM}$ depends strongly on the δ. In particular, our study shows that the evidence varies from strong (in favor of a growing evolution of $f_{\rm IGM}$ with redshift) to inconclusive, as larger values of δ are considered.

To investigate the impact of the number of FRBs observations and different redshift distribution models of FRBs to constrain the baryon fraction in the IGM and host galaxy contribution, we use a cosmological model-independent method developed in our previous work [209] to perform the analysis, in which we combine simulated FRB data from Monte Carlo simulation and GP reconstruction of SNe data. For the distribution models for the FRBs, we assume four cases: gamma-ray bursts, star formation rate, uniform, and equidistant. We also consider samples with $N = 15, 30, 100$ and 500 points and different values of the fluctuations of electron density in the DM, $\delta = 0, 100, 200, 400, 230\sqrt{z}$ pc/cm^3. Our analysis shows that all the distribution models present consistent results within 2σ for the free parameters $f_{\rm IGM}$ and $\rm DM_{host,0}$ and highlights the crucial role of DM fluctuations in obtaining more precise measurements.

Besides these analyses, we also search for a space-time variation of the fundamental constants. We use the DM of FRBs combined with SNe data to investigate a possible redshift evolution of the fine-structure constant (α). We derive all the relevant expressions for the DM dependence concerning the fine-structure constant in a cosmological model-independent way (Sec. 6.4), considering the runaway dilaton scenario, which predicts $\frac{\Delta\alpha}{\alpha} = -\gamma \ln(1+z)$, where γ is a constant proportional to the current value of the coupling between the dilaton field and hadronic matter. We constrain the parameter γ from measurements of 17 well-localized FRBs and GP reconstruction of the Pantheon compilation. We also use Monte Carlo simulations to forecast the constraining power of larger samples of FRB measurements for data sets with $N = 500$ and $N = 1000$ points, adopting a fixed value of DM fluctuations, $\delta = 230\sqrt{z}$ pc/cm^3. From our results, we found that the uncertainty on γ can be improved by one order of magnitude and that limits on $\frac{\Delta\alpha}{\alpha}$ beyond $\sigma \sim 10^{-2}$ will depend crucially on better control of statistical and systematic uncertainties of upcoming FRB data.

We expect that with the next generation of survey telescopes (for example,

ASKAP/CRACO [51], CHIME [52], and SKA1-Mid [53]), the number of FRBs with the host galaxy identified will increase, maximizing our understanding of observational properties—for instance, radiation mechanism, progenitor source, and also the density fluctuations in the dispersion measure (δ), and host galaxy contribution ($\mathrm{DM_{host}}$). We also expect an improvement in the constraints on astrophysical and cosmological parameters, like the baryon fraction in the IGM (f_{IGM}) and fine-structure constant (α) with these new surveys. As a perspective, we plan to test fundamental hypotheses of the standard cosmological model (SCM), which are the General Relativity and the Cosmological Principle, and possible variations of the fundamental constants of nature. Our goal is to test the isotropy of the Universe and search for a possible variation of the speed of the light using observational data and simulations of FRBs. We will focus on model-independent tests to avoid previous assumptions on the large-scale evolution of the Universe.

Bibliography

[1] D. R. Lorimer, M. Bailes, M. A. McLaughlin, and et al. A bright millisecond radio burst of extragalactic origin. *Science*, 318(5851):777–780, November 2007.

[2] D. Thornton, B. Stappers, M. Bailes, and et al. A population of fast radio bursts at cosmological distances. *Science*, 341(6141):53–56, July 2013.

[3] E. Petroff, J. W. T. Hessels, and D. R. Lorimer. Fast radio bursts. *The Astronomy and Astrophysics Review*, 27(1), May 2019.

[4] D. Michilli, A. Seymour, J. W. T. Hessels, and et al. An extreme magneto-ionic environment associated with the fast radio burst source frb 121102. *Nature*, 553(7687):182–185, January 2018.

[5] D. Xiao, F. Wang, and Z. Dai. The physics of fast radio bursts. *Science China Physics, Mechanics & Astronomy*, 64(4), February 2021.

[6] J. J. Condon and S. M. Ransom. *Essential Radio Astronomy*. 2016.

[7] J. W. T. Hessels, L. G. Spitler, A. D. Seymour, and et al. FRB 121102 bursts show complex time–frequency structure. *ApJL*, 876(2):L23, May 2019.

[8] L. G. Spitler, P. Scholz, J. W. T. Hessels, and et al. A repeating fast radio burst. *Nature*, 531(7593):202–205, March 2016.

[9] D. Li, P. Wang, W. W. Zhu, and et al. A bimodal burst energy distribution of a repeating fast radio burst source. *Nature*, 598(7880):267–271, October 2021.

[10] Y.-K. Zhang, P. Wang, Y. Feng, and et al. FAST observations of an extremely active episode of FRB 20201124A. ii. energy distribution. *Research in Astronomy and Astrophysics*, 22(12):124002, November 2022.

[11] B. Zhang. The physics of fast radio bursts. *Reviews of Modern Physics*, 95(3), September 2023.

[12] S. D. Ryder, K. W. Bannister, S. Bhandari, and et al. A luminous fast radio burst that probes the universe at redshift 1. *Science*, 382(6668):294–299, October 2023.

[13] C. Clarkson and R. Maartens. Inhomogeneity and the foundations of concordance cosmology. *Classical and Quantum Gravity*, 27(12):124008, May 2010.

[14] T. Clifton, P. G. Ferreira, A. Padilla, and et al. Modified gravity and cosmology. *Physics Reports*, 513(1–3):1–189, March 2012.

[15] N. Aghanim, Y. Akrami, M. Ashdown, and et al. Planck 2018 results: Vi. cosmological parameters. *A&A*, 641:A6, September 2020.

[16] A. G. Riess, A. V. Filippenko, P. Challis, and et al. Observational evidence from supernovae for an accelerating universe and a cosmological constant. *The Astronomical Journal*, 116(3):1009–1038, September 1998.

[17] S. Perlmutter, G. Aldering, G. Goldhaber, and et al. Measurements of Ω and Λ from 42 high-redshift supernovae. *The Astronomical Journal*, 517(2):565–586, June 1999.

[18] C. L. Bennett, D. Larson, J. L. Weiland, and et al. Nine-year wilkinson microwave anisotropy probe (WMAP) observations: Final maps and results. *The Astrophysical Journal Supplement Series*, 208(2):20, September 2013.

[19] L. Perivolaropoulos and F. Skara. Challenges for ΛCDM: An update. *New Astronomy Reviews*, 95:101659, December 2022.

[20] S. Weinberg. The cosmological constant problem. *Rev. Mod. Phys.*, 61:1–23, Jan 1989.

[21] L. Verde, T. Treu, and A. G. Riess. Tensions between the early and late universe. *Nature Astronomy*, 3(10):891–895, September 2019.

[22] S. Capozziello, G. Sarracino, and G. De Somma. A critical discussion on the h_0 tension. *Universe*, 10(3):140, March 2024.

[23] Z. Pleunis, D. Michilli, C. G. Bassa, and et al. Lofar detection of 110–188 MHz emission and frequency-dependent activity from FRB 20180916b. *ApJL*, 911(1):L3, April 2021.

[24] V. Gajjar, A. P. V. Siemion, D. C. Price, and et al. Highest Frequency Detection of FRB 121102 at 4-8 GHz Using the Breakthrough Listen Digital Backend at the Green Bank Telescope. *ApJ*, 863(1):2, August 2018.

[25] M. Amiri, B. C. Andersen, K. Bandura, and et al. The first CHIME/FRB fast radio burst catalog. *The Astrophysical Journal Supplement Series*, 257(2):59, December 2021.

[26] E. Platts, A. Weltman, A. Walters, and et al. A living theory catalogue for fast radio bursts. *Physics Reports*, 821:1–27, August 2019.

[27] C. D. Bochenek, V. Ravi, K. V. Belov, and et al. A fast radio burst associated with a galactic magnetar. *Nature*, 587(7832):59–62, November 2020.

[28] K. Dolag, B. M. Gaensler, A. M. Beck, and M. C. Beck. Constraints on the distribution and energetics of fast radio bursts using cosmological hydrodynamic simulations, 2015.

[29] W. Deng and B. Zhang. Cosmological implications of fast radio burst/gamma-ray burst associations. *ApJ*, 783(2):L35, February 2014.

[30] Robert Reischke and Steffen Hagstotz. Consistent constraints on the equivalence principle from localized fast radio bursts. *MNRAS*, 523(4):6264–6271, June 2023.

[31] H.-N. Lin and Y. Sang. Probing the anisotropic distribution of baryon matter in the universe using fast radio bursts. *Chinese Physics C*, 45(12):125101, December 2021.

[32] A. Walters, A. Weltman, B. M. Gaensler, and et al. Future cosmological constraints from fast radio bursts. *ApJ*, 856(1):65, March 2018.

[33] J.-J. Wei, X.-F. Wu, and H. Gao. Cosmology with gravitational wave/fast radio burst associations. *ApJL*, 860(1):L7, June 2018.

[34] Q. Wu, H. Yu, and F. Y. Wang. A new method to measure Hubble parameter $H(z)$ using fast radio bursts. *ApJ*, 895(1):33, May 2020.

[35] Q. Wu, G.-Q. Zhang, and F.-Y. Wang. An 8% determination of the Hubble constant from localized fast radio bursts. *Monthly Notices of the Royal Astronomical Society: Letters*, 515(1):L1–L5, March 2022.

[36] S. Hagstotz, R. Reischke, and R. Lilow. A new measurement of the Hubble constant using fast radio bursts. *MNRAS*, 511(1):662–667, January 2022.

[37] Z. Li, H. Gao, J.-J. Wei, and et al. Cosmology-independent estimate of the fraction of baryon mass in the IGM from fast radio burst observations. *ApJ*, 876(2):146, May 2019.

[38] J.-J. Wei, Z. Li, H. Gao, and et al. Constraining the evolution of the baryon fraction in the IGM with FRB and $H(z)$ data. *JCAP*, 2019(09):039–039, September 2019.

[39] Z. Li, H. Gao, J.-J. Wei, and et al. Cosmology-insensitive estimate of IGM baryon mass fraction from five localized fast radio bursts. *Monthly Notices of the Royal Astronomical Society: Letters*, 496(1):L28–L32, May 2020.

[40] Matthew McQuinn. Locating the "missing" baryons with extragalactic dispersion measure estimates. *ApJ*, 780(2):L33, December 2013.

[41] J.-P. Macquart, J. X. Prochaska, M. McQuinn, and et al. A census of baryons in the universe from localized fast radio bursts. *Nature*, 581(7809):391–395, May 2020.

[42] R. Takahashi, K. Ioka, A. Mori, and et al. Statistical modelling of the cosmological dispersion measure. *MNRAS*, 502(2):2615–2629, January 2021.

[43] J. Baptista, J. X. Prochaska, A. G. Mannings, and et al. Measuring the variance of the macquart relation in z-DM modeling, 2023.

[44] J. Xu and J. L. Han. Extragalactic dispersion measures of fast radio bursts. *Research in Astronomy and Astrophysics*, 15(10):1629–1638, Oct 2015.

[45] R. Cen and J. P. Ostriker. Where are the baryons? *ApJ*, 514(1):1–6, March 1999.

[46] R. Cen and J. P. Ostriker. Where are the baryons? II. Feedback effects. *ApJ*, 650(2):560–572, October 2006.

[47] A. A. Meiksin. The physics of the intergalactic medium. *Reviews of Modern Physics*, 81(4):1405–1469, Oct 2009.

[48] M. Fukugita and P. J. E. Peebles. The cosmic energy inventory. *ApJ*, 616(2):643–668, December 2004.

[49] J. M. Shull, B. D. Smith, and C. W. Danforth. The baryon census in a multiphase intergalactic medium: 30% of the baryons may still be missing. *ApJ*, 759(1):23, October 2012.

[50] J. C. Hill, S. Ferraro, N. Battaglia, and et al. Kinematic uppercaseSunyaev-Zel'dovich effect with projected fields: A novel probe of the baryon distribution with Planck, WMAP, and WISE data. *Physical Review Letters*, 117(5), July 2016.

[51] C. W. James, E. M. Ghosh, J. X. Prochaska, and et al. A measurement of hubble's constant using fast radio bursts. *MNRAS*, 516(4):4862–4881, September 2022.

[52] A. E. Lanman, S. Andrew, M. Lazda, and et al. CHIME/FRB Outriggers: KKO Station System and Commissioning Results, 2024.

[53] P. Dewdney, P. Hall, R. Schilizzi, and et al. The Square Kilometre Array. *Proceedings of the IEEE*, 97:1482 – 1496, 09 2009.

[54] V. Ravi, M. Catha, G. Chen, and et al. Deep Synoptic Array Science: Discovery of the Host Galaxy of FRB 20220912A. *ApJL*, 949(1):L3, May 2023.

[55] M. V. dos Santos, R. G. Landim, G. A. Hoerning, and et al. The BINGO Project: IX. search for fast radio bursts – a forecast for the uppercase-BINGO interferometry system. *A&A*, 681:A120, January 2024.

[56] G. B. Rybicki and A. P. Lightman. *Radiative processes in astrophysics*. 1979.

[57] Z. Zheng, E. O. Ofek, S. R. Kulkarni, and et al. Probing the intergalactic medium with fast radio bursts. *ApJ*, 797(1):71, November 2014.

[58] H. Gao, Z. Li, and B. Zhang. FAST RADIO BURST/GAMMA-RAY BURST COSMOGRAPHY. *ApJ*, 788(2):189, Jun 2014.

[59] J. M. Cordes and T. J. W. Lazio. Ne2001.i. a new model for the galactic distribution of free electrons and its fluctuations, 2003.

[60] J. M. Yao, R. N. Manchester, and N. Wang. A NEW ELECTRON-DENSITY MODEL FOR ESTIMATION OF PULSAR AND FRB DISTANCES. *ApJ*, 835(1):29, Jan 2017.

[61] J. H. Taylor and J. M. Cordes. Pulsar Distances and the Galactic Distribution of Free Electrons. *ApJ*, 411:674, July 1993.

[62] J. X. Prochaska and Y. Zheng. Probing galactic halos with fast radio bursts. *MNRAS*, January 2019.

[63] C. R. H. Walker, Y.-Z. Ma, and R. P. Breton. Constraining the redshifts of unlocalised fast radio bursts. *A&A*, 638:A37, June 2020.

[64] K. Ioka. The cosmic dispersion measure from gamma-ray burst afterglows: Probing the reionization history and the burst environment. *ApJ*, 598(2):L79–L82, nov 2003.

[65] G. D. Becker, J. S. Bolton, M. G. Haehnelt, and et al. Detection of extended he ii reionization in the temperature evolution of the intergalactic medium. *MNRAS*, 410(2):1096–1112, nov 2010.

[66] J. M. Cordes and M. A. McLaughlin. Searches for fast radio transients. *ApJ*, 596(2):1142–1154, October 2003.

[67] S. Xu and B. Zhang. On the origin of the scatter broadening of fast radio burst pulses and astrophysical implications. *ApJ*, 832(2):199, December 2016.

[68] J. M. Cordes, R. S. Wharton, L. G. Spitler, and et al. Radio wave propagation and the provenance of fast radio bursts, 2016.

[69] V. Ravi, R. M. Shannon, M. Bailes, and et al. The magnetic field and turbulence of the cosmic web measured using a brilliant fast radio burst. *Science*, 354(6317):1249–1252, December 2016.

[70] B. Marcote, Z. Paragi, J. W. T. Hessels, and et al. The Repeating Fast Radio Burst FRB 121102 as Seen on Milliarcsecond Angular Scales. *ApJL*, 834(2):L8, January 2017.

[71] O. Y. Tsupko and G.S. Bisnovatyi-Kogan. On gravitational lensing in the presence of a plasma. *Gravitation and Cosmology*, 18(2):117–121, 2012.

[72] O. Y. Tsupko and G. S. Bisnovatyi-Kogan. Gravitational lensing in plasma: Relativistic images at homogeneous plasma. *Phys. Rev. D*, 87:124009, Jun 2013.

[73] X. Er and S. Mao. Effects of plasma on gravitational lensing. *MNRAS*, 437(3):2180–2186, 11 2013.

[74] X. Er and S. Mao. The effects of plasma on the magnification and time delay of strongly lensed fast radio bursts. *MNRAS*, 516(2):2218–2222, August 2022.

[75] J. M. Cordes, I. Wasserman, J. W. T. Hessels, and et al. Lensing of fast radio bursts by plasma structures in host galaxies. *ApJ*, 842(1):35, June 2017.

[76] X. Er, Y.-P. Yang, and A. Rogers. The effects of plasma lensing on the inferred dispersion measures of fast radio bursts. *ApJ*, 889(2):158, February 2020.

[77] CHIME/FRB Collaboration, B. C. Andersen, K. Bandura, M. Bhardwaj, and et al. CHIME/FRB Discovery of Eight New Repeating Fast Radio Burst Sources. *ApJL*, 885(1):L24, November 2019.

[78] K. Nimmo, J. W. T. Hessels, A. Keimpema, and et al. Highly polarized microstructure from the repeating FRB 20180916B. *Nature Astronomy*, 5:594–603, June 2021.

[79] S. Dai, J. Lu, C. Wang, and et al. On the Circular Polarization of Repeating Fast Radio Bursts. *ApJ*, 920(1):46, October 2021.

[80] C. K Day, A. T Deller, R. M Shannon, and et al. High time resolution and polarization properties of ASKAP-localized fast radio bursts. *MNRAS*, 497(3):3335–3350, July 2020.

[81] H. Cho, J.-P. Macquart, R. M. Shannon, and et al. Spectropolarimetric analysis of FRB 181112 at microsecond resolution: Implications for fast radio burst emission mechanism. *ApJL*, 891(2):L38, March 2020.

[82] P. Chawla, B. C. Andersen, M. Bhardwaj, and et al. Detection of repeating FRB 180916.J0158+65 down to frequencies of 300 mhz. *ApJL*, 896(2):L41, June 2020.

[83] M. Pilia, M. Burgay, A. Possenti, and et al. The lowest-frequency fast radio bursts: Sardinia Radio Telescope detection of the periodic FRB 180916 at 328 MHz. *ApJL*, 896(2):L40, June 2020.

[84] E. Parent, P. Chawla, V. M. Kaspi, and et al. First discovery of a fast radio burst at 350 MHz by the GBNCC Survey. *ApJ*, 904(2):92, November 2020.

[85] I. Pastor-Marazuela, L. Connor, J. van Leeuwen, and et al. Chromatic periodic activity down to 120 megahertz in a fast radio burst. *Nature*, 596(7873):505–508, August 2021.

[86] D. B. Melrose. Coherent radio emission from pulsars. *Philosophical Transactions: Physical Sciences and Engineering*, 341(1660):105–115, 1992.

[87] D. B. Melrose. Coherent emission. *Proceedings of the International Astronomical Union*, 4(S257):305–315, 2008.

[88] D. B. Melrose. Coherent emission mechanisms in astrophysical plasmas. *Reviews of Modern Plasma Physics*, 1(1), July 2017.

[89] M. A. Ruderman and P. G. Sutherland. Theory of pulsars: polar gaps, sparks, and coherent microwave radiation. *ApJ*, 196:51–72, February 1975.

[90] J. I. Katz. Coherent emission in fast radio bursts. *Physical Review D*, 89(10), May 2014.

[91] P. Kumar, W. Lu, and M. Bhattacharya. Fast radio burst source properties and curvature radiation model. *MNRAS*, 468(3):2726–2739, March 2017.

[92] W. Lu and P. Kumar. On the radiation mechanism of repeating fast radio bursts. *MNRAS*, 477(2):2470–2493, March 2018.

[93] J. I. Katz. Coherent plasma-curvature radiation in FRB. *MNRAS*, 481(3):2946–2950, September 2018.

[94] Y.-P. Yang and B. Zhang. Bunching coherent curvature radiation in three-dimensional magnetic field geometry: Application to pulsars and fast radio bursts. *ApJ*, 868(1):31, November 2018.

[95] A. J. Cooper and R. A. M. J. Wijers. Coherent curvature radiation: maximum luminosity and high-energy emission. *MNRAS: Letters*, 508(1):L32–L36, August 2021.

[96] K. S. Cheng and J. L. Zhang. General Radiation Formulae for a Relativistic Charged Particle Moving in Curved Magnetic Field Lines: The Synchrocurvature Radiation Mechanism. *ApJ*, 463:271, May 1996.

[97] R. Buschauer and G. Benford. General theory of coherent curvature radiation. *MNRAS*, 177:109–136, October 1976.

[98] G. Benford and R. Buschauer. Coherent pulsar radio radiation by antenna mechanisms: general theory. *MNRAS*, 179:189–207, April 1977.

[99] A. Saggion. Curvature Hadiation by Bunches of Particles. *A&A*, 44:285, November 1975.

[100] A. F. Cheng and M. A. Ruderman. Bunching mechanism for coherent curvature radiation in pulsar magnetospheres. *ApJ*, 212:800–806, March 1977.

[101] A. Kaganovich and Y. Lyubarsky. Curvature-drift instability fails to generate pulsar radio emission. *ApJ*, 721(2):1164–1173, September 2010.

[102] D. B. Melrose. Collective plasma radiation processes. *Annual Rev. Astron. Astrophys.*, 29:31–57, January 1991.

[103] D. B. Melrose and M. E. Gedalin. Relativistic plasma emission and pulsar radio emission: A critique. *ApJ*, 521(1):351, Aug 1999.

[104] J. P. Wild, S. F. Smerd, and A. A. Weiss. Solar Bursts. *Annual Rev. Astron. Astrophys.*, 1:291, January 1963.

[105] V. V. Zheleznyakov. *Radiation in Astrophysical Plasmas*, volume 204. Springer Dordrecht, 1996.

[106] V. V. Zheleznyakov, G. Thejappa, S. A. Koryagin, and R. G. Stone. Synchrotron Maser: A "New" Emission Process. *Geophysical Monograph Series*, 119:57–66, January 2000.

[107] G. Ghisellini. Synchrotron masers and fast radio bursts. *MNRAS*, 465(1):L30–L33, February 2017.

[108] Q. Luo and D. B. Melrose. Curvature maser emission due to field line torsion in pulsar magnetospheres. *MNRAS*, 276(2):372–382, 09 1995.

[109] Y. Lyubarsky. A model for fast extragalactic radio bursts. *MNRAS: Letters*, 442(1):L9–L13, April 2014.

[110] I. Plotnikov and L. Sironi. The synchrotron maser emission from relativistic shocks in fast radio bursts: 1d pic simulations of cold pair plasmas. *MNRAS*, 485(3):3816–3833, March 2019.

[111] A.-N. Babul and L. Sironi. The synchrotron maser emission from relativistic magnetized shocks: dependence on the pre-shock temperature. *MNRAS*, 499(2):2884–2895, September 2020.

[112] Y. A. Gallant, M. Hoshino, A. B. Langdon, and et al. Relativistic, Perpendicular Shocks in Electron-Positron Plasmas. *ApJ*, 391:73, May 1992.

[113] J. P. Freidberg. *Ideal MHD*. Cambridge University Press, 2014.

[114] G. F. Burgio, H. J. Schulze, I. Vidaña, and et al. Neutron stars and the nuclear equation of state. *Progress in Particle and Nuclear Physics*, 120:103879, 2021.

[115] R. C. Duncan and C. Thompson. Formation of Very Strongly Magnetized Neutron Stars: Implications for Gamma-Ray Bursts. *ApJL*, 392:L9, June 1992.

[116] C. Thompson and R. C. Duncan. Neutron Star Dynamos and the Origins of Pulsar Magnetism. *ApJ*, 408:194, May 1993.

[117] V. M. Kaspi and A. M. Beloborodov. Magnetars. *Annual Rev. Astron. Astrophys.*, 55(1):261–301, August 2017.

[118] S. B. Popov and K. A. Postnov. Hyperflares of sgrs as an engine for millisecond extragalactic radio bursts, 2007.

[119] B. Zhang. Coherent inverse compton scattering by bunches in fast radio bursts. *ApJ*, 925(1):53, January 2022.

[120] M. Lyutikov. Coherent emission in pulsars, magnetars, and fast radio bursts: Reconnection-driven free electron laser. *ApJ*, 922(2):166, November 2021.

[121] A. Philippov, A. Timokhin, and A. Spitkovsky. Origin of pulsar radio emission. *Physical Review Letters*, 124(24), June 2020.

[122] Y.-P. Yang and B. Zhang. Fast radio bursts and their high-energy counterparts from magnetar magnetospheres. *ApJ*, 919(2):89, September 2021.

[123] A. D. Kuzmin. Giant pulses of pulsar radio emission. *Astrophysics and Space Science*, 308(1–4):563–567, March 2007.

[124] J. M. Cordes and Ira Wasserman. Supergiant pulses from extragalactic neutron stars. *MNRAS*, 457(1):232–257, January 2016.

[125] L. Connor, J. Sievers, and U.-L. Pen. Non-cosmological FRBs from young supernova remnant pulsars. *MNRAS: Letters*, 458(1):L19–L23, February 2016.

[126] M. Lyutikov, L. Burzawa, and S. B. Popov. Fast radio bursts as giant pulses from young rapidly rotating pulsars. *MNRAS*, 462(1):941–950, July 2016.

[127] J. I. Katz. Fast radio bursts as pulsar lightning. *MNRAS: Letters*, 469(1):L39–L42, April 2017.

[128] B. Zhang. A "cosmic comb" model of fast radio bursts. *ApJL*, 836(2):L32, February 2017.

[129] K. Ioka and B. Zhang. A binary comb model for periodic fast radio bursts. *ApJL*, 893(1):L26, April 2020.

[130] J. I. Katz. FRB as products of accretion disc funnels. *MNRAS: Letters*, 471(1):L92–L95, July 2017.

[131] J. I. Katz. Are fast radio bursts made by neutron stars? *MNRAS: Letters*, 494(1):L64–L68, February 2020.

[132] J. I. Katz. Precession and Jitter in FRB 180916b. *MNRAS: Letters*, 516(1):L58–L60, July 2022.

[133] L.-B. Li, Y.-F. Huang, J.-J. Geng, and et al. A model of fast radio bursts: collisions between episodic magnetic blobs. *Research in Astronomy and Astrophysics*, 18(6):061, June 2018.

[134] N. Sridhar, B. D. Metzger, P. Beniamini, and et al. Periodic fast radio bursts from luminous X-ray binaries. *ApJ*, 917(1):13, August 2021.

[135] G. E. Romero, M. V. del Valle, and F. L. Vieyro. Mechanism for fast radio bursts. *Physical Review D*, 93(2), January 2016.

[136] F. L. Vieyro, G. E. Romero, V. Bosch-Ramon, and et al. A model for the repeating FRB 121102 in the AGN scenario. *A&A*, 602:A64, June 2017.

[137] V. Ravi, M. Catha, L. D'Addario, and et al. A fast radio burst localized to a massive galaxy. *Nature*, 572(7769):352–354, July 2019.

[138] H. Falcke and L. Rezzolla. Fast radio bursts: the last sign of supramassive neutron stars. *A&A*, 562:A137, February 2014.

[139] E. R. Most, A. Nathanail, and L. Rezzolla. Electromagnetic emission from blitzars and its impact on non-repeating fast radio bursts. *The Astrophysical Journal*, 864(2):117, September 2018.

[140] M.-H. Wang, S.-K. Ai, Z.-X. Li, and et al. Testing the hypothesis of a compact-binary-coalescence origin of fast radio bursts using a multimessenger approach. *The Astrophysical Journal Letters*, 891(2):L39, March 2020.

[141] K. Kashiyama, K. Ioka, and P. Mészáros. Cosmological fast radio bursts from binary white dwarf mergers. *The Astrophysical Journal*, 776(2):L39, October 2013.

[142] B. Zhang. Mergers of Charged Black Holes: Gravitational-wave Events, Short Gamma-Ray Bursts, and Fast Radio Bursts. *ApJL*, 827(2):L31, August 2016.

[143] B. Zhang. Charged compact binary coalescence signal and electromagnetic counterpart of plunging black hole–neutron star mergers. *The Astrophysical Journal Letters*, 873(2):L9, March 2019.

[144] T. Totani. Cosmological fast radio bursts from binary neutron star mergers. *Publications of the Astronomical Society of Japan*, 65(5), October 2013.

[145] Z. G. Dai, X. Y. Wang, X. F. Wu, and B. Zhang. X-ray Flares from Postmerger Millisecond Pulsars. *Science*, 311(5764):1127–1129, February 2006.

[146] B. Zhang. Early X-Ray and Optical Afterglow of Gravitational Wave Bursts from Mergers of Binary Neutron Stars. *ApJL*, 763(1):L22, January 2013.

[147] C. Finlay, B. A Bassett, M. Kunz, and et al. Trajectory-based RFI subtraction and calibration for radio interferometry. *MNRAS*, 524(3):3231–3251, July 2023.

[148] S.A.K. Leeney, W.J. Handley, and E.L. Acedo. Bayesian approach to radio frequency interference mitigation. *Physical Review D*, 108(6), September 2023.

[149] B. Engelbrecht, M. G. Santos, J. Fonseca, and et al. Radio Frequency Interference from Radio Navigation Satellite Systems: simulations and comparison to MeerKat single-dish data, 2024.

[150] D. Pang, K. Goseva-Popstojanova, T. Devine, and et al. A novel single-pulse search approach to detection of dispersed radio pulses using clustering and supervised machine learning. *MNRAS*, 480(3):3302–3323, August 2018.

[151] L. Staveley-Smith, W. E. Wilson, T. S. Bird, and et al. The Parkes 21 CM multibeam receiver. *PASA*, 13(3):243–248, November 1996.

[152] Radio-radar telescope will probe solar system. *Electrical Engineering*, 80(7):561–561, 1961.

[153] P. Jiang, Y. Yue, H. Gan, and et al. Commissioning progress of the FAST, 2019.

[154] T. M. Colegate and N. Clarke. Searching for fast radio transients with SKA Phase 1. *Publications of the Astronomical Society of Australia*, 28(4):299–316, 2011.

[155] Y. Maan and J. van Leeuwen. Real-time searches for fast transients with Apertif and LOFAR. In *2017 XXXIInd General Assembly and Scientific Symposium of the International Union of Radio Science (URSI GASS)*. IEEE, August 2017.

[156] A. W. Hotan, J. D. Bunton, A. P. Chippendale, and et al. Australian square kilometre array pathfinder: I. system description. *Publications of the Astronomical Society of Australia*, 38, 2021.

[157] M. Amiri, K. Bandura, A. Boskovic, and et al. An Overview of CHIME, the Canadian Hydrogen Intensity Mapping Experiment. *The Astrophysical Journal Supplement Series*, 261(2):29, July 2022.

[158] K. W. Bannister, A. T. Deller, C. Phillips, and et al. A single fast radio burst localized to a massive galaxy at cosmological distance. *Science*, 365(6453):565–570, August 2019.

[159] A. Karastergiou, J. Chennamangalam, W. Armour, and et al. Limits on fast radio bursts at 145 MHz with artemis, a real-time software backend. *MNRAS*, 452(2):1254–1262, July 2015.

[160] C. J. Law, M. W. Abruzzo, C. G. Bassa, and et al. A Multi-telescope Campaign on FRB 121102: Implications for the FRB Population. *ApJ*, 850(1):76, November 2017.

[161] M. CHIME/FRB Collaboration: Amiri, K. Bandura, M. Bhardwaj, and et al. A second source of repeating fast radio bursts. *Nature*, 566(7743):235–238, January 2019.

[162] K. Masui, H.-H. Lin, J. Sievers, and et al. Dense magnetized plasma associated with a fast radio burst. *Nature*, 528(7583):523–525, December 2015.

[163] B. C. CHIME/FRB Collaboration: Andersen, K. M. Bandura, M. Bhardwaj, and et al. A bright millisecond-duration radio burst from a galactic magnetar. *Nature*, 587(7832):54–58, November 2020.

[164] D. J. Zhou, J. L. Han, B. Zhang, and et al. FAST observations of an extremely active episode of FRB 20201124A: I. burst morphology. *Research in Astronomy and Astrophysics*, 22(12):124001, November 2022.

[165] L. G. Spitler, J. M. Cordes, J. W. T. Hessels, and et al. Fast Radio Burst Discovered in the Arecibo Pulsar ALFA Survey. *ApJ*, 790(2):101, August 2014.

[166] D. Palaniswamy, Y. Li, and B. Zhang. Are there multiple populations of fast radio bursts? *ApJL*, 854(1):L12, February 2018.

[167] L. Connor. Interpreting the distributions of FRB observables. *MNRAS*, 487(4):5753–5763, June 2019.

[168] P. Kumar, R. M. Shannon, S. Osłowski, and et al. Faint repetitions from a bright fast radio burst source. *ApJL*, 887(2):L30, December 2019.

[169] Z. Pleunis, D. C. Good, V. M. Kaspi, and et al. Fast radio burst morphology in the first CHIME/FRB Catalog. *ApJ*, 923(1):1, December 2021.

[170] J.-W. Luo, J.-M. Zhu-Ge, and B. Zhang. Machine learning classification of CHIME fast radio bursts – I. Supervised methods. *MNRAS*, 518(2):1629–1641, November 2022.

[171] J.-M. Zhu-Ge, J.-W. Luo, and B. Zhang. Machine learning classification of CHIME fast radio bursts – II. Unsupervised methods. *MNRAS*, 519(2):1823–1836, December 2022.

[172] Y. G. Zhang, V. Gajjar, G. Foster, and et al. Fast radio burst 121102 pulse detection and periodicity: A machine learning approach. *ApJ*, 866(2):149, October 2018.

[173] D. M. Hewitt, M. P. Snelders, J. W. T. Hessels, and et al. Arecibo observations of a burst storm from FRB 20121102A in 2016. *MNRAS*, 515(3):3577–3596, July 2022.

[174] H. Xu, J. R. Niu, P. Chen, and et al. A fast radio burst source at a complex magnetized site in a barred galaxy. *Nature*, 609(7928):685–688, September 2022.

[175] J.-R. Niu, W.-W. Zhu, B. Zhang, and et al. FAST observations of an extremely active episode of FRB 20201124A. iv. spin period search. *Research in Astronomy and Astrophysics*, 22(12):124004, November 2022.

[176] M. Amiri, B. C. Andersen, K. M. Bandura, and et al. Periodic activity from a fast radio burst source. *Nature*, 582(7812):351–355, June 2020.

[177] M. Cruces, L. G. Spitler, P. Scholz, and et al. Repeating behaviour of FRB 121102: periodicity, waiting times, and energy distribution. *MNRAS*, 500(1):448–463, October 2020.

[178] K. M. Rajwade, M. B. Mickaliger, B. W. Stappers, and et al. Possible periodic activity in the repeating FRB 121102. *MNRAS*, 495(4):3551–3558, May 2020.

[179] P. Beniamini, Z. Wadiasingh, and Brian D Metzger. Periodicity in recurrent fast radio bursts and the origin of ultralong period magnetars. *MNRAS*, 496(3):3390–3401, June 2020.

[180] M. Lyutikov, M. V. Barkov, and D. Giannios. FRB periodicity: Mild pulsars in tight O/B-star binaries. *ApJL*, 893(2):L39, April 2020.

[181] J. J. Zanazzi and D. Lai. Periodic fast radio bursts with neutron star free precession. *ApJL*, 892(1):L15, March 2020.

[182] Y. Levin, A. M. Beloborodov, and A. Bransgrove. Precessing flaring magnetar as a source of repeating FRB 180916.J0158+65. *ApJL*, 895(2):L30, May 2020.

[183] S. Chatterjee, C. J. Law, R. S. Wharton, and et al. A direct localization of a fast radio burst and its host. *Nature*, 541(7635):58–61, January 2017.

[184] S. P. Tendulkar, C. G. Bassa, J. M. Cordes, and et al. The Host Galaxy and Redshift of the Repeating Fast Radio Burst FRB 121102. *ApJL*, 834(2):L7, January 2017.

[185] B. D. Metzger, E. Berger, and B. Margalit. Millisecond magnetar birth connects FRB 121102 to superluminous supernovae and long-duration gamma-ray bursts. *ApJ*, 841(1):14, May 2017.

[186] C. K. Day, S. Bhandari, A. T. Deller, and et al. ASKAP localisation of the FRB 20201124A source. *The Astronomer's Telegram*, 14515:1, April 2021.

[187] W.-f. Fong, Y. Dong, J. Leja, and et al. Chronicling the host galaxy properties of the remarkable repeating FRB 20201124A. *ApJL*, 919(2):L23, September 2021.

[188] L. Piro, G. Bruni, E. Troja, and et al. The fast radio burst FRB 20201124A in a star-forming region: Constraints to the progenitor and multiwavelength counterparts. *A&A*, 656:L15, December 2021.

[189] V. Ravi, C. J. Law, D. Li, and et al. The host galaxy and persistent radio counterpart of FRB 20201124A. *MNRAS*, 513(1):982–990, April 2022.

[190] K. E. Heintz, J. X. Prochaska, S. Simha, and et al. Host galaxy properties and offset distributions of fast radio bursts: Implications for their progenitors. *ApJ*, 903(2):152, November 2020.

[191] S. Bhandari, E. M. Sadler, J. X. Prochaska, and et al. The host galaxies and progenitors of fast radio bursts localized with the Australian Square Kilometre Array Pathfinder. *ApJL*, 895(2):L37, June 2020.

[192] Y. Li and B. Zhang. A comparative study of host galaxy properties between fast radio bursts and stellar transients. *ApJL*, 899(1):L6, August 2020.

[193] A. Spanakis-Misirlis and C. L. Van Eck. Frbstats: A web-based platform for visualization of fast radio burst properties. *The Open Journal of Astrophysics*, 6, February 2023.

[194] J. Xu, Y. Feng, D. Li, and et al. Blinkverse: A Database of Fast Radio Bursts. *Universe*, 9(7):330, July 2023.

[195] E. K. Mahony, R. D. Ekers, J.-P. Macquart, and et al. A search for the host galaxy of FRB 171020. *ApJL*, 867(1):L10, October 2018.

[196] S. Bhandari, K. E. Heintz, K. Aggarwal, and et al. Characterizing the fast radio burst host galaxy population and its connection to transients in the local and extragalactic universe. *The Astronomical Journal*, 163(2):69, January 2022.

[197] B. Marcote, K. Nimmo, J. W. T. Hessels, and et al. A repeating fast radio burst source localized to a nearby spiral galaxy. *Nature*, 577(7789):190–194, January 2020.

[198] M. Bhardwaj, A. Y. Kirichenko, D. Michilli, and et al. A local universe host for the repeating fast radio burst FRB 20181030A. *ApJL*, 919(2):L24, September 2021.

[199] J. X. Prochaska, J.-P. Macquart, M. McQuinn, and et al. The low density and magnetization of a massive galaxy halo exposed by a fast radio burst. *Science*, 366(6462):231–234, October 2019.

[200] S. K. Ocker, J. M. Cordes, S. Chatterjee, and et al. The large dispersion and scattering of FRB 20190520B are dominated by the host galaxy. *ApJ*, 931(2):87, May 2022.

[201] J. S. Chittidi, S. Simha, A. Mannings, and et al. Dissecting the local environment of FRB 190608 in the spiral arm of its host galaxy. *ApJ*, 922(2):173, November 2021.

[202] C. J. Law, B. J. Butler, J. X. Prochaska, and et al. A distant fast radio burst associated with its host galaxy by the very large array. *ApJ*, 899(2):161, August 2020.

[203] M. Bhardwaj, A. Y. Kirichenko, D. Michilli, and et al. A nearby repeating fast radio burst in the direction of m81. *ApJL*, 910(2):L18, March 2021.

[204] R. M. Shannon. CRAFT Transient FRB Discovery Report for 2023-02-04. *Transient Name Server Fast Radio Bursts*, 287:1, February 2023.

[205] R. M. Shannon and P. Uttarkar. CRAFT Transient FRB Discovery Report for 2023-03-02. *Transient Name Server Fast Radio Bursts*, 469:1, March 2023.

[206] C. J. Law, K. Sharma, V. Ravi, and et al. Deep Synoptic Array Science: First FRB and host galaxy catalog, 2024.

[207] B. Zhang. Fast radio burst energetics and detectability from high redshifts. *ApJL*, 867(2):L21, November 2018.

[208] L. S. Sparke and III Gallagher, J. S. *Galaxies in the universe : an introduction*. 2000.

[209] T. Lemos, R. S Gonçalves, J. C Carvalho, and et al. Cosmological model-independent constraints on the baryon fraction in the IGM from fast radio bursts and supernovae data. *EPJC*, 83(2):138, 2023.

[210] D. M. Scolnic, D. O. Jones, A. Rest, and et al. The complete light-curve sample of spectroscopically confirmed SNe Ia from Pan-STARRS1 and cosmological constraints from the combined Pantheon sample. *ApJ*, 859(2):101, May 2018.

[211] S. Weinberg. *Cosmology*. Cosmology. OUP Oxford, 2008.

[212] R. F. L. Holanda, J. C. Carvalho, and J. S. Alcaniz. Model-independent constraints on the cosmic opacity. *JCAP*, 2013(04):027–027, April 2013.

[213] R. N. Manchester, G. B. Hobbs, A. Teoh, and et al. The Australia Telescope National Facility Pulsar Catalogue. *The Astronomical Journal*, 129(4):1993–2006, April 2005.

[214] A. G. Riess, S. Casertano, W. Yuan, and et al. Large magellanic cloud cepheid standards provide a 1% foundation for the determination of the Hubble constant and stronger evidence for physics beyond ΛCDM. *ApJ*, 876(1):85, May 2019.

[215] D. Foreman-Mackey, David W. Hogg, D. Lang, and et al. emcee: The MCMC Hammer. *Publications of the Astronomical Society of the Pacific*, 125(925):306–312, March 2013.

[216] M Jaroszynski. Fast radio bursts and cosmological tests. *MNRAS*, 484(2):1637–1644, January 2019.

[217] R. J. Cooke, M. Pettini, and C. C. Steidel. One percent determination of the primordial deuterium abundance. *ApJ*, 855(2):102, March 2018.

[218] M. Fukugita, C. J. Hogan, and P. J. E. Peebles. The cosmic baryon budget. *ApJ*, 503(2):518–530, August 1998.

[219] J.-P. Dai and J.-Q. Xia. Reconstruction of baryon fraction in intergalactic medium through dispersion measurements of fast radio bursts. *MNRAS*, 503(3):4576–4580, March 2021.

[220] H. Jeffreys. *Theory of Probability*. International series of monographs on physics. Clarendon Press, 1998.

[221] F. Feroz and M. P. Hobson. Multimodal nested sampling: an efficient and robust alternative to Markov Chain Monte Carlo methods for astronomical data analyses: Multimodal nested sampling. *MNRAS*, 384(2):449–463, January 2008.

[222] F. Feroz, M. P. Hobson, and M. Bridges. MultiNest: an efficient and robust Bayesian inference tool for cosmology and particle physics. *MNRAS*, 398(4):1601–1614, Sep 2009.

[223] F. Feroz, M. P. Hobson, E. Cameron, and et al. Importance nested sampling and the CultiNest algorithm. *The Open Journal of Astrophysics*, 2(1), November 2019.

[224] T. Lemos, R. Gonçalves, J. Carvalho, and et al. Forecasting constraints on the baryon mass fraction in the IGM from fast radio bursts and type Ia supernovae. *EPJC*, 83(12), December 2023.

[225] M. Bhattacharya, P. Kumar, and E. V. Linder. Fast radio burst dispersion measure distribution as a probe of helium reionization. *Physical Review D*, 103(10), May 2021.

[226] R. C. Zhang, Bi. Zhang, Y. Li, and D. R. Lorimer. On the energy and redshift distributions of fast radio bursts. *MNRAS*, 501(1):157–167, November 2020.

[227] D.-C. Qiang and H. Wei. Effect of redshift distributions of fast radio bursts on cosmological constraints. *Physical Review D*, 103(8), April 2021.

[228] L. Shao, Z.-G. Dai, Y.-Z. Fan, and et al. Implications of understanding short gamma-ray bursts detected by \it swift. *ApJ*, 738:19, 2011.

[229] P. Madau and M. Dickinson. Cosmic star-formation history. *Annual Review of Astronomy and Astrophysics*, 52(1):415–486, August 2014.

[230] T. Lemos, R. Gonçalves, J. Carvalho, and et al. A search for the fine-structure constant evolution from fast radio bursts and type Ia supernovae data, 2024.

[231] P. A. M. Dirac. The cosmological constants. *Nature*, 139:323–323, 1937.

[232] J.-P. Uzan. The fundamental constants and their variation: observational and theoretical status. *Reviews of Modern Physics*, 75(2):403–455, April 2003.

[233] J.-P. Uzan. Varying constants, gravitation and cosmology. *Living Reviews in Relativity*, 14(1), March 2011.

[234] C. J. A. P. Martins. The status of varying constants: a review of the physics, searches and implications. *Reports on Progress in Physics*, 80(12):126902, November 2017.

[235] J. Magueijo. New varying speed of light theories. *Reports on Progress in Physics*, 66(11):2025, Oct 2003.

[236] E. Gaztañaga, E. García-Berro, J. Isern, and et al. Bounds on the possible evolution of the gravitational constant from cosmological type-Ia supernovae. *Physical Review D*, 65(2), December 2001.

[237] M. S. Safronova, D. Budker, D. DeMille, and et al. Search for new physics with atoms and molecules. *Reviews of Modern Physics*, 90(2), June 2018.

[238] L. Hart and J. Chluba. Updated fundamental constant constraints from Planck 2018 data and possible relations to the Hubble tension. *MNRAS*, 493(3):3255–3263, February 2020.

[239] L. Hart and J. Chluba. Varying fundamental constants principal component analysis: additional hints about the Hubble tension. *MNRAS*, 510(2):2206–2227, October 2021.

[240] O. Seto and Y. Toda. Big bang nucleosynthesis constraints on varying electron mass solution to the Hubble tension. *Physical Review D*, 107(8), April 2023.

[241] O. Seto, T. Takahashi, and Y. Toda. Variation of the fine structure constant in light of recent helium abundance measurement. *Physical Review D*, 108(2), July 2023.

[242] C. J. A. P. Martins. Primordial nucleosynthesis with varying fundamental constants: Degeneracies with cosmological parameters. *A&A*, 646:A47, February 2021.

[243] M. Deal and C. J. A. P. Martins. Primordial nucleosynthesis with varying fundamental constants: Solutions to the lithium problem and the deuterium discrepancy. *A&A*, 653:A48, September 2021.

[244] O. Minazzoli and A. Hees. Late-time cosmology of a scalar-tensor theory with a universal multiplicative coupling between the scalar field and the matter Lagrangian. *Physical Review D*, 90(2), July 2014.

[245] A. Hees, O. Minazzoli, and J. Larena. Breaking of the equivalence principle in the electromagnetic sector and its cosmological signatures. *Physical Review D*, 90(12), December 2014.

[246] P. A. R. Ade, N. Aghanim, M. Arnaud, and et al. Planck intermediate results: XXIV. constraints on variations in fundamental constants. *A&A*, 580:A22, July 2015.

[247] T. L. Smith, D. Grin, D. Robinson, and et al. Probing spatial variation of the fine-structure constant using the CMB. *Physical Review D*, 99(4), February 2019.

[248] G. Dvali and M. Zaldarriaga. Changing α with time: Implications for fifth-force-type experiments and quintessence. *Physical Review Letters*, 88(9), February 2002.

[249] T. Chiba and K. Kohri. Quintessence cosmology and varying α. *Progress of Theoretical Physics*, 107(3):631–636, March 2002.

[250] C. J. A. P. Martins. Fundamental cosmology in the E-ELT era: the status and future role of tests of fundamental coupling stability. *General Relativity and Gravitation*, 47(1), December 2014.

[251] T. Damour, F. Piazza, and G. Veneziano. Runaway dilaton and equivalence principle violations. *Physical Review Letters*, 89(8), August 2002.

[252] T. Damour, F. Piazza, and G. Veneziano. Violations of the equivalence principle in a dilaton-runaway scenario. *Physical Review D*, 66(4), August 2002.

[253] R. F. L. Holanda, S. J. Landau, J. S. Alcaniz, and et al. Constraints on a possible variation of the fine structure constant from galaxy cluster data. *JCAP*, 2016(05):047–047, May 2016.

[254] C. J. A. P. Martins, P. E. Vielzeuf, M. Martinelli, and et al. Evolution of the fine-structure constant in runaway dilaton models. *Physics Letters B*, 743:377–382, April 2015.

[255] Z. Li, H. Gao, J.-J. Wei, and et al. Cosmology-independent estimate of the fraction of baryon mass in the IGM from fast radio burst observations. *ApJ*, 876(2):146, May 2019.

[256] F. D. Albareti, J. Comparat, C. M. Gutiérrez, and et al. Constraint on the time variation of the fine-structure constant with the SDSS-III/BOSS DR12 quasar sample. *MNRAS*, 452(4):4153–4168, August 2015.

[257] S. M. Kotuš, M. T. Murphy, and R. F. Carswell. High-precision limit on variation in the fine-structure constant from a single quasar absorption system. *MNRAS*, 464(3):3679–3703, October 2016.

[258] M. C. D. Marsh. Exacerbating the cosmological constant problem with interacting dark energy models. *Physical Review Letters*, 118(1), January 2017.

[259] R. F. L. Holanda, L. R. Colaço, R. S. Gonçalves, and et al. Limits on evolution of the fine-structure constant in runaway dilaton models from Sunyaev–Zeldovich observations. *Physics Letters B*, 767:188–192, April 2017.

[260] J.-J. Zhang, L. Yin, and C.-Q. Geng. Cosmological constraints on $\Lambda(\alpha)$CDM models with time-varying fine structure constant. *Annals of Physics*, 397:400–409, October 2018.

[261] L. R. Colaço, R. F. L. Holanda, R. Silva, and et al. Galaxy clusters and a possible variation of the fine structure constant. *JCAP*, 2019(03):014–014, March 2019.

[262] S. J. Landau. Variation of fundamental constants and white dwarfs. *Proceedings of the International Astronomical Union*, 15(S357):45–59, October 2019.

[263] L. Lopez-Honorez, O. Mena, S. Palomares-Ruiz, and et al. Variations in fundamental constants at the cosmic dawn. *JCAP*, 2020(06):026–026, June 2020.

[264] R. S. Gonçalves, S. Landau, J. S. Alcaniz, and et al. Variation in the fine-structure constant and the distance-duality relation. *JCAP*, 2020(06):036–036, June 2020.

[265] M. Seikel, C. Clarkson, and M. Smith. Reconstruction of dark energy and expansion dynamics using gaussian processes. *JCAP*, 2012(06):036–036, June 2012.

[266] J. E. González, J. S. Alcaniz, and J. C. Carvalho. Non-parametric reconstruction of cosmological matter perturbations. *JCAP*, 2016(04):016–016, April 2016.

[267] S. Santos-da Costa, V. C. Busti, and R. F. L. Holanda. Two new tests to the distance duality relation with galaxy clusters. *JCAP*, 2015(10):061–061, October 2015.

[268] Z. Li, J. E. Gonzalez, H. Yu, and et al. Constructing a cosmological model-independent Hubble diagram of type Ia supernovae with cosmic chronometers. *Physical Review D*, 93(4), February 2016.

[269] R. Trotta. Bayes in the sky: Bayesian inference and model selection in cosmology. *Contemporary Physics*, 49(2):71–104, March 2008.

[270] R. Trotta. Bayesian methods in cosmology, 2017.

Appendix A

Gaussian Process

Gaussian Process (GP) [265, 266] is the generalization of a Gaussian distribution (distribution of a random variable) that describes a distribution over functions. GP constitutes a powerful method to reconstruct the expected function that describes the behavior of a given data where is not necessary to assume any model or parametric function to describe the data. This method has been applied to reconstruct several cosmological quantities, such as the dark energy equation of state [265], the duality-distance parameter [267] and to infer the H_0 [268].

Let us consider W the expected function formed from a GP. The value of function W at point z ($W(z)$) is not independent of the function value at some other point z' ($W(z')$), being z and z' two different and not independent points. The functions $W(z)$ and $W(z')$ are related by a covariance function ($k(z, z')$), also called as kernel. $k(z, z')$ is an indicator of the interaction of the states (z, z'), playing a very important role in the GP regression. The squared exponential kernel is the kernel function most used for GP regression that can be written as

$$k(z, z') = \sigma^2 \exp\left(-\frac{||z - z'||^2}{2l^2}\right), \tag{A.1}$$

where σ is the hyperparameter that describes the signal variance, which determines the average distance of the data-generating function from its means. The other hyperparameter, l, is related to the length scale between two points z and z'. The advantage of this function is that it is infinitely differentiable, which is useful for reconstructing the derivative of a function.

In order to perform the non-parametric reconstruction of the SNe data, we use the GaPP python library (for details of GaPP[1], see [265]) with a square exponential covariance function and optimize its hyperparameters by maximizing the GP's likelihood to obtain the reconstruction $m_B(z)$ and its uncertainty. We reconstructed 10^6 points of the function within the range $0.02 < z < 2.26$ which is illustrated in

[1]https://github.com/astrobengaly/GaPP

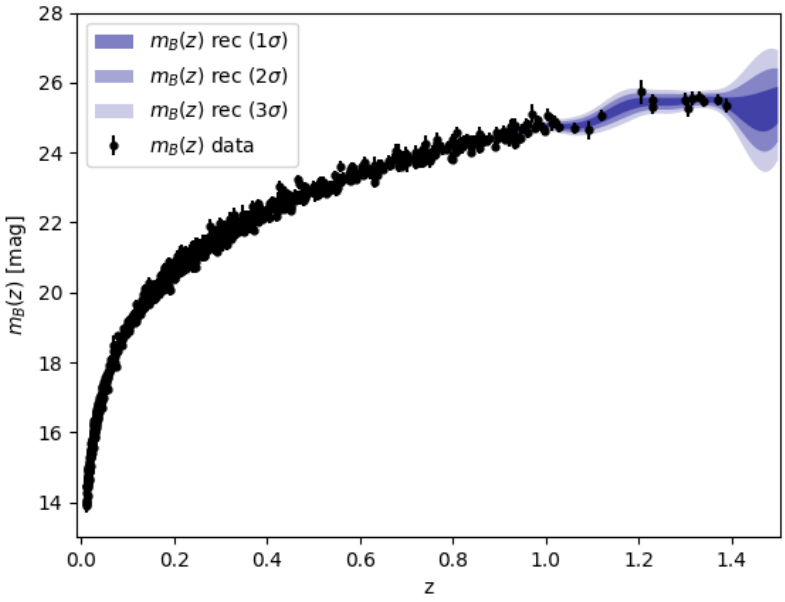

Figure A.1: GP reconstruction of the apparent magnitude of SNe Pantheon dataset.

Figure A.1. Note that the GP reconstruction of the Pantheon dataset overestimates the uncertainty values for $z > 1.5$, as the number of SNe in this interval is small.

Appendix B

Bayes factor

The Bayesian inference is a statistical technique used for parameter estimation and model selection (see e.g. [269, 270] for a detailed discussion). Based on the Bayes' theorem, this inference method updates the probability for a hypothesis (or model) as more information (or data) becomes available. The Bayes' theorem provides the posterior probability $\mathcal{P}$ for a set of parameters θ, given the data d, described by a model $\mathcal{M}$

$$\mathcal{P}(\theta|d,\mathcal{M}) = \frac{\mathcal{L}(d|\theta,\mathcal{M})\; p(\theta|\mathcal{M})}{\mathcal{E}(d|\mathcal{M})}, \tag{B.1}$$

where $\mathcal{L}(d|\theta,\mathcal{M})$ is the likelihood function, which is the probability of the data given a certain value of the parameters. $p(\theta|\mathcal{M})$ is the prior probability distribution that represents our state of knowledge before seeing the data. The term in the denominator is the evidence (or "marginal likelihood") which is a normalization constant in the Bayesian parameter estimation. On the other hand, in the case of model comparison, the evidence is the central quantity given by the relation

$$\mathcal{E}(d|\mathcal{M}) = \int \mathcal{L}(d|\theta,\mathcal{M})\; p(\theta|\mathcal{M})\; d\theta, \tag{B.2}$$

note that the Bayesian evidence is the average of the likelihood under the prior for a specific model choice [269].

Let us consider two different models, $\mathcal{M}_i$ vs $\mathcal{M}_j$, given the data, one interesting way to compare the performance of these models is from the Bayes's factor, defined as the ratio of the model's evidences

$$B_{ij} \equiv \frac{\mathcal{E}(d|\mathcal{M}_i)}{\mathcal{E}(d|\mathcal{M}_j)} = \frac{\mathcal{E}_i}{\mathcal{E}_j}, \tag{B.3}$$

where a value $B_{ij} > (<)1$ represents an increase (decrease) of the support in favor of model $\mathcal{M}_i$ versus model $\mathcal{M}_j$ given the data.

From the Bayes factors, the strength of the evidence in comparing two competing

models is usually interpreted using Jeffrey's scale, which is given in Table B.1.

$\lvert\ln B_{ij}\rvert$	Strength of evidence
< 1.0	Inconclusive
1.0	Weak
2.5	Moderate
5.0	Strong

Table B.1: The Jeffreys' scale, an empirical measure for interpreting the evidence in comparing two models $\mathcal{M}_i$ and $\mathcal{M}_j$. The left column indicates the threshold for the logarithm of the Bayes factor and the right column is the interpretation for the strength of the evidence above the corresponding threshold [269, 270].

Appendix C

Supplementary Material

In order to show that our simulations of Sections 5.3 and 6.7 have converged, we present below the best-fit results of our free parameters using simulated data. In Sec. 5.3, we consider four distribution models (SFR, GRB, Uniform and ED) with $N = 15, 30, 100$ and 500 points and different values for DM fluctuations ($\delta = 0, 100, 200, 400, 230\sqrt{z}$ pc/cm^3) and estimate $f_{\rm IGM}$ and $\rm DM_{host,0}$. Here we present the convergence for two cases: $N = 15$ and $\delta = 0$ pc/cm^3 (Fig. C.1) and $N = 500$ and $\delta = 400$ pc/cm^3 (Fig. C.2). Note that the simulations have converged after 50 runs.

Now in Sec. 6.7, we adopted two distribution models (SFR and GRB) with $N = 500$ and 1000 points and $\delta = 230\sqrt{z}$ pc/cm^3. In Figures C.3 and C.4 we present the best-fit results of our simulations for γ assuming $N = 500$ (Fig. C.3) and $N = 1000$ (Fig. C.4) and from these figures we can note that the simulations have converged after 100 runs.

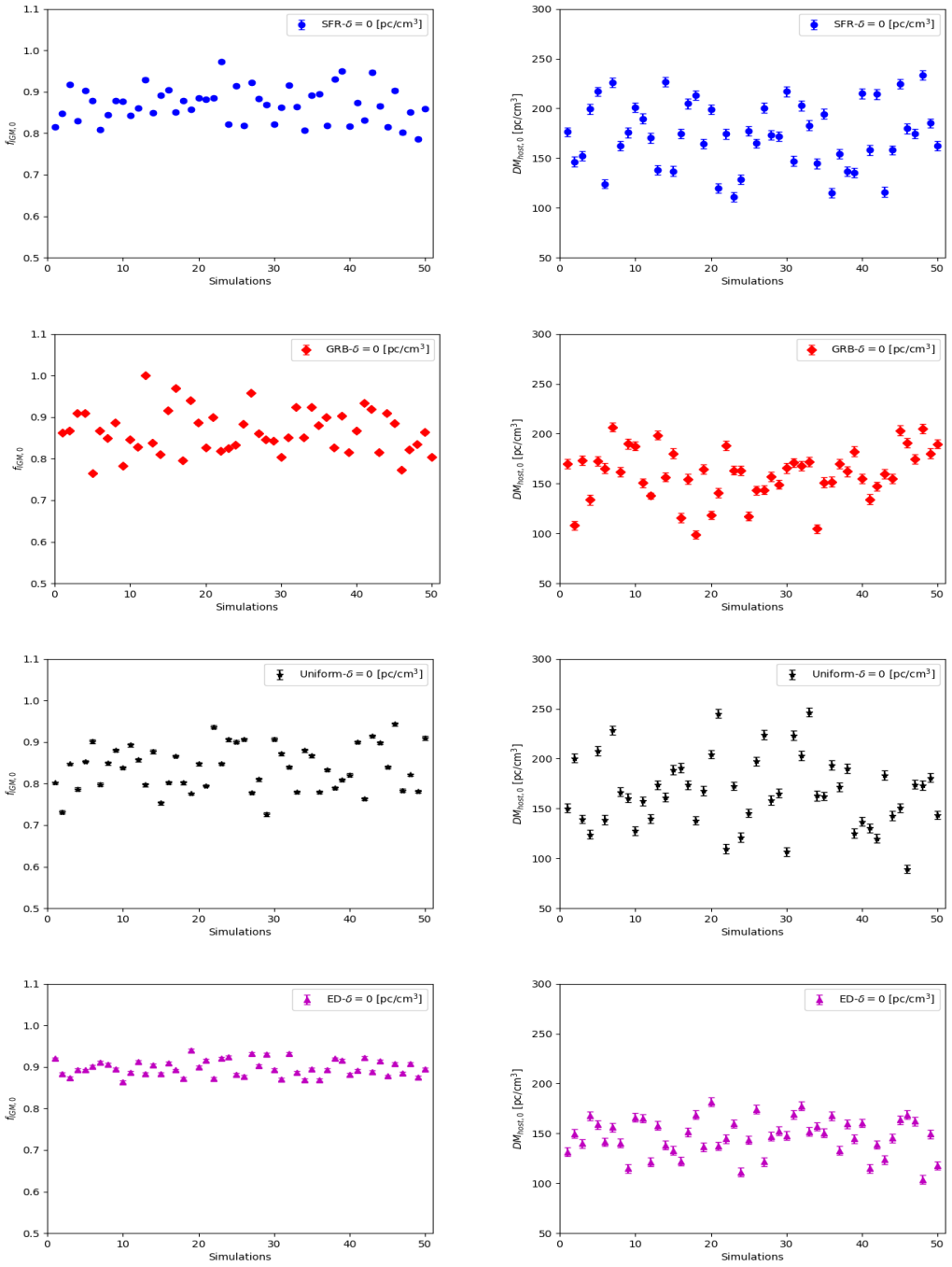

Figure C.1: The best-fit of the 50 simulations of SFR, GRB, Uniform and ED considering $N = 15$ and $\delta = 0$ pc/cm^3 for both parameters $f_{\rm IGM,0}$ and $\rm DM_{host,0}$.

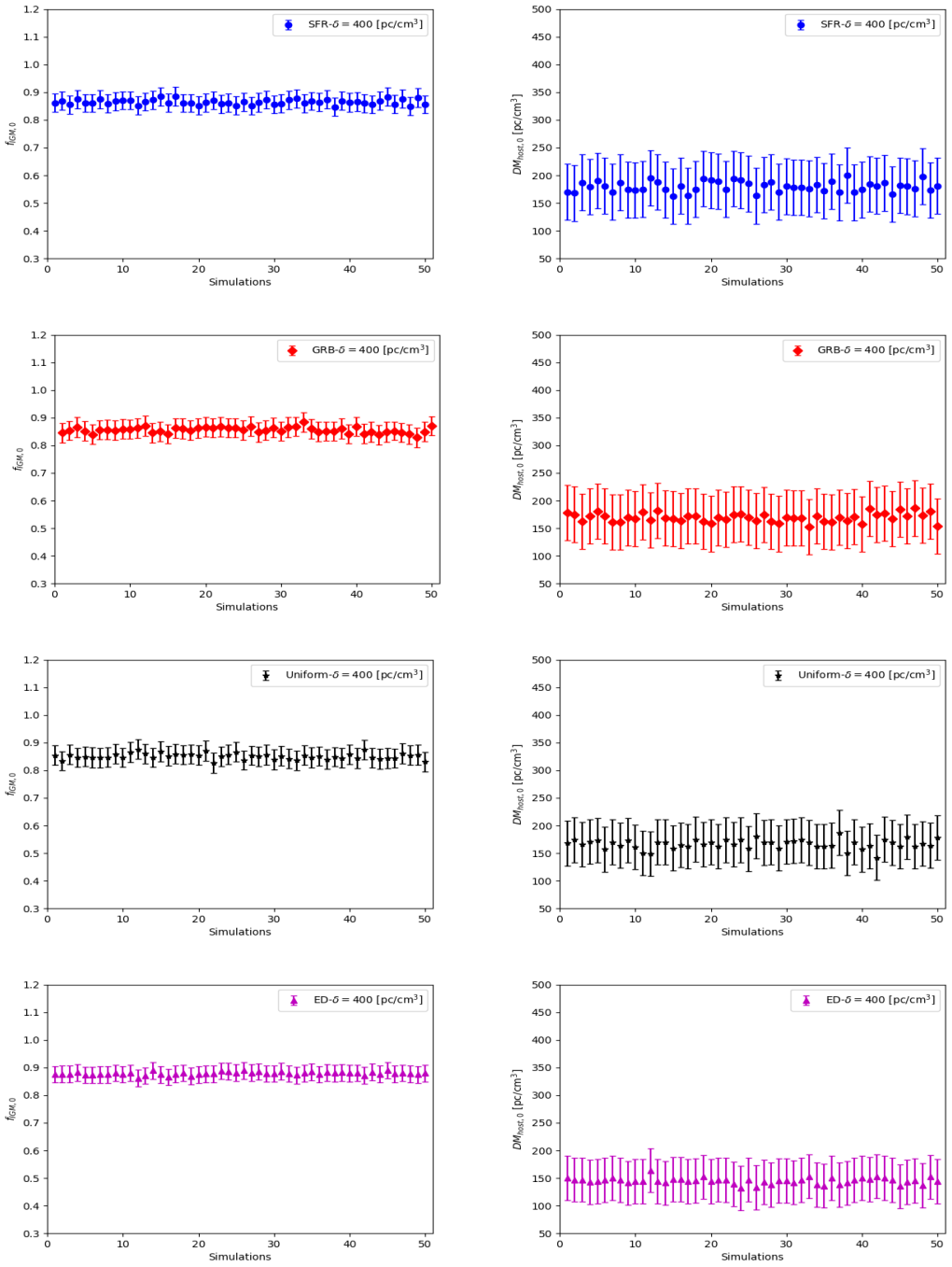

Figure C.2: The same as in the previous figure, considering $N = 500$ and $\delta = 400$ pc/cm^3.

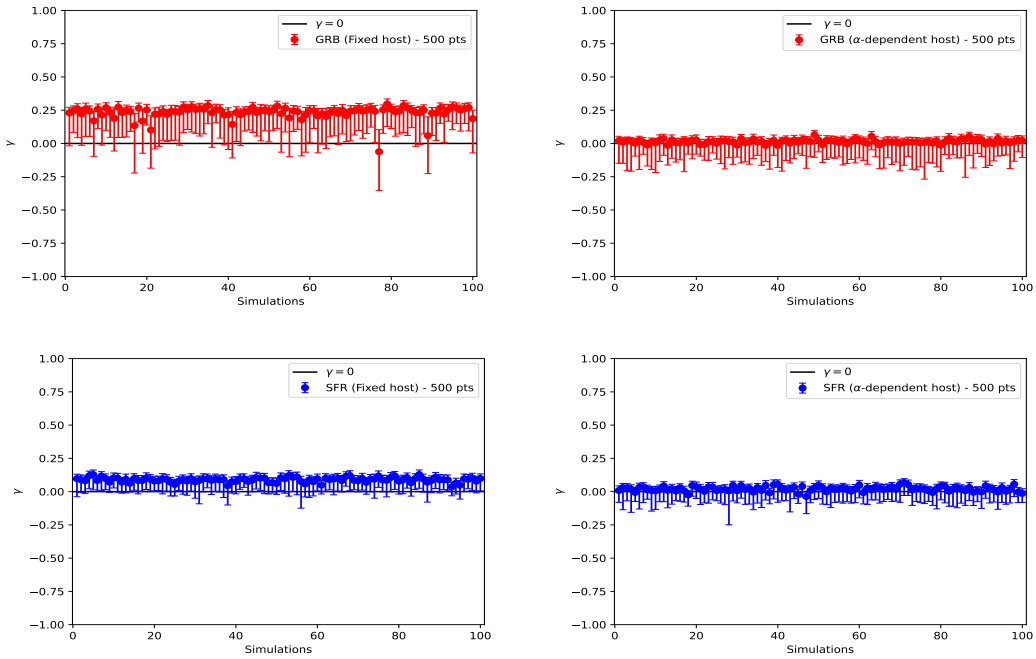

Figure C.3: The best-fit of the 500 simulations of γ for GRB and SFR distributions considering $N = 500$ for Fixed host and α-dependent host.

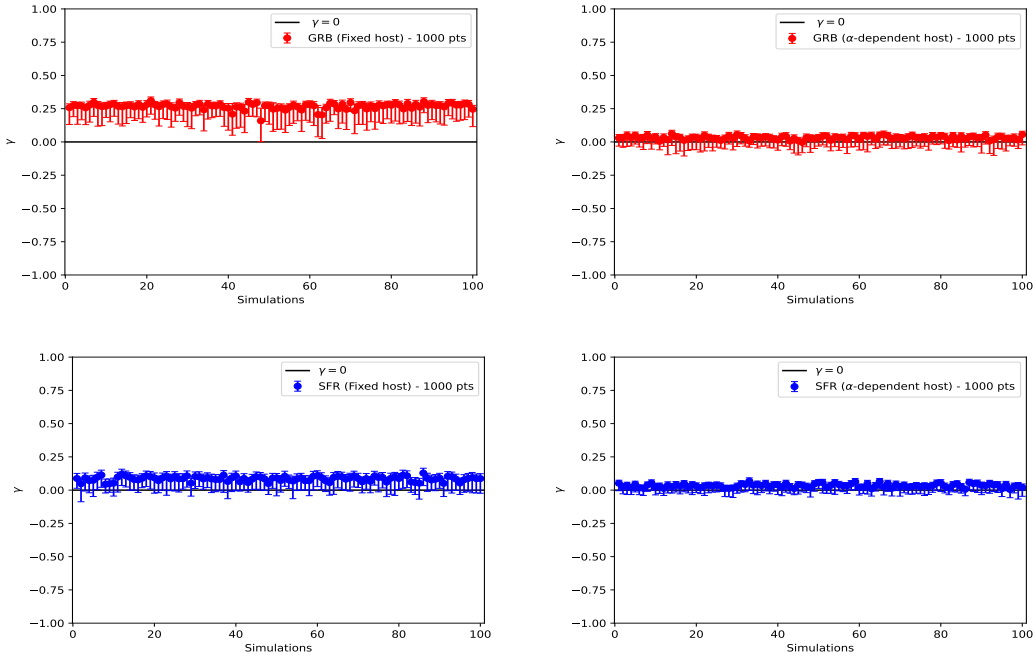

Figure C.4: The same as in the previous figure, considering N = 1000.